Inertial Confinement Fusion Reactor Cavity Analysis: Progress Report for the Period 1 July 1986 to 30 June 1987

R.R. Peterson, J.J. MacFarlane, G.A. Moses, M. El-Afify,
M.L. Corradini

July 1987

UWFDM-725

FUSION TECHNOLOGY INSTITUTE

UNIVERSITY OF WISCONSIN

MADISON WISCONSIN

DISCLAIMER

Inertial Confinement Fusion Reactor Cavity Analysis: Progress Report for the Period 1 July 1986 to 30 June 1987

R.R. Peterson, J.J. MacFarlane, G.A. Moses, M. El-Afify, M.L. Corradini

Fusion Technology Institute
University of Wisconsin
1500 Engineering Drive
Madison, WI 53706

http://fti.neep.wisc.edu

July 1987

UWFDM-725

INERTIAL CONFINEMENT FUSION REACTOR CAVITY ANALYSIS

Progress Report for the Period 1 July 1986 to 30 June 1987

R.R. Peterson

J.J. MacFarlane

G.A. Moses

M. El-Afify

M.L. Corradini

Fusion Technology Institute
1500 Johnson Drive
University of Wisconsin-Madison
Madison, Wisconson 53706

July 1987

UWFDM-725

1. INTRODUCTION

This is a progress report for research performed from July 1, 1986 to June 30, 1987 for Lawrence Livermore National Laboratory under subcontract number 9265205 with the project title: Inertial Confinement Fusion Reactor Cavity Analysis. This research generally considers the problems of vaporization and condensation of liquid metal or solid first surface materials in high yield ICF facilities such as reactors or high yield target test experiments.

For many years, ICF technology researchers have simulated the behavior of reactor target chambers following the explosion of a high yield target. This work has been theoretically based with little effort directed toward experimental verification of the models or the specific results. This was due in part to: (1) the long range nature of commercial reactors, (2) funding limitations, and, (3) the limited availability of suitable facilities to perform relevant experiments. In the past few years two of these issues have changed. It is currently believed that the next generation of driver facility will achieve target yields near reactor relevant levels. Therefore the reactor issues related to shot by shot phenomena (e.g., surface ablation and condensation and first wall loading) have become near term as well as long term problems. It is therefore appropriate to begin the study of these phenomena with the goal of experimental verification of the modeling before the final decisions need to be made about the next generation of driver facilities.

The past year's research consisted of 1.2 man years of effort on three tasks. These tasks were:

(1) Verify the current vaporization-condensation models in CONRAD through literature surveys of relevant published data, and evaluation and comparison of these data with predictions by CONRAD on condensation phenomena, and with predictions by CONRAD, ZPINCH, and/or MIXERG on radiation phenomena.

(2) Design a small-scale vaporization experiment by evaluating existing experimental facilities, selecting a primary facility, and conceptually designing an experiment complete with facility parameters and measurables.

(3) Design a small-scale condensation experiment including experimental parameters, measurables, and diagnostics.

The following three chapters report the results of the research on these three tasks. The CONRAD program for modeling ICF chamber phenomena has been compared to experimental or other theoretical results in seven different areas. In all cases we have either shown good agreement or have identified the inadequacies of CONRAD and have proposed further research to correct them. A small university-scale experiment to study condensation of liquid metal vapor at ICF reactor relevant temperatures and pressures has been conceptually designed. We are now prepared to begin fabrication and initial testing of the apparatus. The conceptual design of an x-ray vaporization experiment has been completed. Tradeoffs between the cost of three available x-ray sources and the experimental flexibility of each are discussed.

2. COMPUTER CODE VALIDATION

2.1 Introduction

In this section, we describe our efforts to validate some of the physical models used in CONRAD. CONRAD is a one-dimensional, Lagrangian hydrodynamics code which includes multifrequency radiation transport using the flux-limited diffusion approximation.[1] We have compared the results from various computer models with experimental data whenever possible, and with other theoretical computations when experimental data do not exist. In addition to examining CONRAD models, it has also been necessary to assess the reliability of our equation of state and opacity code - MIXERG.[2] This is because the radiation model in CONRAD relies heavily on the opacity tables computed by MIXERG.

Table 2-1 lists the different models we have examined, and indicates whether each resides in CONRAD or MIXERG. Also shown are the data we have used to check each model, and whether the data are based on experiments or theoretical calculations. Our equation of state, opacity, and radiation emission rate models have been compared with a number of other theoretical calculations. These will be discussed in Section 2.2. In Section 2.3, we describe our ion energy deposition model, and compare some of its results with experimentally determined stopping cross sections. The Naval Research Laboratory (NRL) laser-generated plasma experiments have provided some very good data on the formation and evolution of blast waves. In Section 2.4, we describe how this data has been used to test the radiation, hydrodynamic, and ion deposition models in CONRAD. In Section 2.5, we check the vaporization model in CONRAD with electron beam vaporization experiments carried out at Sandia National Laboratories (SNL). And finally, in Section 2.6, the x-ray deposition model is compared with calculations performed at LLNL.

2.2 Equation of State and Opacity Data

The equation of state and opacity tables used by CONRAD are calculated with MIXERG. It is important to have reliable estimates of the plasma opacities because the radiation model in CONRAD is of course strongly dependent on these data. Unfortunately, there are no experimental data available in the temperature range relevant to ICF reactor cavity studies (~ 1 eV to 1 keV) which can be used to validate theoretical results. Hence, we must try to assess the accuracy of the MIXERG results by comparing them with other theoretical calculations.

We have found three sources of computed data which we have used to test the MIXERG opacities and equations of state. These are the Astrophysical Opacity Library[3]

Table 2-1. CONRAD and MIXERG Models Examined

Model	Code	Data Type	Data
Equation of State	MIXERG	Theoretical	SESAME and Post et al.
Opacities	MIXERG	Theoretical	SESAME and Astrophysical Opacity Library
Radiation Emission Rate	CONRAD	Theoretical	Post et al.
Ion Stopping Cross Sections	CONRAD	Experimental	Anderson and Ziegler, Northcliffe and Schilling
Radiation, Ion Energy Deposition, and Hydrodynamic	CONRAD	Experimental	NRL laser plasma expts.
Vaporization	CONRAD	Experimental	SNL electron beam expts.
X-ray Deposition	CONRAD	Theoretical	LLNL calculations

(AOL) at Los Alamos, the SESAME[4] tables at Los Alamos, and results reported by Post, et al.[5] The SESAME tables include data for single-temperature opacities, ionization states, and specific energies. The AOL data provide frequency dependent opacity information, and are evidently the data base used to calculate the SESAME (frequency independent) opacities. Finally, Post et al. list results for the ionization states and radiation emission rates for low density plasmas.

In proposed ICF reactor cavities, the ambient pressure of the background gas is expected to be $\lesssim$ 10 torr. For nitrogen, this corresponds to a mass density of ~ 10^{-5} g/cm^3. This density, however, is lower than those for which the SESAME tables are generally established. That is, the physical models used to calculate the SESAME data are often not applicable to a high temperature, low density plasma. For instance, the SESAME specific energy tables for nitrogen[6] do not include the effects of electronic excitation and ionization. At the same time, however, the charge state tables for nitrogen include these effects. Thus, the SESAME tables are not always internally consistent.

Figure 2-1 shows the equilibrium charge state as a function of temperature of a nitrogen gas with a density of 6.3 x 10^{-4} g/cm^3. The solid curve was computed by MIXERG using the usual combination of Saha and coronal models. The coronal model is used in the high temperature, low density regime. The dotted curve shows the MIXERG results when the Saha model was used at all temperatures. This curve incorrectly reaches a maximum charge state lower than 7. This is unimportant because the coronal values will normally be used at these temperatures. The dashed line represents the SESAME results. Because of the good agreement between the MIXERG-Saha and SESAME curves, one would suspect that the SESAME values are computed using the Saha model. This model, however, is not appropriate to use for low density, high temperature plasmas because three-body recombination is unimportant under these conditions. Hence, we feel the MIXERG equation of state data are more reliable than the SESAME tables for the types of problems CONRAD is expected to simulate.

Figure 2-2 shows a similar comparison for a low density (coronal equilibrium) nitrogen gas. Here, the dashed curve represents the results of Post et al., and the open squares represent the MIXERG results. The agreement between the two calculations is good, with MIXERG predicting slightly higher charge states. These comparisons lead us to believe the MIXERG equations of state are reasonably accurate over the large range of densities and temperatures needed for ICF reactor cavity problems.

We have also compared the MIXERG opacities with those from the SESAME tables and the Astrophysical Opacity Library (AOL). Figure 2-3 shows the Rosseland and Planck opacities for neon as a function of the photon energy for a plasma temperature at 10 eV (top) and 1 keV (bottom). The density of the neon gas in each case is 10^{-3} g/cm^3. The solid curves represent the MIXERG values and the dotted curves the AOL values. The Rosseland opacities in each figure are represented by the curves that have a constant opacity in the high photon energy limit. At 10 eV, the MIXERG opacities are generally lower the the AOL values by 1 to 2 orders of magnitude. Also, it is seen that the MIXERG curve is missing the K-edge contribution from the photo-ionization of the final electron from neon (whose ionization potential is 1.36 keV). We are not certain at this time why MIXERG neglects this contribution. At a temperature of 1000 eV, the MIXERG opacities are 1 to 2 orders of magnitude larger than the AOL opacities. We cannot be certain which values are more reliable at this temperature because of the lack of experimental data. We do note, however, that the SESAME (and perhaps the AOL) ionization populations seem to be calculated using the Saha model even at these high temperatures.

Figure 2-4 shows the single temperature (integrated over photon energy) Rosseland and Planck opacities, respectively, for nitrogen as a function of temperature. The density in each case is 10^{-3} g/cm^3. The MIXERG opacities are again significantly lower than the SESAME values at temperatures $\lesssim$ 20 eV. We believe this may be due to MIXERG underestimating the contributions from electronic bound-bound transitions. At temperatures $\gtrsim 10^2$ eV, the agreement between the two calculations is much better.

At these relatively high densities, we expect the SESAME opacities should be more reliable than the MIXERG results. This should also be the case for low temperatures ($\lesssim$ 1 eV) because MIXERG does not include any molecular recombination effects. However, it is unclear whether the SESAME and AOL opacities should be any more reliable than the MIXERG values at the densities and temperatures relevant to ICF target chambers ($\rho \sim 10^{-10}$-10^{-5} g/cm^3, T ~ 1-1000 eV).

Finally, we have compared our radiation emission rates with the results of Post et al. at gas densities low enough for coronal equilibrium to exist. Under these conditions, the radiant cooling rate (per ion per free electron) and ionization states are independent of density. In CONRAD, the radiant energy emitted is $\propto \sigma_P T^4$, where σ_P is the Planck opacity and T is the plasma temperature. Figure 2-5 shows the emission rate for a low density nitrogen plasma as a function of the temperature. The solid curve represents the results of Post et al., and the open boxes are the MIXERG values, and correspond to a density of ~ 10^{15} atoms/cm^3 ~ 2 x 10^{-8} g/cm^3. The MIXERG emission rates are seen to be roughly 10 to 1000 times higher than the Post values. We have also observed that the MIXERG rates are inappropriately dependent on the density, with the emission rates increasing as the density decreases. We have located the source of this problem, and will correct it in the near future. As we will discuss in Section 2.4, this results in anomalously large radiant energy losses from the fireball regions in the NRL simulations.

To summarize, our comparisons of MIXERG equation of state and opacity data with the SESAME, AOL, and Post et al. calculations lead to the following conclusions: 1) the MIXERG charge states, and thus equations of state, appear to be fairly reliable, 2) MIXERG seems to be underestimating the contribution of bound-bound transitions to the opacity, and 3) the photo-ionization contribution to the opacity of low density plasmas is not being modeled correctly. Thus, we have located several areas where MIXERG can be improved. We do note, however, that the other calculations mentioned here do not provide a reliable and complete set of data necessary for ICF reactor cavity studies. The calculations of Post et al. are applicable only at densities where the coronal equilibrium model becomes valid (i.e., for electron densities $\lesssim 10^{16}$ cm^{-3}). Most of the SESAME data appear to be appropriate for calculations involving higher density gases and solids. We also stress that because of the lack of high temperature experimental data, it is difficult to determine the reliability of any of these theoretical calculations. Thus, although MIXERG has some shortcomings, we feel it is the best tool available to provide data for the wide range of materials and conditions required by CONRAD for ICF applications.

2.3 Ion Energy Deposition Model

A time- and energy-dependent model is used to compute the debris ion energy deposition. The ion velocity spectrum can be divided into as many as 10 different energy groups, and the ions are emitted from the target area over a time interval specified by the user. The total ion energy is specified by adjusting the debris ion flux. The debris ions transfer energy to the background gas through collisions at a rate determined by the ion stopping cross sections. The energy and location of each ion group is tracked until the ion velocities eventually fall below the thermal velocity of the gas, or until they escape the computational grid.

The ion stopping cross sections are calculated using a model similar to that described by Melhorn[7]. The debris ions interact with the background gas via ion-neutral, ion-ion, and ion-electron collisions. Other processes, such as plasma instabilities, are not included. The stopping cross section is defined to be the increment of energy dE lost by a "projectile" ion as it travels a distance dx through a material of atomic number density N. Mathematically, the stopping cross section can be written as:

$$S = \frac{1}{N}\frac{dE}{dx} = S_n + S_{be} + S_{fe} + S_{ii} \ . \qquad (1)$$

S_n and S_{be} are the contributions from elastic nuclear scattering and inelastic scattering from bound electrons, respectively. These arise from ion-neutral collisions and are therefore important only at lower temperatures. S_{fe} represents the contribution from collisions between the debris ions and free electrons, and becomes important at temperatures $\gtrsim$ 1 eV. The ion-ion term, S_{ii}, contributes only at very high temperatures ($\gtrsim 10^3$ eV), and can usually be ignored.

When the debris ion velocities are small compared to the orbital "velocities" of the bound electrons ($\sim v_0$ = velocity of an electron in the first Bohr orbit of hydrogen $\sim 2.2 \times 10^8$ cm/s), the stopping cross sections for ion-neutral collision are calculated using the Lindhard-Scharff model,[8] which is based on Thomas-Fermi theory.[9] At higher ion velocities, these cross sections are calculated using the Bethe model.[10] Comparisons between the theoretical stopping cross sections and experimental data are shown in Figs. 2-6 and 2-7. The cross sections for protons (Fig. 2-6) and aluminum ions (Fig. 2-7) traveling through nitrogen at room temperature are plotted as a function of the ion kinetic energy. The theoretical values are indicated by the solid line in each figure. Data taken from the tables of Northcliffe and Schilling[11] are indicated by the dashed lines. These data are based on a combination of experimental data and theoretical models. Also shown in Fig. 2-6 is a dotted curve which is a fit to experimental data.[12]

Figure 2-6 shows the theoretical stopping cross sections for protons are in excellent agreement with the experimental data over the entire energy range. The Northcliffe and Schilling data also agree with the experimental data for ions with kinetic energies $\gtrsim$ 200 keV, but are up to a factor of 2 too low at lower energies. In this plot, the total cross sections are dominated by the inelastic scattering term S_{be}. In Fig. 2-7, elastic collisions (S_n) make the largest contribution for kinetic energies below 100 keV. Here, the theoretical values for Al agree well with the Northcliffe and Schilling data. Unfortunately, experimental data for relatively heavy projectiles are sparse at energies relevant to the NRL experiments ($< 10^2$ keV). Even so, Ormrod et al.[13] have shown that the Lindhard-Scharff model is in general agreement with experimental data (within a factor of 2) for a wide variety of projectiles and stopping media. Consequently, we feel the low temperature contributions to the theoretical stopping cross sections should be fairly reliable.

At higher temperatures, the background gas becomes ionized and the stopping powers become dominated by electron-ion collisions. The free electron stopping cross section is proportional to the square of the charge state of the projectile ion $Z_1^\star$($S_{fe} \propto (Z_1^\star)^2$).[14] Figure 2-8 shows the theoretical total stopping cross sections for Al ions traveling through a partially ionized nitrogen plasma. The temperature is 10 eV and the average charge state of the nitrogen is assumed to be 2. The three curves were calculated for three different values of the projectile charge states: Al^{7+} (top curve), Al^{4+}, and Al^{1+} (bottom curve). To our knowledge, there are no experimental data available than can be used test the accuracy of the stopping power model for high temperature plasmas. At an energy that typically occurs in ICF problems, say ~ 10^2 keV, the ion stopping power for Al^{7+} is predicted to be roughly 20 times higher than that for singly ionized aluminum. The reason for this is the larger Coulomb field originating from the more highly charged ion results in greater momentum transfer to the electron.

The strong dependence of the total stopping cross section on the projectile charge indicates the importance of knowing the charge state of the debris ions as they evolve in time. This of course requires calculating the cross sections for charge-exchange and electron-capture reactions for the various ionization states of the projectile ions as a function of velocity. Because of the complexity involved in calculating these cross sections, we currently use an "average" charge for the debris ions, which in effect becomes an adjustable parameter. The sensitivity of CONRAD results to this average charge is addressed in Section 2.4.2.

2.4. Simulations of NRL Plasma Coupling Experiments

2.4.1 Overview of the NRL Experiments

The formation and evolution of shock waves resulting from laser-generated plasma expansions have been studied extensively in a series of recent experiments carried out at the Naval Research Laboratory (NRL).[15-21] In the NRL experiments we have simulated, a solid planar aluminum target was illuminated by an intense laser pulse (~ 10^{12} W/cm^2 with pulse width ~ 5 ns), producing an explosion of highly charged Al ions with velocities ~ 5 x 10^7 cm/s. The Al ions transfer energy and momentum (via collisions) to a surrounding nitrogen gas, producing significant ionization, and heating the gas to ~ 10^2 eV. Also, the Al ions, which are fully ionized as they leave the target,[22] undergo charge-exchange and electron-capture reactions as they speed through the background gas. Thus, the ionization state of the Al ions decreases as they travel through the gas. The ambient pressure of the background N_2 gas was varied from ~ 10^{-2} to 10^1 torr (room temperature values). The location of the shock front as it evolved was monitored using both dark-field shadowgraphy and framing photography.[16,20] In addition, spectroscopic observations were made to estimate the temperature, density, and charge state of the plasma.[17]

The background pressures in our calculations cover a range that varies from the high density, "collisional" regime to the low density, "collisionless" regime. That is, for background gas pressures $\gtrsim$ 1 torr, essentially all of the kinetic energy of the debris ions is lost in collisions with background gas particles that occur within a very small volume near the target. At gas pressures $\lesssim$ 0.1 torr, a large fraction of the debris ions will stream through the background gas while depositing very little of their energy. One of the purposes of this study is to gain a better understanding of the interaction, or "coupling", between the exploding plasma and the background medium in this transition region. In particular, we wish to determine whether classical collision theory can adequately explain the experimental data, or whether other effects, such as plasma instabilities, must be invoked. In addition, we want to assess the importance of radiation transport in the NRL experiments.

In Section 2.4.2, we will describe the results from simulations in which radiative transfer is neglected. In these problems, energy is transported away from the target by electron conduction and hydrodynamic motion. Results from calculations in which the diffusion approximation is used to model radiation transport will be discussed in Section 2.4.3. We have performed calculations with and without radiation in order to assess the importance of radiation energy losses, and also to test the validity of the radiation model in CONRAD for the conditions that existed in the NRL experiments. In Section 2.4.4, we will show how uncertainties in the equation of state can affect our results. And finally, in Section 2.4.5, we will summarize the conclusions of our NRL simulations.

2.4.2 Hydrodynamic Simulations

We assume in our calculations that the only energy source (other than the ambient thermal energy of the background gas) is the kinetic energy of the debris ions. The velocity distribution of the ions emitted from the target is well known from experiments performed with essentially no background gas surrounding the target. It is more difficult, however, to determine the appropriate debris mass to use in our 1-D spherical calculations because of the non-isotropic nature of the plasma expansion in the experiments. For instance, measurements obtained from experiments in which approximately 100 J of laser energy was focused onto a planar target[18] indicate that roughly 50 J of debris kinetic energy (0.4 μg of ions with $\langle v_{ion} \rangle \sim$ 450-500 km/s) expands into the hemisphere facing the incoming laser beam. Roughly half of that was contained in a cone of solid angle ~ $\pi/2$, and whose axis of symmetry lies perpendicular to the target (along the laser axis). Since most measurements of the shock properties were made in the solid angle where the debris concentration was highest, an equivalent value to use for the Al kinetic energy expanding into 4π steradians in our simulations is ~ 150-200 J. That is, we can simulate the NRL experiments that put 100 J of laser energy on target by assuming an isotropic spherical expansion of Al ions having a kinetic energy of ~ 12-16 J/steradian.

In assuming the debris ion kinetic energy is the sole energy source, we have neglected the energy emitted from the target in the form of x-rays. These x-rays partially ionize (0.2%) and heat the background gas to ~ 1-2 eV[19] before the target ions arrive. Ripin et al.[16] estimate that ~ 90% of the energy absorbed by the target is converted to debris energy. Thus, we can expect the target x-ray energy emitted to be $\lesssim$ 10% of the absorbed energy. Because the uncertainties in estimating the debris ion kinetic energy are much larger, we have chosen to neglect the effect of the target x-rays.

Results from a typical calculation are shown in Figs. 2-9(a) through 2-9(e). Plotted as a function of distance from the target are the plasma temperature, pressure, mass density, electron density, and fluid velocity. The different curves in each figure represent simulation times ranging from ~ 40 ns to ~ 250 ns (the shock moves from left to right in these figures). The total debris ion kinetic energy used in this calculation was 70 J, and the initial gas pressure was 5 torr. Radiation transport was not included in this calculation.

The most noticeable feature in Figs. 2-9(b) through 2-9(e) is the presence of a strong shock front. The front travels radially outward with a velocity ~ a few x 10^7 cm/s at early times, and slows as it sweeps up mass from the background gas. The shock front is quite clearly defined in simulations with this initial gas pressure, with the peak values for the pressure, fluid velocity, mass density, and electron density all occurring at about the same radius. Behind the shock front is a hot, low density microfireball, where the temperature distribution is roughly isothermal near the center. At the times shown, the temperatures are high enough to substantially ionize the gas in the fireball region.

We can compare the results from this calculation with observations from experimental shots in which 25 J of laser energy was focused onto an Al foil target.[17] In this experiment, the initial gas pressure surrounding the target was 5 torr, and the gas was composed of 90% N_2 and 10% H_2. From spectroscopic data, McLean et al.[17] have determined that the shock front reaches a radius of 1 cm (perpendicular to the target) at ~ 100 ns. Also, they have estimated the peak electron density at that point to be roughly 5×10^{18} cm^{-3}, and placed an upper limit of ~ 14 eV for the electron temperature in the shock front. The uncertainty in the temperature, however, is rather large because of the assumption that N^{2+} would be the highest observable ionization state. These observations are consistent with the results plotted in Fig. 2-9. Our calculations predict a shock arrival time at 1 cm of 95 ns, a peak electron density at 1 cm of 4.7×10^{18} cm^{-3}, and a temperature at 1 cm of ~ 10 eV at 100 ns. The temperature rises to ~ 30 eV at later times due to the fireball expansion. However, the temperature in the shock front (defined by the high electron density region) is significantly lower. Clearly, the 25 J laser energy experiments are well-described by our 1-D hydrodynamic simulations using a total debris ion kinetic energy of 70 J (or ~ 5.6 J/steradian).

It is somewhat surprising that the debris ion kinetic energy required by our calculations to predict the experimentally observed shock arrival time at 1 cm is so large. Earlier in this section, we estimated that a debris ion energy (E_{ion}) of ~ 150-200 J expanding into 4π steradians in our calculations should produce the same ion concentration that was observed in the experiments using 100 J of laser energy (E_{laser}) on target. That is, the ratio of the debris ion energy used in our simulations to the experimental laser energy is E_{ion}/E_{laser} ~ 1.5-2.0. However, to predict the shock arrival time observed in the experiments using 25 J of laser energy, our calculations require E_{ion}/E_{laser} ~ 70 J/25 J ~ 2.8. This larger ratio is likely caused by differences in the debris expansion characteristics between the 25 J and 100 J laser energy experiments. For example, the anisotropy in the plasma expansion may have been more pronounced in the 25 J experiments, or perhaps the velocity spectra of the target ions were significantly different. These effects could result from differences in the laser spot size focused on the target, the pulse duration, or the laser beam intensity.[15,23]

It is also of interest to track the evolution of the shock front as it propagates away from the target area. This is because the shock velocity provides information about how much energy from the debris ions has been "coupled" into the background gas. For instance, overestimating the ion stopping cross sections will result in shorter mean free paths for the Al ions, and energy will be absorbed by the background gas closer to the target. If the ion stopping range is comparable to or larger than the shock radius, the resulting shock radius will be too large. Comparisons between our calculated shock radii and experimental observations are shown in Fig. 2-10 as a function of time. In these calculations, the total debris ion energy was 150 J (~ 12 J/steradian). The solid curves represent the calculated radii for 4 different initial gas pressures: 0.1 (at top), 0.3, 1.5, and 5 torr. The open symbols in each plot represent the shock positions observed in NRL experiments in which 100 J of laser energy was focused onto the Al target. The straight dashed line originating from the origin represents the initial velocity of the debris ions (~ 5×10^7 cm/s). The experimental data were obtained using framing photography of the visible emission fronts.[20] Because the emission is a strong function of the electron density,[20] we have defined the location of the shock front in our simulations to be the radius at which the electron density was a maximum.

Figure 2-10 shows that the calculated shock radii are in reasonable agreement with the experimental data at all pressures. The calculated shock radii for the 0.1 and 0.3 torr cases are slightly greater than the experimental values, while the radii for the 1.5 torr case agree quite well with the data. In the 5 torr problem, the computed radius agrees with the NRL data at early times ($\lesssim$ 100 ns), but predicts a somewhat larger radius at later times. It is worth noting that the calculated curve at 5 torr has a trajectory that is quite similar to that predicted by strong shock theory ($r \propto t^{2/5}$).[24] Although there is some "scatter" in the NRL data, the experimental shock velocities are noticeably smaller than the calculated velocities at times $\gtrsim$ 100 ns. Thus, it appears that the part of the shock front observed in the NRL experiment, which is perpendicular to the target and along the laser axis, is losing a significant amount of energy at these times. One explanation for this is a significant amount of radiant energy may be escaping from behind the shock front in the NRL experiments. Another possibility is that energy that was preferentially deposited along the laser axis (due to the anisotropic debris ion flux) may be diffusing away from this axis. In this case, the shock front would become more spherical as the energy is redistributed away from the laser axis.

The sensitivity of our results to the uncertainties in the charge states of the Al ions is illustrated in Fig. 2-11. As discussed in Section 2.3, we can adjust the energy deposition range of the Al ions by modifying the average charge state used in calculating the free electron stopping cross sections. Figure 2-11 compares the results of calculations using different values for the Al charge state for both the 0.1 and 5 torr problems. The solid curves represent the shock radii computed using an ionization state of Al^{4+}, and the dashed curves represent similar results for Al^{2+}. The open symbols represent the experimental values. In these calculations, the debris ion kinetic energy was again 150 J, and radiation transport was neglected. The shock radius is seen to be quite sensitive to the charge state of the debris ions at 0.1 torr. An ionization state of 3 would produce good agreement with the experimental data. At higher pressures, the blast wave properties show little dependence on the ionization state of the debris ions. This is because the Al ions lose essentially all of their energy in a very small volume of gas near the target regardless of the free electron stopping cross sections.

We have also performed calculations for a case with a 0.025 torr background gas and found good agreement with the NRL data when the ionization state of the Al ions was increased to 6. The "average" charge state of the debris ions should of course increase as the background gas pressure decreases because the distance an Al ion must travel before capturing each electron becomes larger. Although the blast wave properties at this ambient pressure are extremely sensitive to the assumed ionization states of the Al ions, we have demonstrated that a model based on classical collision theory can quite adequately describe the energy transfer from the debris ions to the background gas in the NRL experiments. Collective effects, which are not included in our stopping cross section model, are not required to increase the "effective" collisional interaction, and so are probably not a significant source of momentum transfer for ambient pressures down to 25 mtorr.

In another study, Kacenjar et al.[21] reported the results of computer simulations in which they calculated the hydrodynamic and magnetic properties resulting from spherical plasma expansions occurring in the presence of a magnetic field. In their simulations, rate equations for various collisional processes were used to calculate the evolution of the ionization states of the aluminum and nitrogen particles. In a problem similar to one reported in their paper, we calculated the response of a 0.2 torr background gas to an 82 J spherical expansion of Al ions. Whereas Kacenjar et al. found the shock front radius (defined by peak electron density) at 100 ns to be ~ 1.0 cm, our calculations predict a substantially larger shock radius of 1.6 cm. Interestingly, by reducing the charge state of the Al ions in our calculations from 4 to 0 (i.e., neutral Al), the shock radius at 100 ns decreases to 1.0 cm. That is, the two calculations produce similar results when we completely neglect the effects of collisions between the Al ions and free electrons in our calculations.

We can estimate what the observed shock radius at 100 ns was in the 0.2 torr NRL experiments from the "coupling efficiency" curves of Ripin et al.[18] From emission photography data, the shock radius is estimated to be 1.5 ± 0.1 cm. Although a smaller radius (1.1 ± 0.2 cm) is predicted from shadowgraphic measurements, the emission front results are expected to be more reliable when the background gas pressure is $\lesssim 0.3$ torr.[20] Our simulations best reproduce the emission photography data when the charge state of the Al ions is ~ 3. Note that this ionization state also produced the best agreement with experimental data at 0.1 and 0.3 torr (see above).

Strong shock theory has been used[15,18] to find the "effective" energy coupled into the blast waves in the NRL experiments. But this approach is only valid when: 1) energy losses (e.g., due to radiation) are unimportant, and 2) at times and distances that are large compared to those over which the energy is deposited. Our calculations indicate that the second condition does not hold for the lower pressure experiments ($\lesssim 1$ torr). Figure 2-12 shows the spatially integrated debris ion energy deposited as a function of distance from the target. The total ion kinetic energy used in these calculations was ~ 150 J, and results are shown for 4 different initial gas pressures. At 5 torr, it is seen that essentially all of the ion energy is deposited within ~ 0.5 cm from the target. At lower pressures, however, the volume over which the energy is deposited increases substantially. Only 50% of the energy from the Al ions has been transferred to the background within a radius of ~ 1.8 and 5.4 cm for the 0.3 and 0.1 torr cases, respectively. By comparison, the maximum shock radius measured in the NRL experiments is ~ 2.5 cm. Hence, strong shock theory will not be as reliable when estimating the properties of blast waves in the NRL experiments for the pressures much below 1 torr.

Another reason the shock trajectories in Fig. 2-10 should not follow those predicted by strong shock theory ($r \propto t^{2/5}$) is that hydrodynamic motion is not the dominant means of energy transport at early times. This is more readily seen at the lower nitrogen gas pressures. (Although this effect is not clearly seen in the NRL data shown here, it is much more noticeable for the 0.025 and 0.044 torr data.[18,20]) At early times, the radius increases at a rate roughly equal to the debris ion velocity. At low ambient pressures, the Al ions transfer enough energy to heat the background gas, but not enough to significantly slow the ions. During this time, electron conduction is redistributing within the microfireball energy that was deposited by the debris ions. Eventually, the debris ions are stopped; or in the case of low pressures, they are unable to heat the background gas sufficiently to cause significant ionization. The latter occurs because the flux of Al ions decreases as $1/r^2$ (r = distance from the target). When the debris ions are unable to sufficiently heat the gas to the point that electron thermal conduction is important, hydrodynamic flow becomes the primary means of energy transport. In our 0.1 torr calculation, the shock radius does not follow a $r \propto t^{2/5}$ trajectory until times $\gtrsim 200$ ns.

The above results show that the stopping power model in CONRAD, which is based on classical collision theory, can explain the blast wave properties observed in the NRL experiments for ambient gas pressures down to 25 mtorr. The calculations best reproduce the experimental blast wave data in the 0.1 to 0.3 torr range when a charge state of 3 is assumed for the Al ions, and at 0.025 torr when a charge state of 6 is used. For background gas pressures $\gtrsim$ 1 torr, the shock radius is relatively insensitive to the assumed ionization state of the Al ions. The increase in the ionization state of the Al projectiles should be expected because the Al ions must travel farther before capturing an electron in a lower density plasma.

2.4.3 Radiation Effects

We next examine how including radiative transport in the energy equations affects the results of our simulations. We have performed a series of calculations similar to those described in Section 2.4.2, but this time radiation transport is included using a flux-limited diffusion model.

Figures 2-13(a) through 2-13(d) show results from a radiation-hydrodynamic calculation assuming a total debris ion energy of 70 J and an ambient N_2 gas pressure of 5 torr. Plotted as a function of radius are the plasma temperature, radiation temperature, plasma pressure, and electron density. Comparing Fig. 2-13(a) with Fig. 2-9(a), it is seen that the plasma temperature is a factor of ~ 4 to 6 lower when radiation transport is included in the calculation. The plasma temperature distribution is roughly isothermal at times $\gtrsim$ 100 ns. At earlier times, temperature variations persist because the plasma is emitting radiation faster than electron thermal conduction can reduce the gradients. This effect, however, is not necessarily real because the computed emission rate is probably too large (see Section 2.2). Figure 2-13(b) shows that the radiation temperature (defined to be proportional to the fourth root of the radiant energy density) is significantly lower than the plasma temperature, which indicates that the radiation field has not had time to equilibrate with the plasma. Instead, the relatively short diffusion times allow a significant fraction of the radiant energy to diffuse outward, far ahead of the shock front. Consequently, the escaping energy reduces the temperature in the microfireball, and less energy is available to generate hydrodynamic motion. This can result in a substantially weaker blast wave.

Because of the large radiation losses, the shock velocity is substantially lower. The shock arrival time at a distance of 1 cm from the target is 145 ns (Fig. 2-13(d)). This is roughly 50% longer than the value found from calculations in which radiation losses were ignored (Fig. 2-13(d)). In order to match the shock arrival time in the 25 J laser energy experiments of McLean et al. (see Section 2.4.2), the total debris kinetic energy in our calculations must be raised to 140 J (i.e., a factor of 2 increase). Although the predicted electron density and temperature in the 140 J calculation are in agreement with the values derived from experimental data, it seems unlikely that such a large debris ion flux (E_{ion}/E_{laser} ~ 5.6) would be produced in the 25 J laser energy experiments.

Another interesting effect reported by McLean et al. was that a discrete jump in the continuum intensity was detected at a point 1 cm from the target roughly 50 ns before the shock front arrived.[17] The electron density in this "pre-step" region was estimated to be ~ 2×10^{18} cm^{-3}, or about 40% of the peak electron density observed when the shock front arrived. This effect is not observed in our calculations when the usual radiative transfer model was used (see Fig. 2-13(d)). But a "pre-step" was seen qualitatively in similar calculations in which the values in the opacity tables were increased by a factor of 100. Because of the shorter photon mean free paths, radiation emitted from behind the shock front can be reabsorbed in a region just ahead of the shock front instead of escaping to much farther distances. It seems quite possible that given the uncertainties in the opacities, the "pre-step" observed in this experiment was caused by the absorption of radiation emitted from behind the shock front. This conclusion would also be consistent with the possibility that our opacities are somewhat low (see Section 2.2).

The shock radii computed in a series of radiation-hydrodynamic calculations using a debris ion energy of 150 J are shown in Fig. 2-14. The initial background gas pressures range from 0.1 torr (top curve) to 5.0 torr. The open symbols again represent the NRL data. The calculated shock radii are somewhat larger that the experimental values for the 0.1 and 0.3 torr cases, but slightly small for the 1.5 and 5 torr cases. It is also seen that, except for the 5 torr case, the calculated shock velocities are somewhat lower than the experimental data predict. This indicates that too much energy is being radiated from behind the shock front in our calculations. When radiation losses are neglected, the calculated shock velocities are in much better agreement with the experimental data (see Fig. 2-10). Thus, as Ripin[22] has suggested, it appears that radiation plays a relatively minor role in the energy transport of the NRL experiments.

The large radiation losses in our low density calculations are likely caused by CONRAD overestimating the radiation emission rate. This is due to the MIXERG Planck opacity being too large for low density plasmas (see Section 2.2). The second possible problem is that the radiation diffusion approximation is inappropriate to use for the conditions in these problems. The validity of the diffusion approximation can be tested by estimating the value of the photon mean free path. For a nitrogen gas at a temperature of ~ 10 eV and a density corresponding to an initial pressure of 1 torr, the Rosseland opacity is ~ 10^2-10^3 cm^2/g.[25] This leads to a photon mean free path of ~ 10^2-10^3 cm.

Clearly, this violates the assumption that the photon mean free paths are small compared to the characteristic dimensions of the problem (which in the NRL experiments are ~ 1 cm). Hence, the diffusion approximation may lead to inaccurate results in simulations of the NRL experiments and in fact may be marginal for reactor applications.

2.4.4 *Equation of State Effects*

We have performed a set of calculations to determine how uncertainties in the equation of state affect the results of the CONRAD simulations. To do this, we ran simulations similar to those described earlier in this section, but this time substituting the SESAME equation of state data for the MIXERG values. In each of these calculations, radiation transport was neglected so that the opacities did not affect the results. Also, neon was used as the background gas because the SESAME equation of state for nitrogen neglected the effects of electronic excitation and ionization, and thus was not physically reasonable for these calculations.

Figure 2-15 shows the shock radius as a function of time for the MIXERG (solid curves) and SESAME (dashed curves) calculations at two different initial background gas pressures. The squares and circles represent results for a background gas pressure of 0.3 and 5.0 torr, respectively. It is seen that the shock radii computed using the SESAME equation of state are just slightly ($\lesssim$ 10%) larger that those computed using the MIXERG equation of state. This results from the fact that the SESAME heat capacities are slightly smaller than the MIXERG values. We can therefore conclude that reasonable inaccuracies in the equation of state will have a relatively minor effect on the blast wave properties computed by CONRAD.

2.4.5 *Summary of NRL Simulations*

The NRL experiments have provided valuable data that have been used to test a number of the computer models in CONRAD. At the same time, we feel the CONRAD simulations have lead to a better understanding of the physical processes that are important in the NRL experiments. The main conclusions from this study are as follows:

1. Our results indicate that the interactions between the expanding debris ions and the nitrogen background gas in the NRL experiments can be adequately modeled using classical collision theory. Collective effects are not required to explain the blast wave data down to pressures of at least 0.025 torr.
2. We have shown that the blast wave properties depend sensitively on the charge state of the debris ions for ambient gas pressures below 1 torr. This is because electron-ion collisions are the dominant mechanism of energy transfer from the debris ions in the experiments, and because the collisional mean free path becomes larger than the shock radius at the lower pressures.

3. The NRL blast wave data of McLean et al.[20] are best reproduced by calculations in which the initial debris ion kinetic energy is ~ 150 J, the energy loss due to radiation is neglected, and the "average" charge state of the Al ions is ~ 3 for ambient pressures of 0.1 to 0.3 torr and ~ 6 for ambient pressures near 0.025 torr. This dependence between the gas pressure and charge states is expected because the Al ions should remain more highly ionized in the lower density experiments because they must travel farther before capturing an electron. It is realized that computing the stopping cross sections using a constant value for the Al charge state is rather simplistic. Although the charge state has been shown to be unimportant when the background gas pressure is $\gtrsim$ 1 torr, calculations at lower pressures should include the effects of charge transfer between the debris ions and background plasma.
4. Radiation losses appear to be unimportant in the NRL experiments. We suspect the rather large radiation losses in our lower pressure calculations are caused by CONRAD overestimating the emission rates (as discussed in Section 2.2).
5. Reasonable inaccuracies in the equation of state have been shown to lead to only minor errors in the calculated blast wave properties.
6. We expect that equilibrium assumptions used in our calculations are not always valid for the conditions that occur in the NRL experiments. For example, the mean collision time between electrons and ions is given by:[24]

$$\tau_{ei} \sim \frac{5 \times 10^7 \, A T_{eV}^{3/2}}{N Z^2} ,$$

where T_{eV} is the plasma temperature in eV, A is the atomic weight, Z is the charge state, and N is the ion number density. Thus, for $A = 14$ (nitrogen), $T_{eV} = 10$, $Z = 2$, and $N = 7 \times 10^{16}$ (corresponding to a gas pressure of 1 torr), the collision time is ~ 80 ns. Clearly, the equilibration time between the electron and ions is not small compared to the times discussed in this report.

This may be particularly important because the primary mechanism for transferring energy from the debris ions to the background plasma is ion-electron collisional interaction. Hence, we feel it may be important for CONRAD to use a two-temperature model for the ions and electrons.

2.5 X-Ray Deposition Verification

We have tested CONRAD's ability to calculate the deposition of x-rays in materials. We have compared the deposition of target x-rays in CONRAD with calculations done by Charles Orth of LLNL.[26] Orth's calculations showed that the x-ray deposition in the July 1986 version of CONRAD did not agree with either the BUCKL computer code or with Orth's PROFILE code. We have made improvements to the x-ray deposition in CONRAD and have run the same calculation as Orth. The prescribed incident x-ray spectrum is shown in Fig. 2-16 and the deposition profile in a 5 meter radius aluminum shell is shown for CONRAD and PROFILE calculations in Fig. 2-17. There is obviously good agreement between the two calculations. The results differ the most at the greatest depth into the material, where the deposited energy is low.

We feel that the good agreement with Orth's results verifies the x-ray deposition in CONRAD. There is good agreement between PROFILE and the BUCKL code,[27] and both are generally believed to be correct. PROFILE uses cross section data from LLNL,[28] which are presumably not directly related to the calculation done in BUCKL. CONRAD also uses a different set of data and a different method for the calculation of energy deposition. Therefore three independent calculations now yield very similar x-ray deposition results. The cross section data used have partially been compared with experiment but as yet we know of no direct measurements of x-ray deposition profiles.

2.6 Vaporization Verification

We have recently discovered some pulsed vaporization data that we can compare with the vaporization in CONRAD. Croessmann[29] at SNL has used pulsed electron beams to vaporize graphite. The electrons will not penetrate the same depth into the material as target x-rays and the pulse widths are long compared to ICF applications. The experiments we have chosen to compare with CONRAD results use 30 keV electrons in a pulse that lasts for 0.1 s. The experimental results are depicted in Fig. 2-18, where the sublimation thickness is plotted against energy fluence. The CONRAD simulation results are also shown in this figure. Given the problems that we have had in finding good experimental results for x-ray vaporization, we feel that these well parameterized experiments are helpful. We still need to find a good x-ray vaporization experiment to fully test the vaporization models in CONRAD.

We have simulated the deposition of 30 keV electrons in graphite by using CONRAD to calculate the deposition of 1.65 keV x-rays in graphite. Both 30 keV electrons and 1.65 keV photons have ranges of about 2×10^{-3} g/cm^2 in graphite. X-rays deposit their energy exponentially while electron energy deposition is not exactly exponential, but we don't think that this inaccuracy in our calculations leads to large errors in the deposition profile.

The results of our vaporization calculations are shown in Fig. 2-18, where they are compared with experimental results and other computations. The shielded and unshielded calculations referred to in Fig. 2-18 either consider the stopping of electrons in the vapor or do not. The shielding model assumes a linear vapor density profile and a very simple reradiation approximation. One can see that our calculations agree well with Croessmann's shielded calculations and that the experimental data agree with the unshielded results. Croessmann's shielded calculation and CONRAD assume that the vapor moves off of the surface in a direction normal to the surface, which for the small (0.95 cm in radius) samples in Croessmann's experiment is very probably not a good approximation. If the vapor has a significant velocity component parallel to the surface on the sample, the vapor plume will spread out and let more electron energy through to the sample surface and will increase the vaporization. Therefore, one should expect the CONRAD simulations to underestimate the vaporization. One should also notice that the threshold energy fluence for the onset of vaporization as calculated by CONRAD agrees well with the experimental data.

The reasonable agreement between CONRAD and electron beam vaporization experimental data validates the calculation of heat transfer in the vaporizing material and of the slow evaporation of material. When energy is deposited slowly, as it is in this experiment, heat transfer into the solid material limits vaporization. In CONRAD, when energy is deposited volumetrically in a solid material over a finite period of time, the rate of vaporization of that material is calculated as a function of the surface temperature,

$$\dot{m} = \rho \sqrt{\frac{T_{surf}\ 4.13 \times 10^3}{A}}\ \exp\left(-\frac{121\ \Delta H_v A}{T_{surf}\rho}\right)\ . \tag{1}$$

Here, ρ is the mass density of the material, T_{surf} is the surface temperature in K, A is the atomic mass number of the material, and ΔH_v is the latent heat of vaporization.

This calculation should be distinguished from the models used in CONRAD when the deposition is instantaneous (i.e., occurring over a time much shorter than the thermal diffusion time). When the deposition is instantaneous, CONRAD calculates the vaporization as depicted in Fig. 2-19, where the vaporization is related to the local energy density profile in the material. Croessmann's experiment does not test instantaneous vaporization.

REFERENCES FOR SECTION 2

1. R.R. Peterson, UWFDM-670, Fusion Technology Institute, University of Wisconsin, Madison, WI (1986); G.A. Moses, R.R. Peterson, and T.J. McCarville, Comput. Phys. Commun. 36, 249 (1985).

2. R.R. Peterson and G.A. Moses, Comput. Phys. Commun. 28, 405 (1983).

3. W.F. Huebner, A.L. Merts, N.H. Magee, Jr., and M.F. Argo, LA-6760-M, Los Alamos Scientific Laboratory, Los Alamos, NM (1977).

4. G.I. Kerley, LASL-79-62, Los Alamos National Laboratory, Los Alamos, NM (1980).

5. D.E. Post, R.V. Jensen, C.B. Tarter, W.H. Grasberger, and W.A. Lokke, At. Data and Nucl. Data Tables 20, 397 (1977).

6. K.S. Holian, LA-10160-MS, Los Alamos National Laboratory, Los Alamos, NM (1984).

7. T.A. Melhorn, J. Appl. Phys. 52, 6522 (1981).

8. J. Lindhard and M. Scharff, Phys. Rev. 124, 128 (1961).

9. L.H. Thomas, Proc. Camb. Phil. Soc. 23, 542 (1927). E. Fermi, Z. Phys. 48, 73 (1930).

10. H.A. Bethe, Ann. d. Physik (Leipzig) 5, 325 (1930).

11. L.C. Northcliffe and R.F. Schilling, Nuc. Data Tables A7, 233 (1970).

12. J.J. Andersen and J.F. Ziegler, Hydrogen Stopping Powers and Ranges in All Elements (Pergamon, New York, 1977).

13. J.H. Ormrod, J.R. Macdonald and H.E. Duckworth, Can. J. Phys. 43, 275 (1965).

14. J.D. Jackson, Classical Electrodynamics, 2nd Edition (Wiley, New York, 1975).

15. B.H. Ripin, A.W. Ali, H.R. Griem, J. Grun, S.T. Kacenjar, C.K. Manka, E.A. McLean, A.N. Mostovych, S.P. Obenschain and J.A. Stamper, in Laser Interaction and Related Plasma Phenomena, Vol. 7, edited by G. Miley and H. Hora (Plenum, New York, 1986), pp. 857-877.

16. B.H. Ripin, J.A. Stamper and E.A. McLean, NRL Memorandum Report 5279, Naval Research Laboratory, Washington, D.C. (1984).

17. E.A. McLean, J.A. Stamper, H.R. Griem, A.W. Ali, B.H. Ripin and C.K. Manka, NRL Memorandum Report 5274, Naval Research Laboratory, Washington, D.C. (1984).

18. B.H. Ripin, E.A. McLean, J.A. Stamper, J. Grun, C.K. Manka and A.N. Mostovych, ETHANOL, Issue #7, p. 75, SRI International, Menlo Park, CA (1987).

19. A.W. Ali and E.A. McLean, J. Quant. Spectrosc. Radiat. Transfer 33, 381 (1985).

20. E.A. McLean, B.H. Ripin, A.W. Ali, H.R. Griem, J. Grun, C.K. Manka, A.N. Mostovych, S. P. Obenschain and J. A. Stamper, ETHANOL, Issue #7, p. 20, SRI International, Menlo Park, CA (1987).

21. S. Kacenjar, M. Hausman, M. Keskinen, A.W. Ali, J. Grun, C.K. Manka, E.A. McLean and B.H. Ripin, Phys. Fluids 29, 2077 (1986).

22. B.H. Ripin, private communication (1986).

23. J. Grun, R. Decoste, B.H. Ripin and J. Gardner, Appl. Phys. Lett. 39, 545 (1981). J. Grun, R. Stellingwerf, and B. H. Ripin, Phys. Fluids 29, 3390 (1986).

24. Y.B. Zel'dovich and Y.P. Raizer, Physics of Shock Waves and High-Temperature Hydrodynamic Phenomena (Academic Press, New York, 1966).

25. Opacity value calculated using MIXERG; see Ref. 2.

26. Charles Orth, LLNL, private communication, July 15, 1986.

27. R.K. Cole, Jr., "BUCKL: A Program for Rapid Calculations of X-Ray Deposition," Sandia National Laboratories, Albuquerque, NM, SC-RR-69-855 (1970).

28. E.F. Plechaty, D.E. Cullen and R.J. Howerton, "Tables and Graphs of Photon-Interaction Cross Sections From 0.1 keV to 100 MeV Derived From the LLL Evaluated-Nuclear-Data Library," Lawrence Livermore National Laboratory, Livermore, CA, UCRL-50400, Vol. 6, Rev. 3 (1981).

29. C.D. Croessmann, G.L. Kulcinski and J.B. Whitley, "Graphite Sublimation and Hydrocarbon Production Due to Intense Energy Deposition," Sandia Report SAND86-0764 (June 1986).

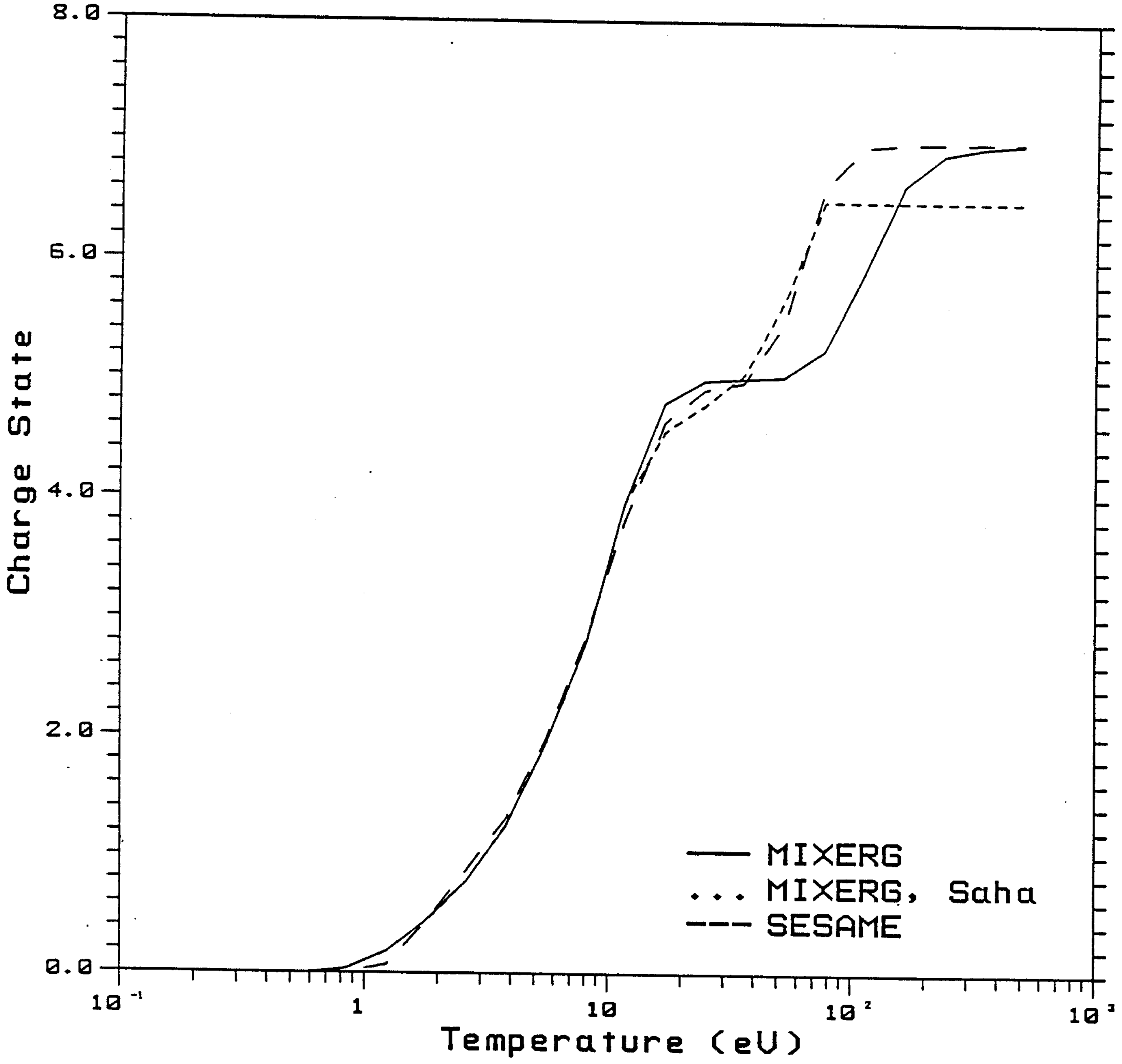

Fig. 2-1. Charge state vs. temperature computed for nitrogen using the MIXERG Saha/Coronal model, the MIXERG Saha model only, and SESAME. The density is 6.3 x 10^{-4} g/cm^3.

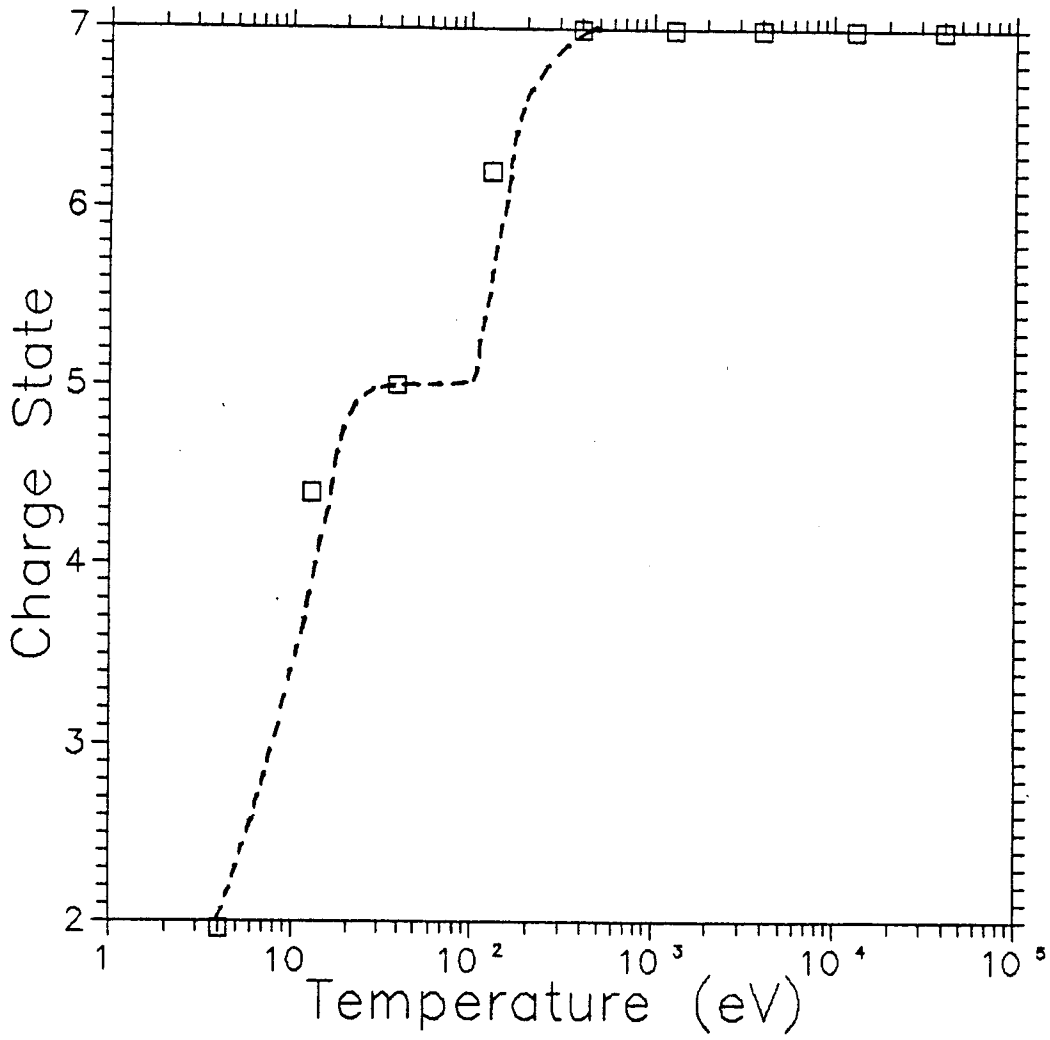

Fig. 2-2. Charge state vs. temperature computed by MIXERG (squares) and Post et al. (dashed curve) for a low density nitrogen plasma.

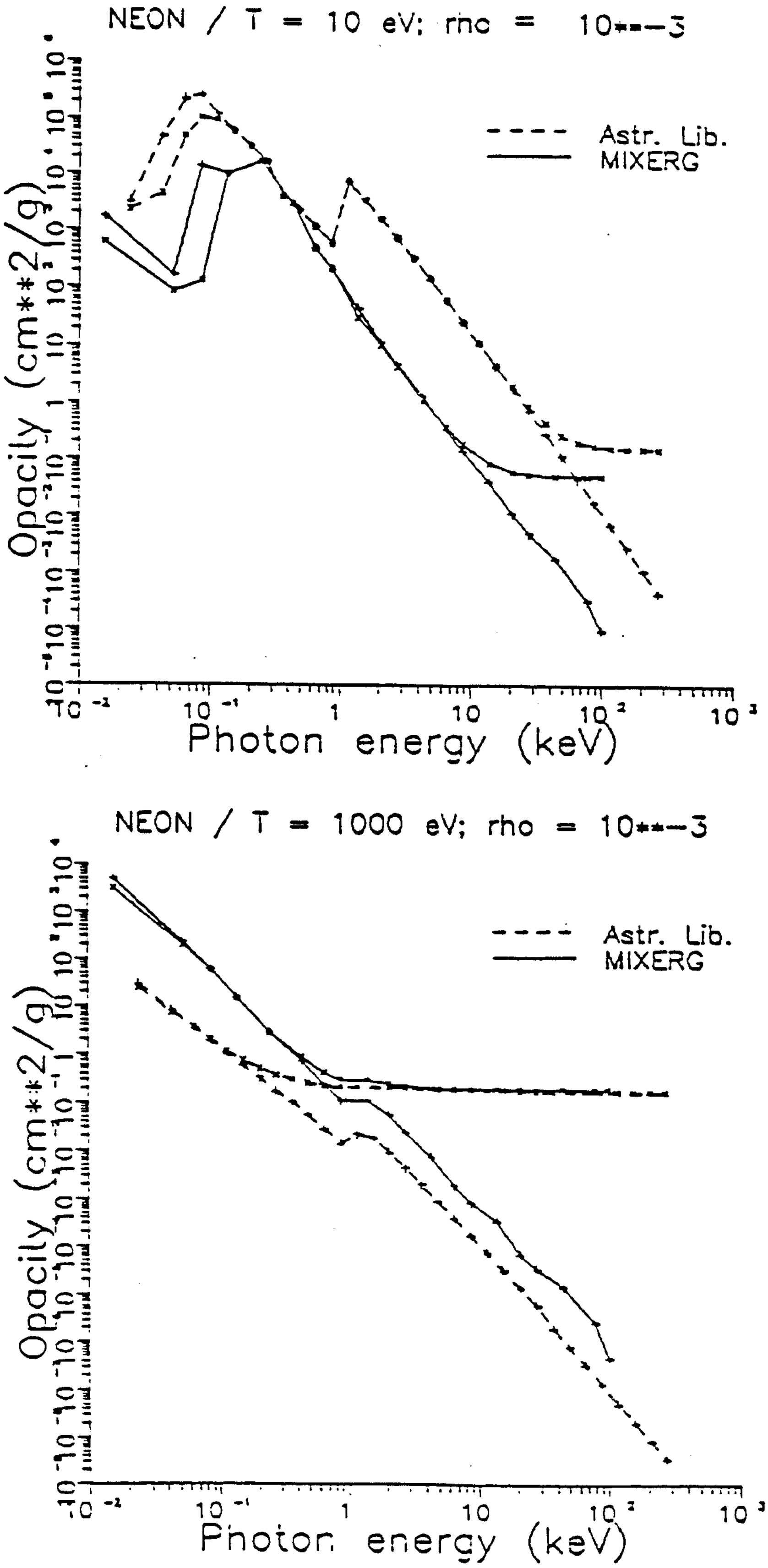

Fig. 2-3. Rosseland and Planck opacities vs. photon energy for neon at temperatures of 10 eV (top figure) and 1000 eV (bottom) computed by MIXERG and the Astrophysical Opacity Library. The Rosseland opacities approach a constant value in the high energy limit.

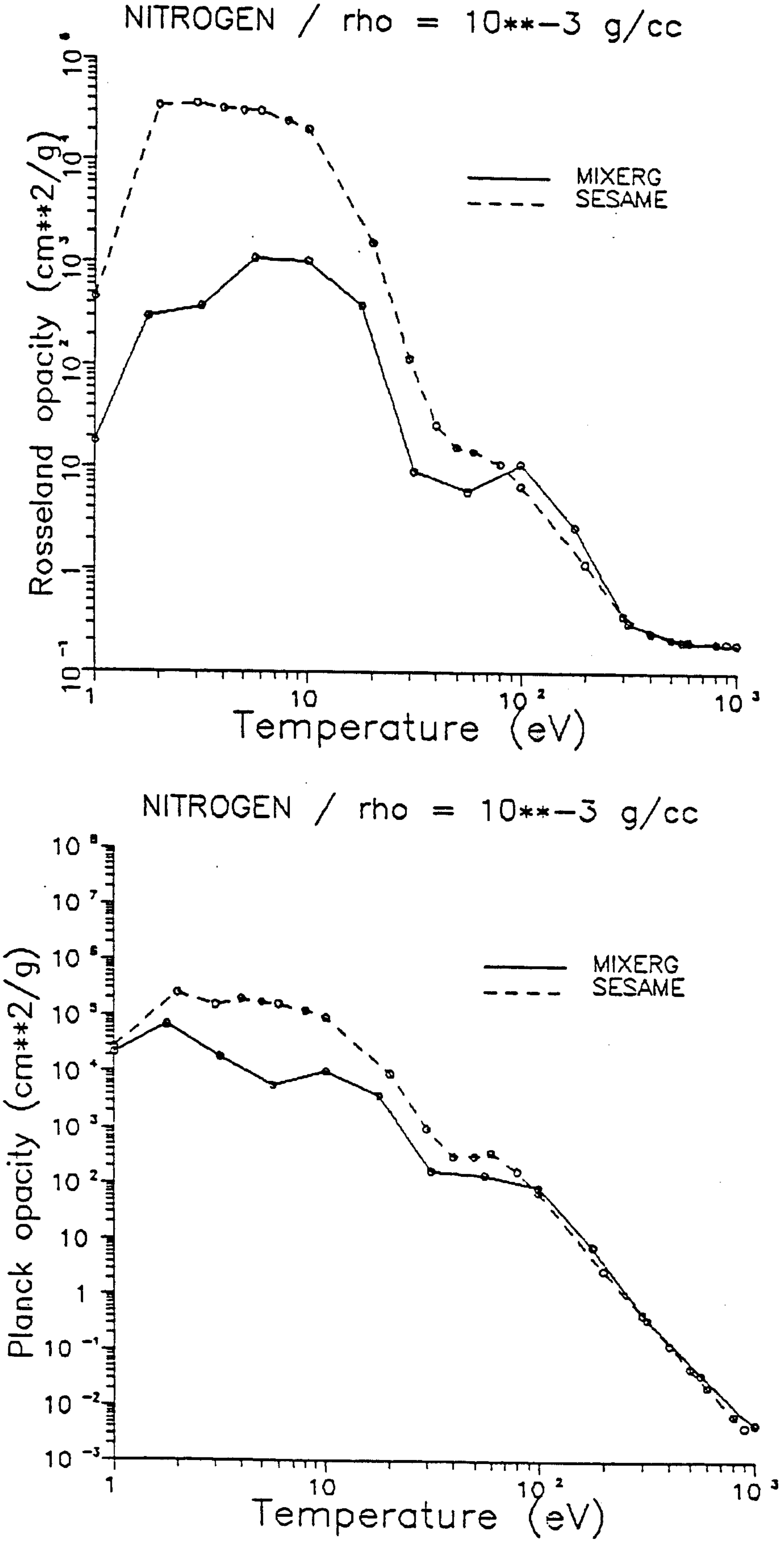

Fig. 2-4. Rosseland (top figure) and Planck (bottom) opacity vs. temperature for nitrogen computed by MIXERG and SESAME. The mass density in each case is 1 x 10^{-3} g/cm^3.

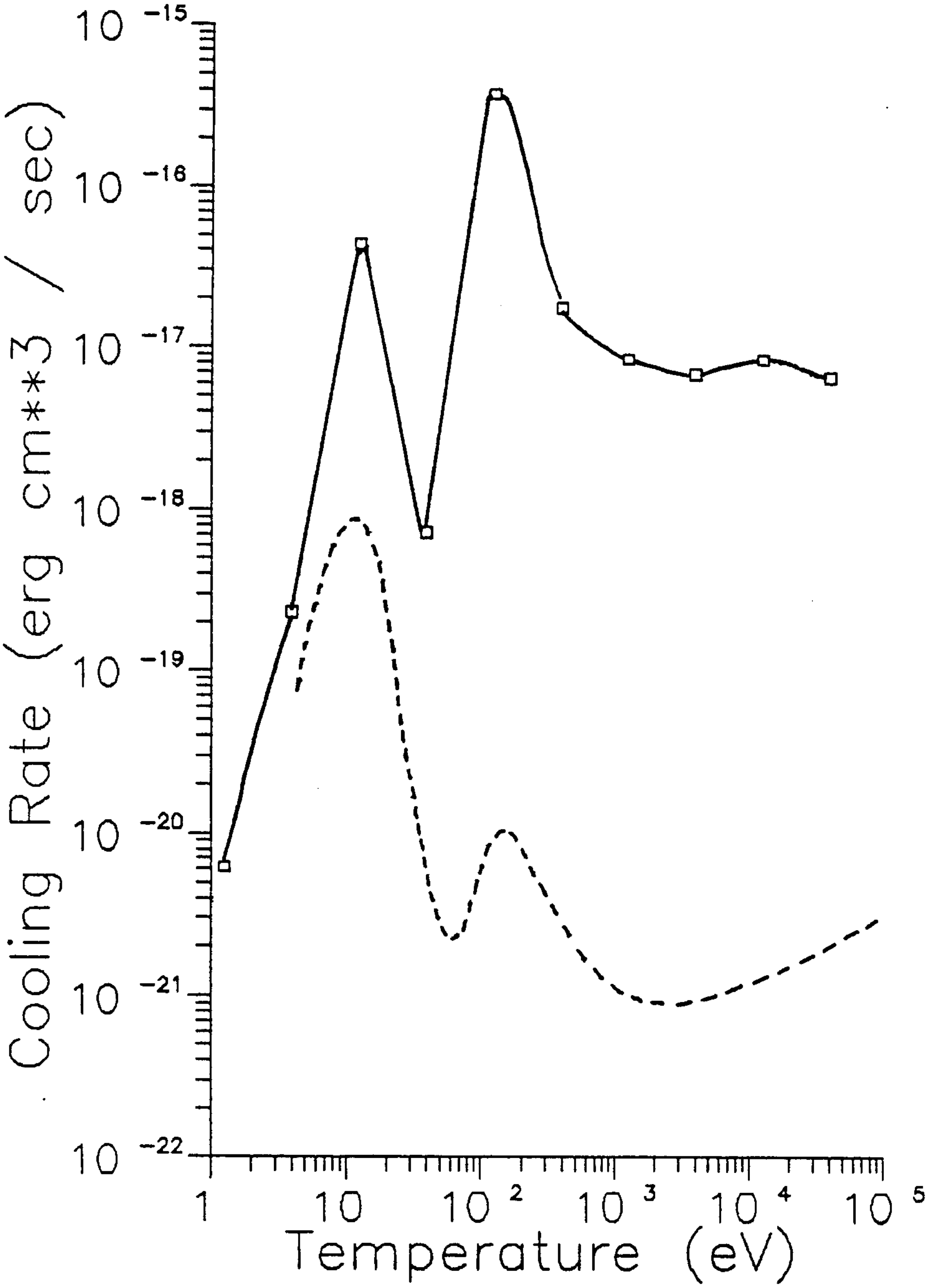

Fig. 2-5. Radiative cooling rate vs. temperature computed by CONRAD with MIXERG opacities (solid curve) and Post et al. (dashed curve) for a low density nitrogen plasma.

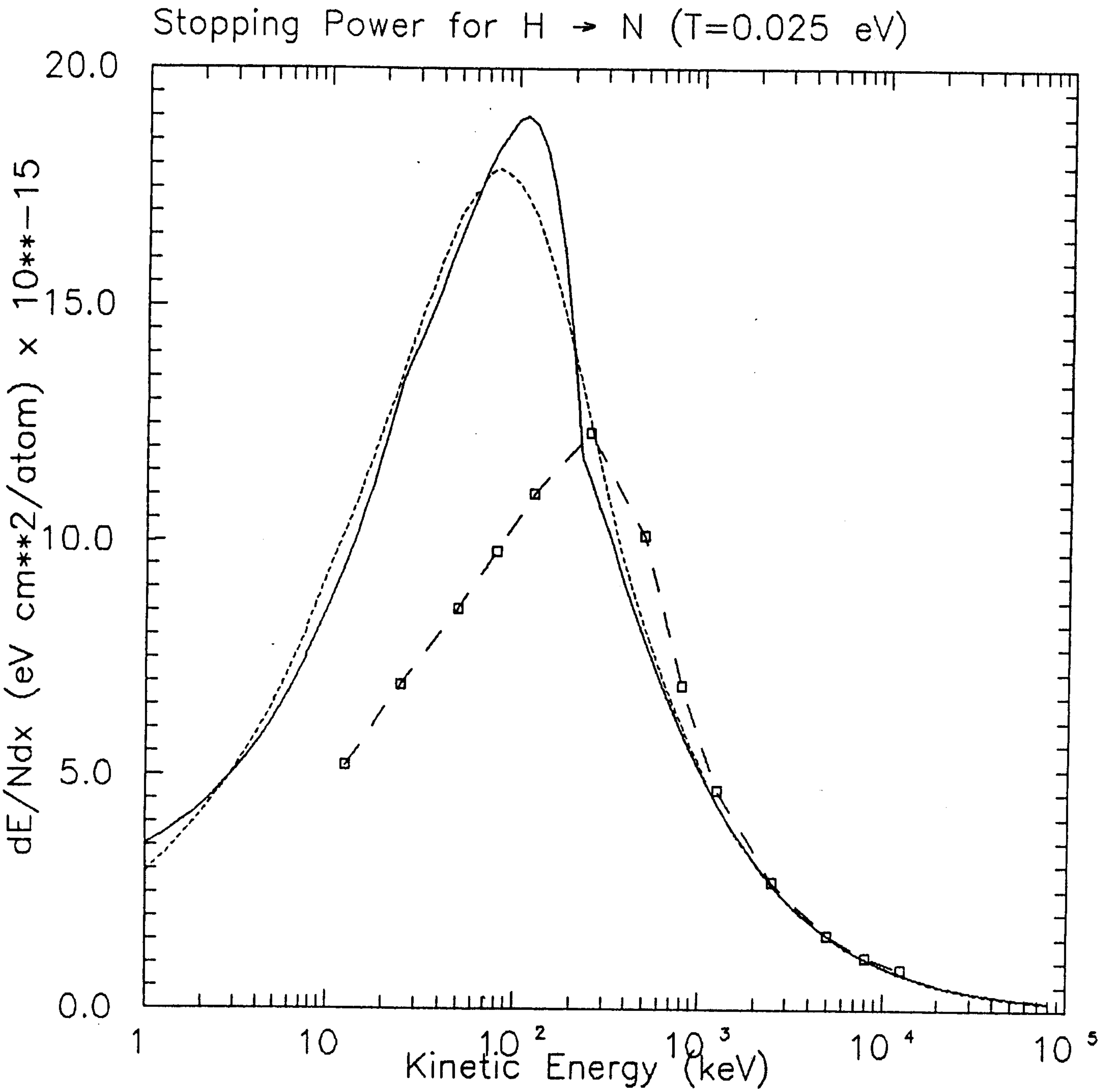

Fig. 2-6. Stopping cross-sections for protons in nitrogen at room temperature as a function of proton kinetic energy. Results are shown for theoretical calculations (solid curve), fit to experimental data (dotted curve), and Northcliffe and Schilling tables (dashed curve).

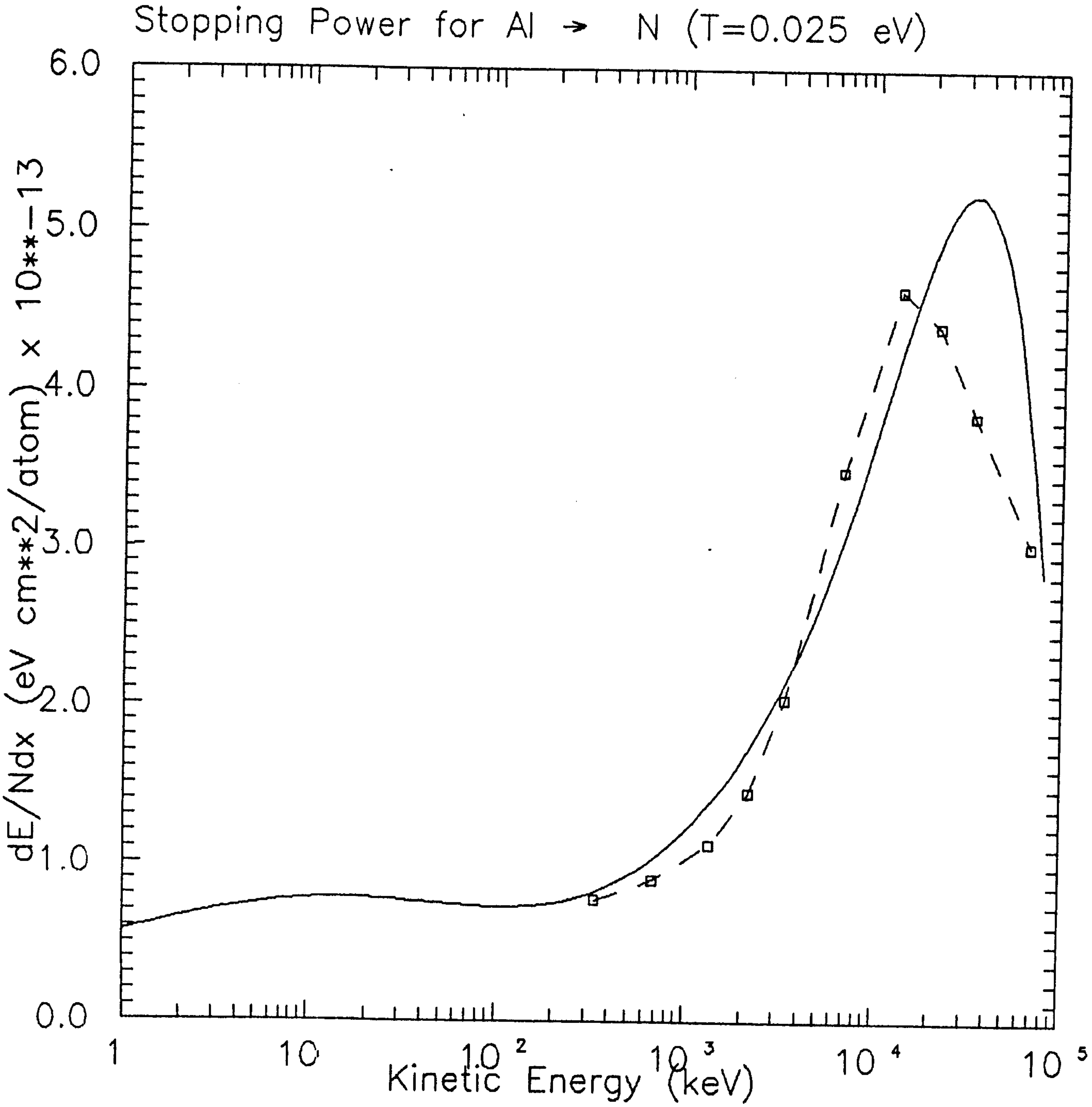

Fig. 2-7. Stopping cross-sections for aluminum in nitrogen at room temperature as a function of aluminum kinetic energy. Results are shown for theoretical calculations (solid curve) and Northcliffe and Schilling tables (dashed curve).

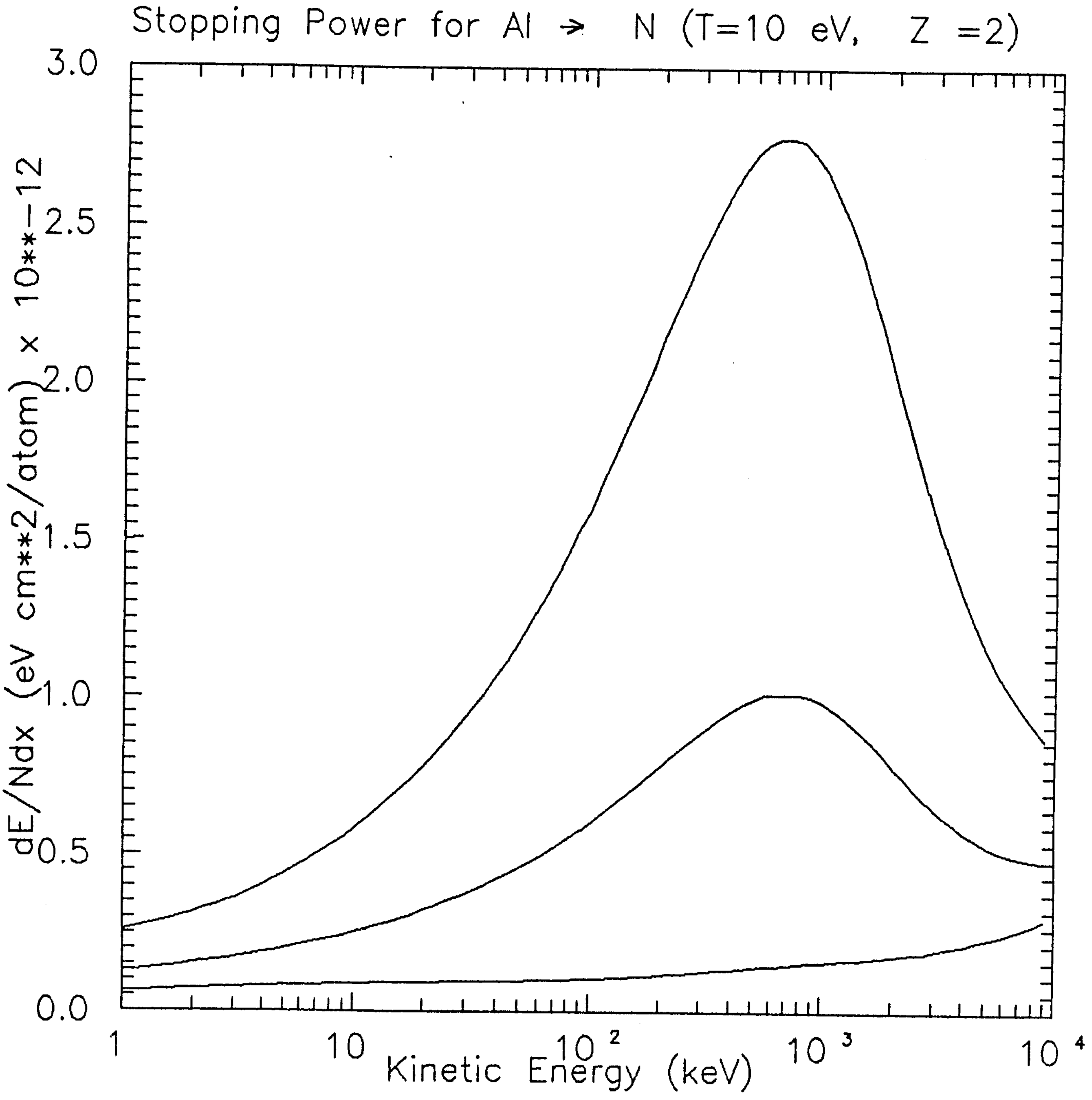

Fig. 2-8. Calculated stopping cross-sections for aluminum in nitrogen at T = 10 eV as a function of aluminum kinetic energy. Curves correspond to Al charge states of 7 (top), 4 (middle), and 1 (bottom).

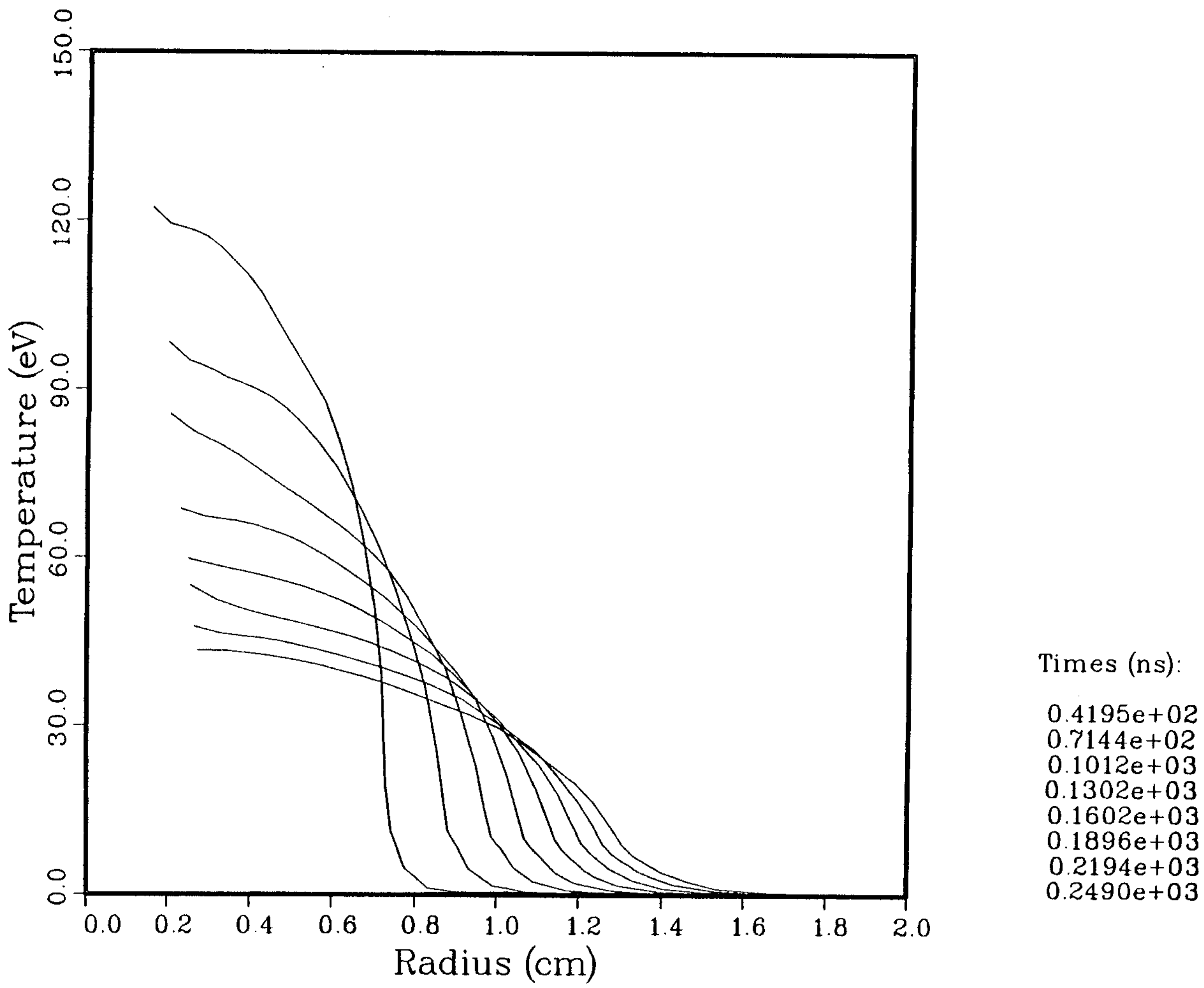

Fig. 2-9(a). Calculated plasma temperature as a function of radius at 8 different simulation times. Total Al kinetic energy was 70 J. Radiation effects were not included.

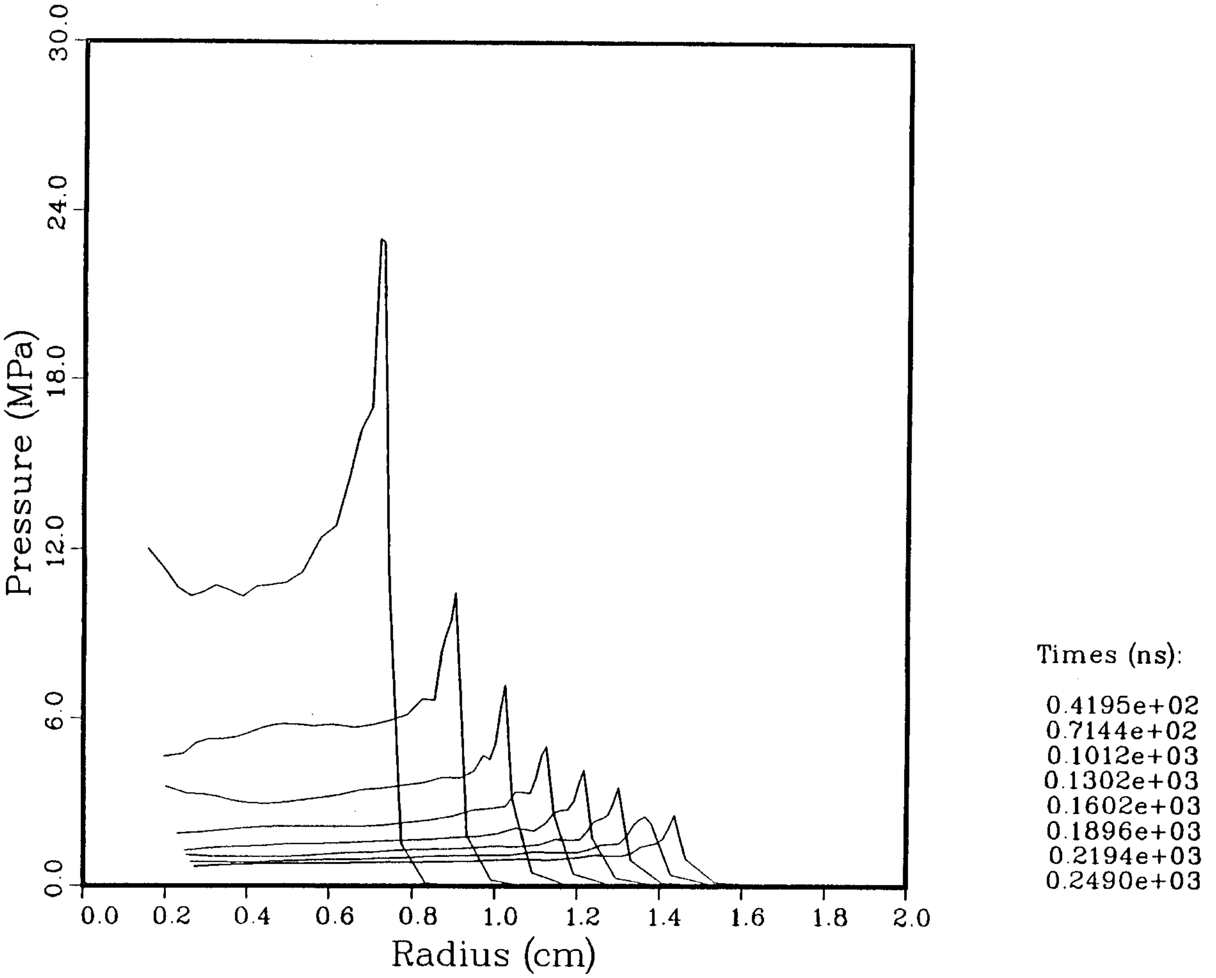

Fig. 2-9(b). Plasma pressure vs. radius (same calculation as Fig. 2-9(a)).

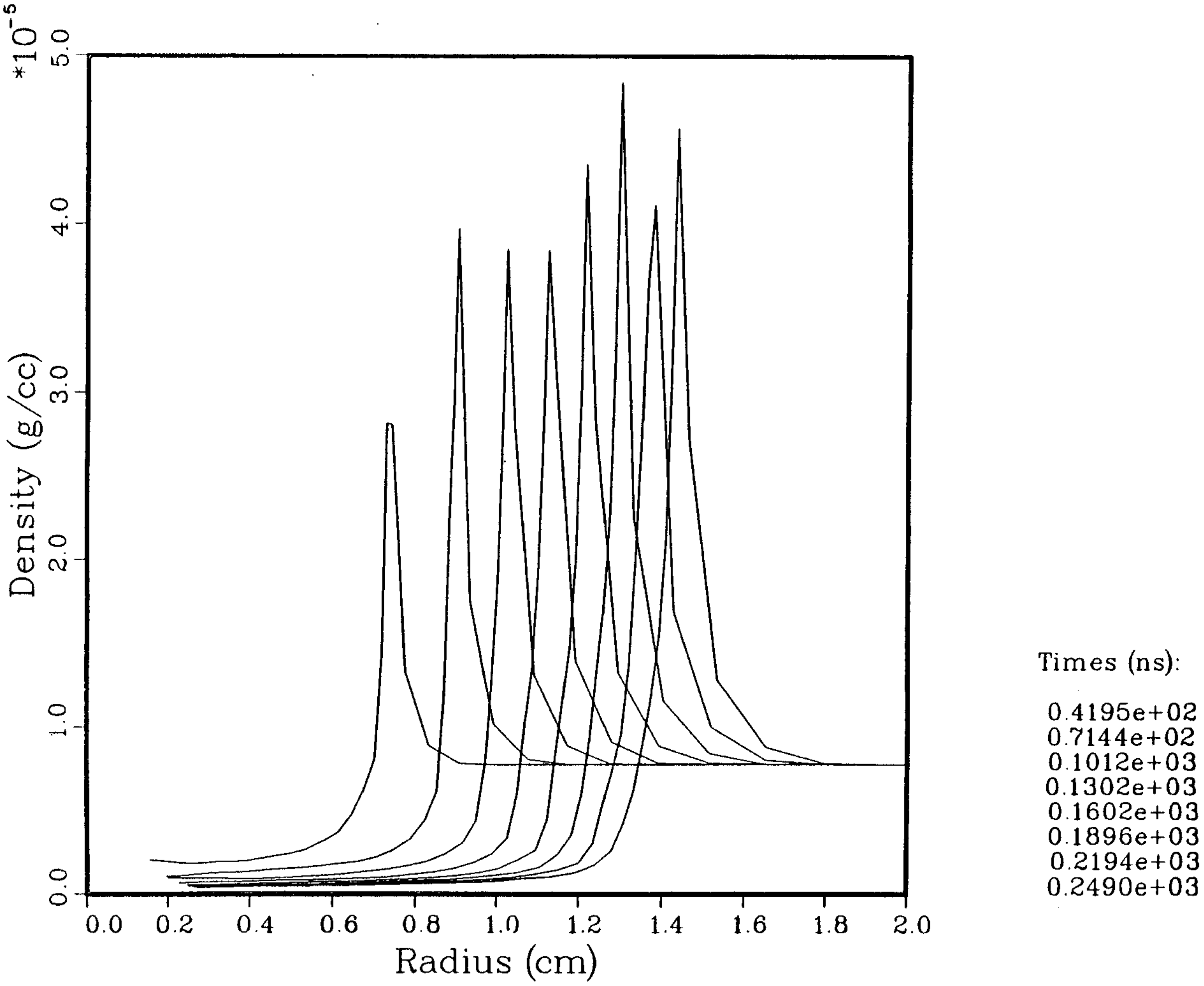

Fig. 2-9(c). Mass density vs. radius (same calculation as Fig. 2-9(a)).

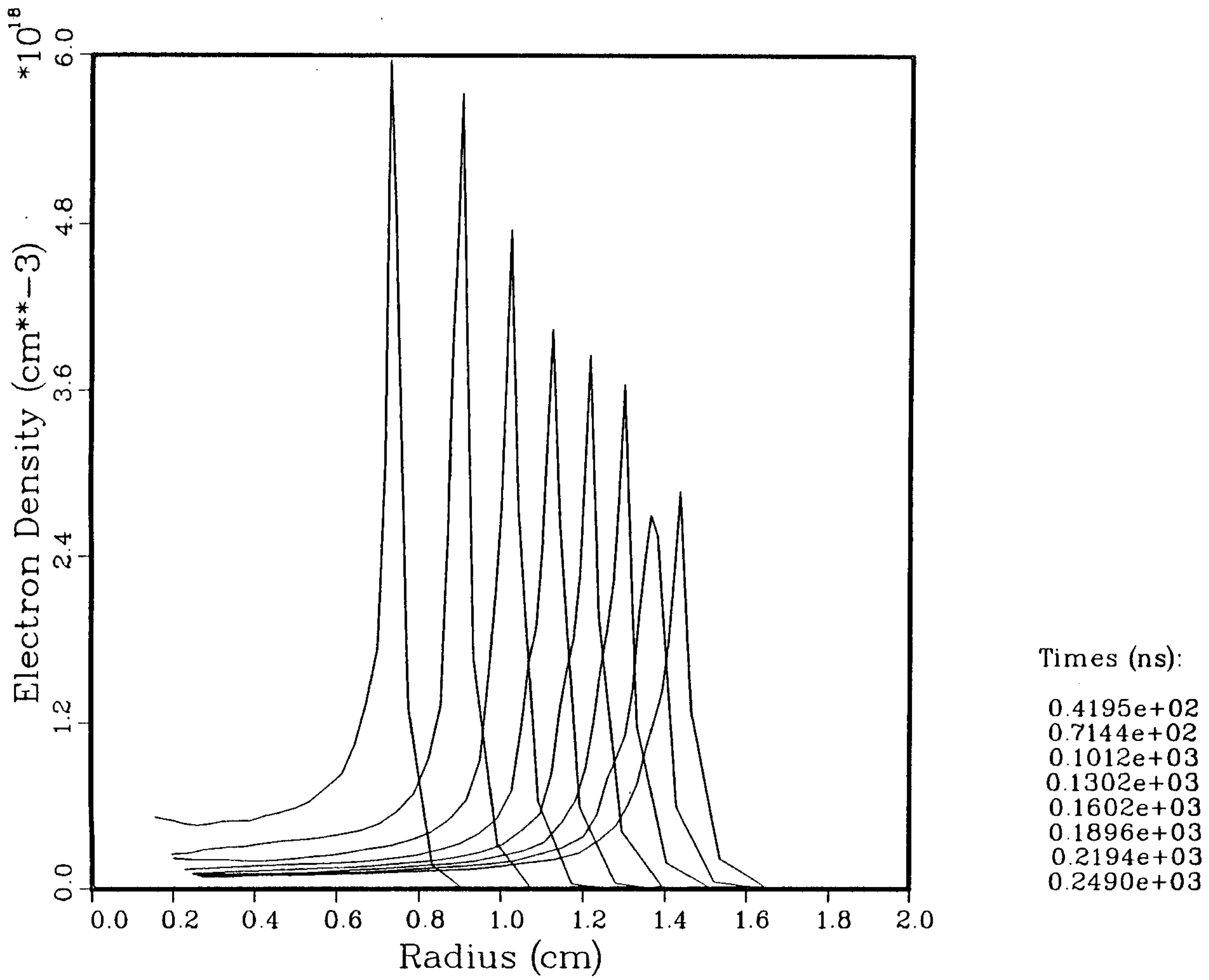

Fig. 2-9(d). Electron density vs. radius (same calculation as Fig. 2-9(a)).

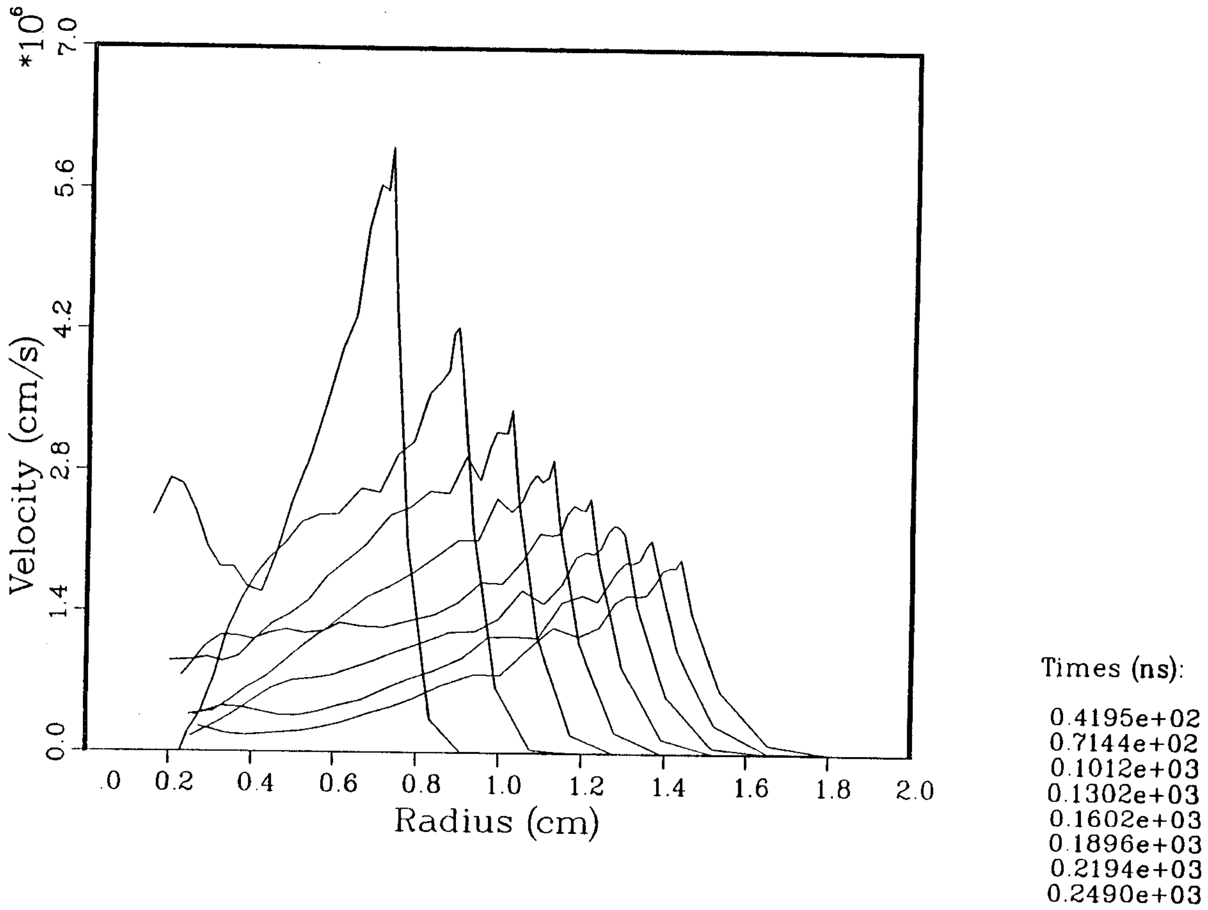

Fig. 2-9(e). Fluid velocity vs. radius (same calculation as Fig. 2-9(a)).

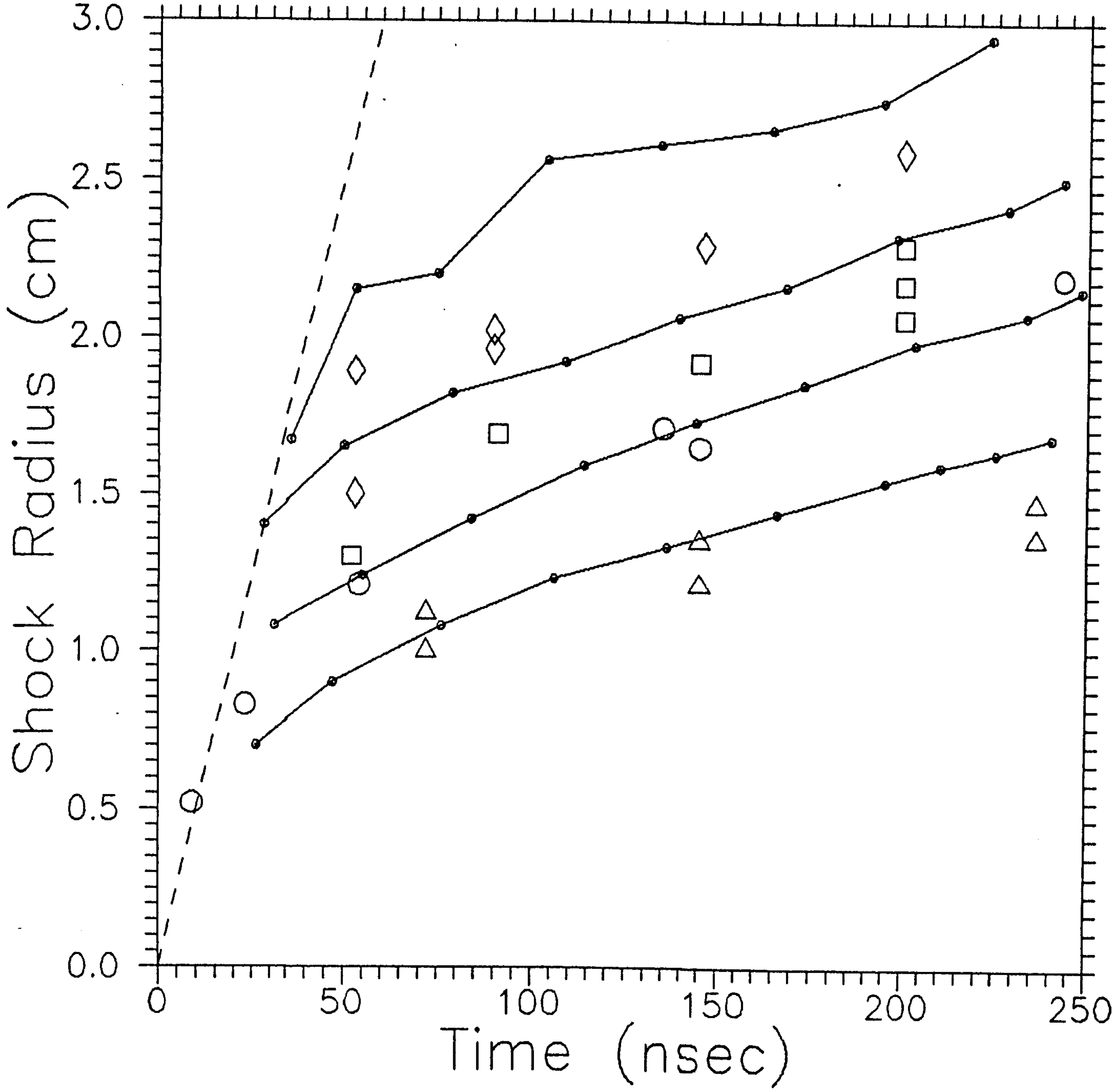

Fig. 2-10. Shock front radius vs. time. Solid curves represent calculated values. Radiation effects were not included. Experimental data as shown for ambient gas pressures of 0.1 torr (diamonds), 0.3 torr (squares), 1.5 torr (circles), and 5.0 torr (triangles).

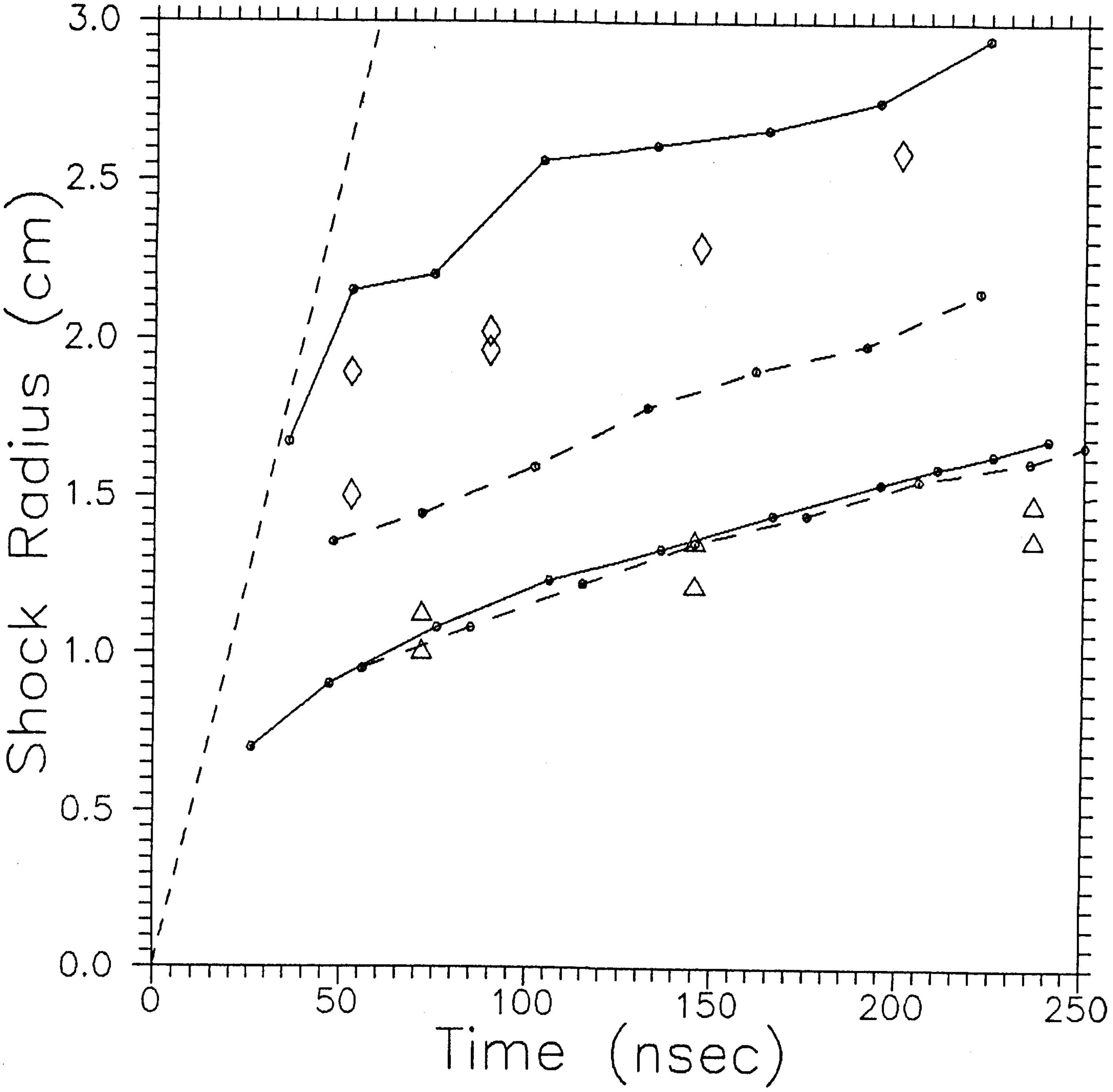

Fig. 2-11. Shock front radius vs. time. Calculated values are shown for Al^{4+} (solid curves) and Al^{2+} (dashed curves) for 0.1 torr (top curves) and 5.0 torr cases. Experimental data are shown for ambient gas pressures of 0.1 torr (diamonds) and 5.0 torr (triangles).

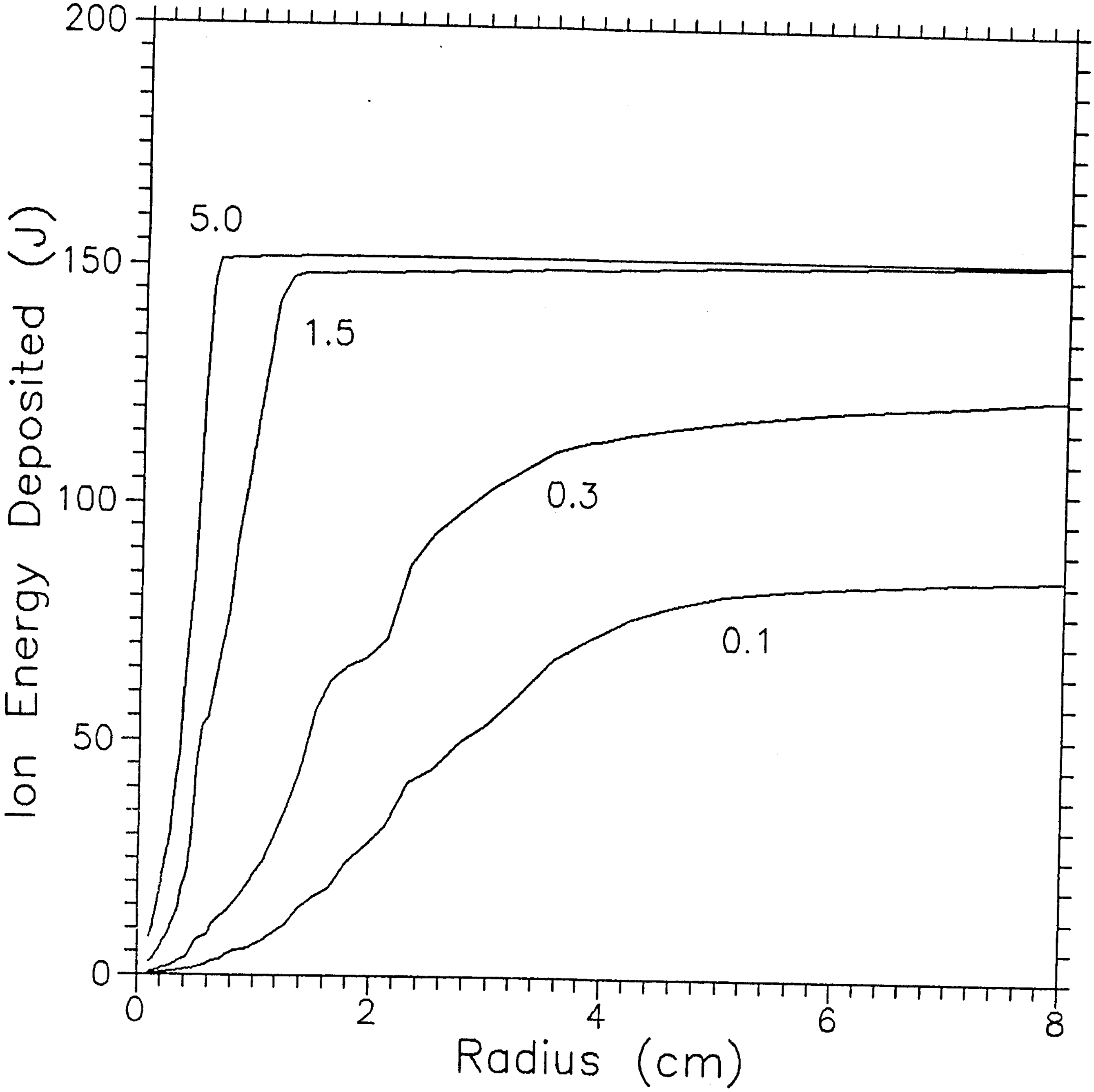

Fig. 2-12. Integrated Al ion energy deposition as a function of radius for calculations with an ambient gas pressure of 5.0, 1.5, 0.3, and 0.1 torr. Total Al ion kinetic energy in each calculation was 150 J.

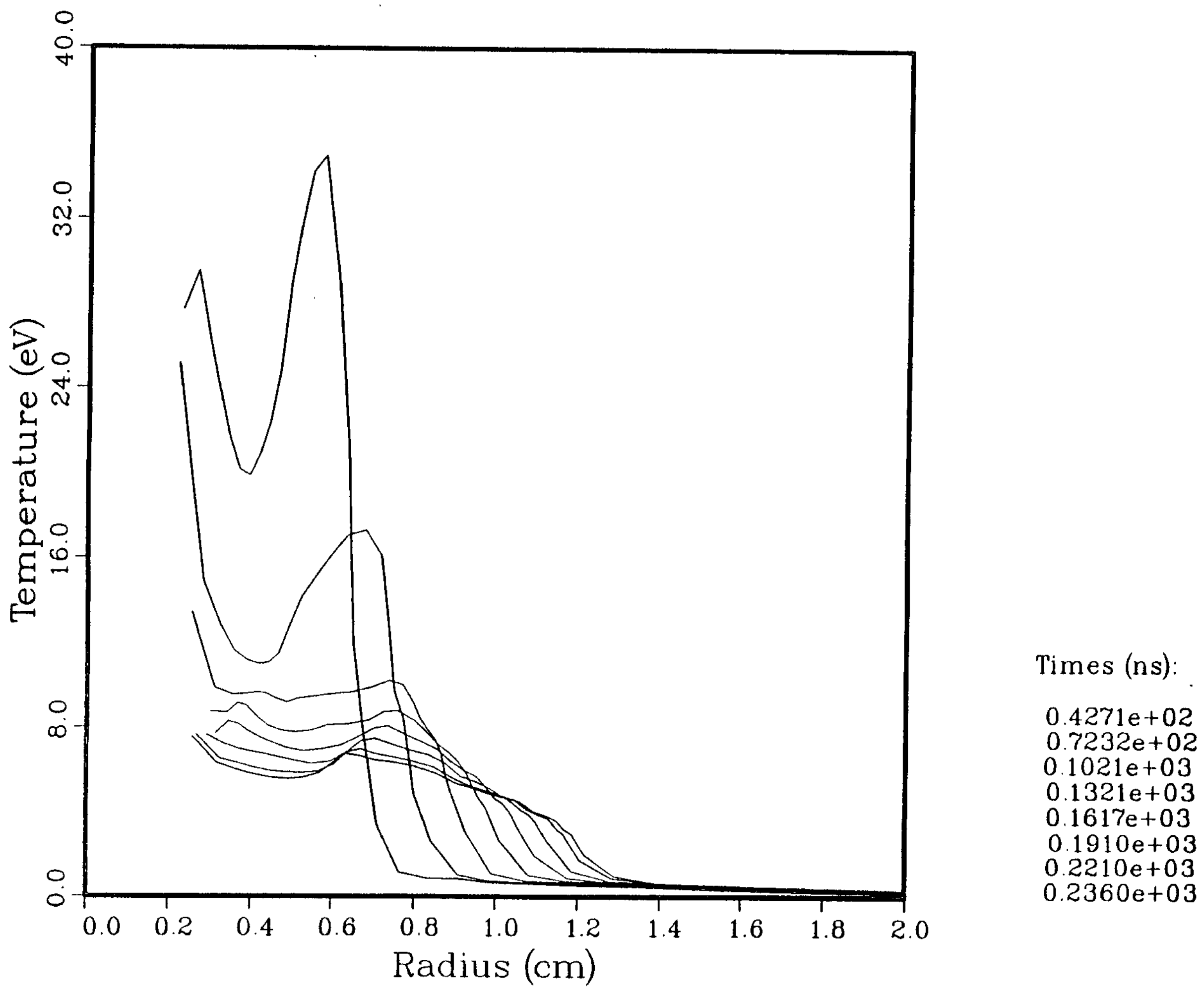

Fig. 2-13(a). Calculated plasma temperature as a function of radius at 8 different simulation times. Total Al kinetic energy was 70 J. Radiation effects were included.

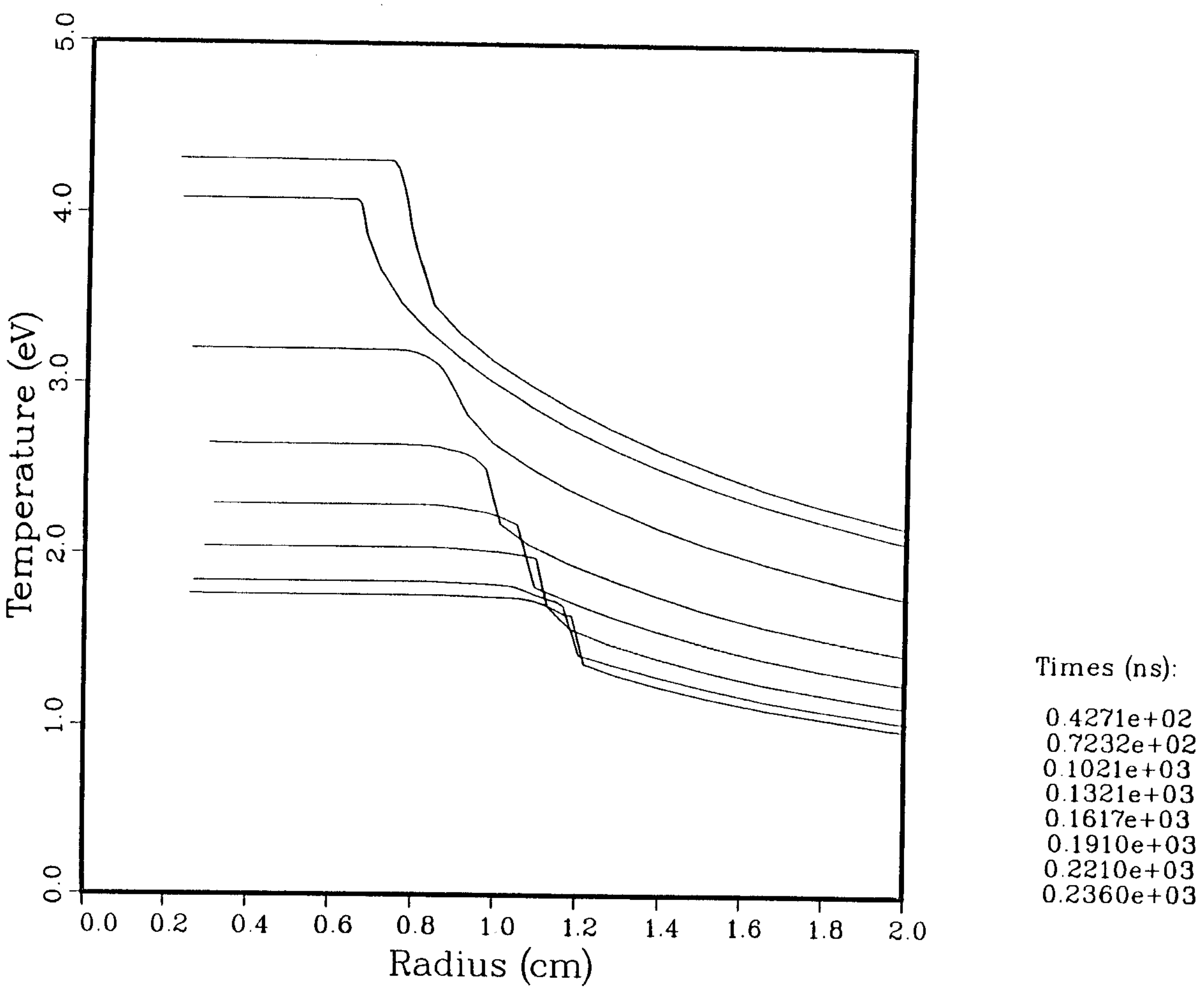

Fig. 2-13(b). Radiation temperature vs. radius (same calculation as Fig. 2-13(a)).

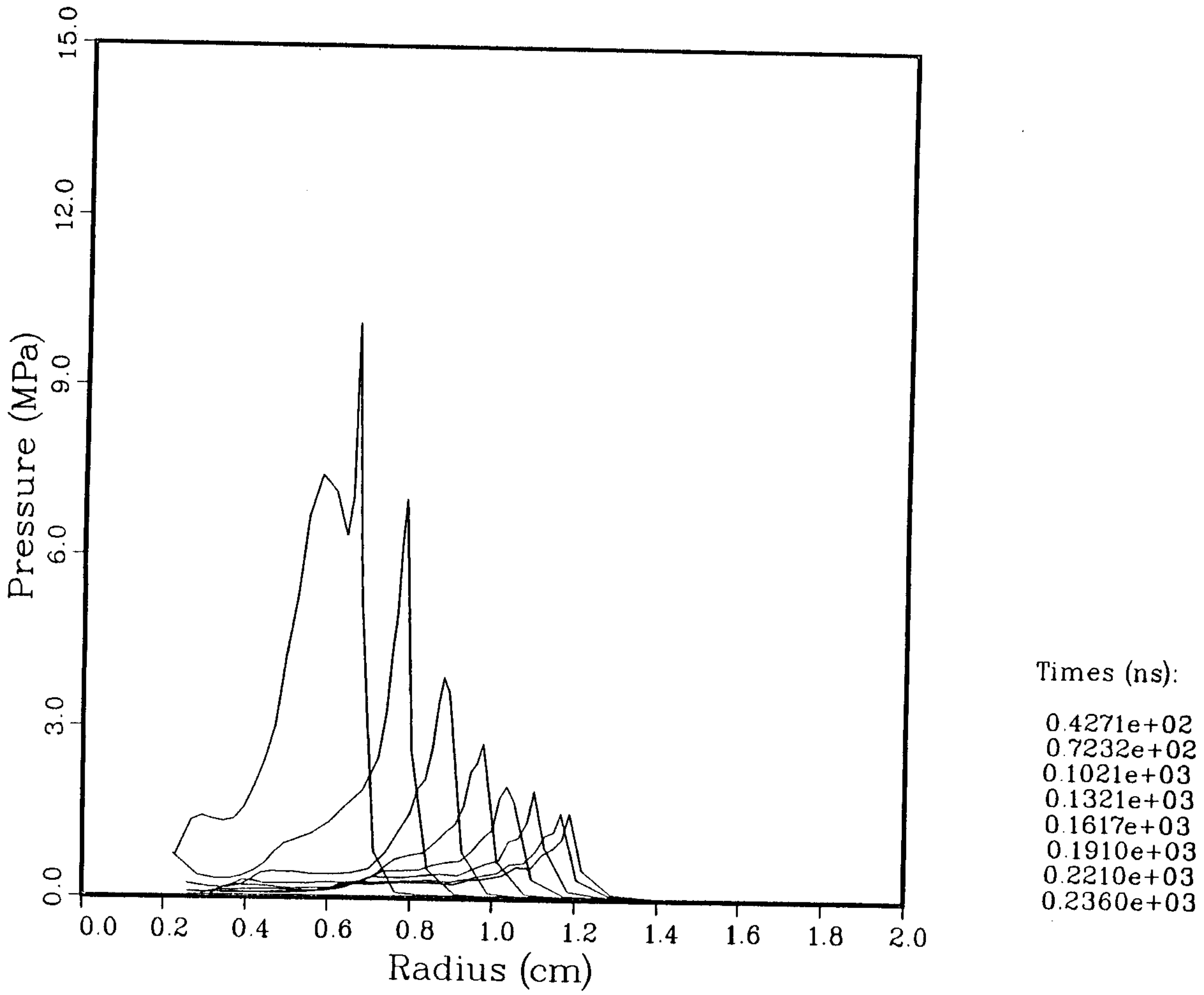

Fig. 2-13(c). Plasma pressure vs. radius (same calculation as Fig. 2-13(a)).

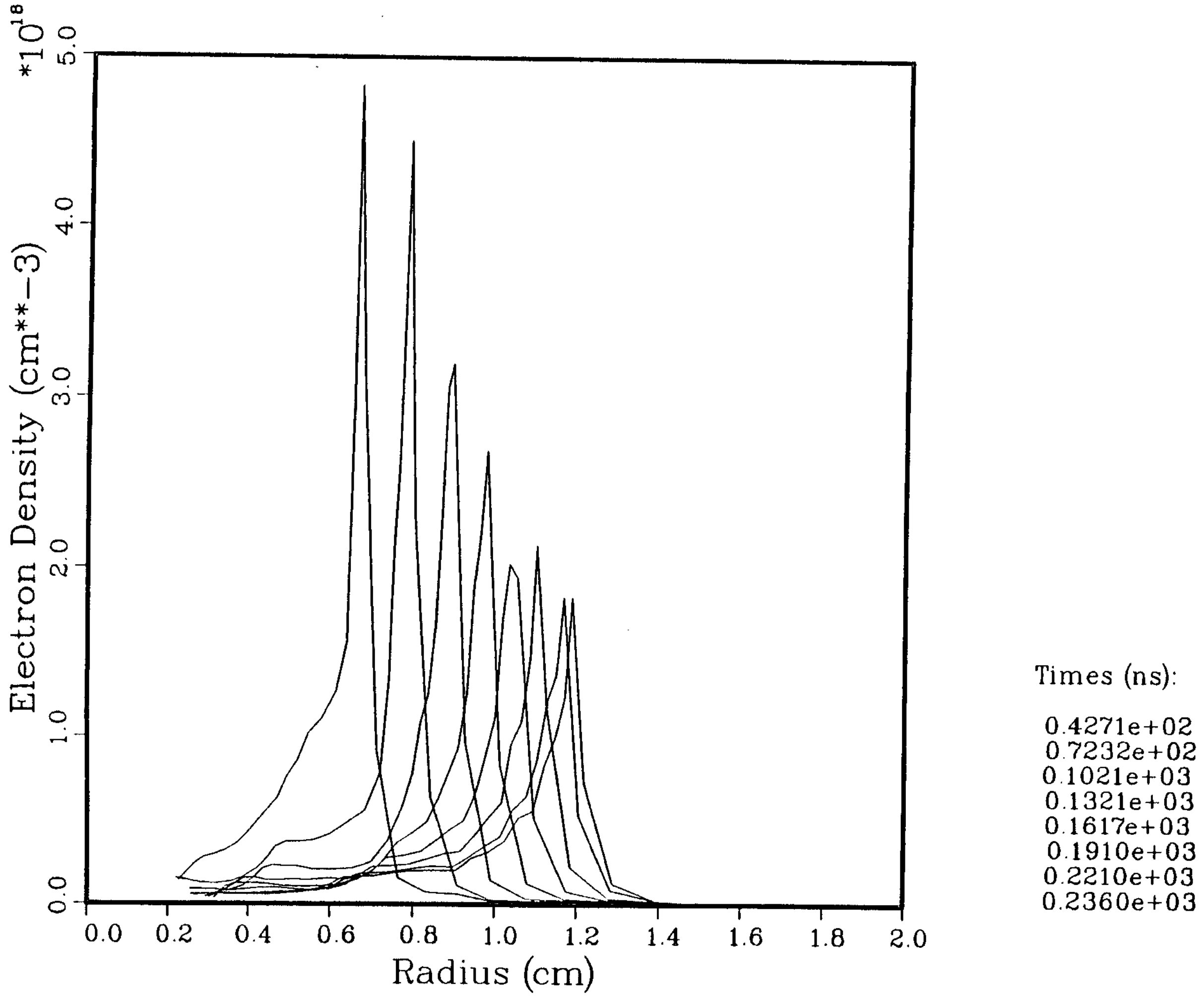

Fig. 2-13(d) Electron density vs. radius (same calculation as Fig. 2-13(a)).

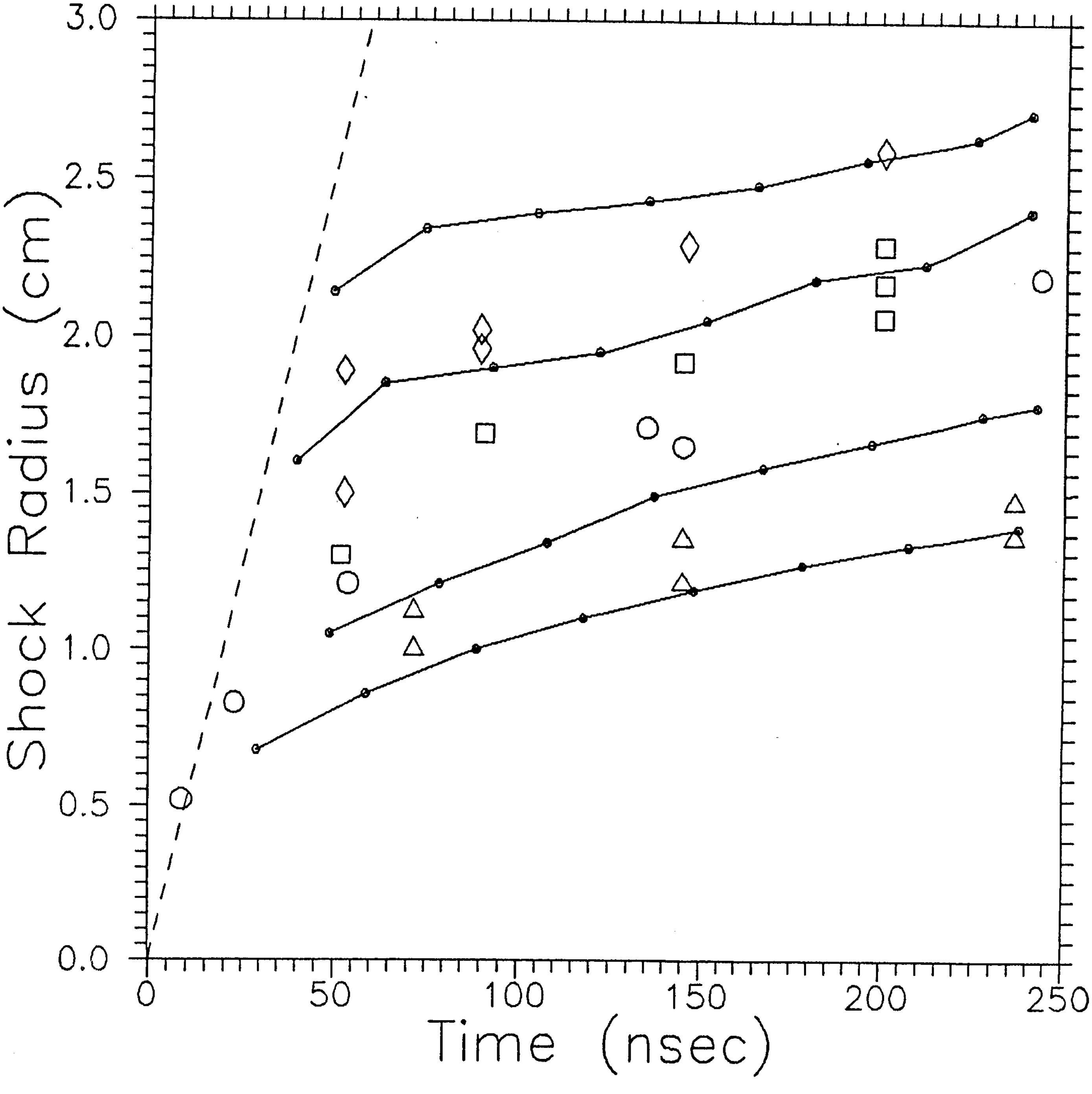

Fig. 2-14. Shock front radius vs. time. Solid curves represent calculated values. Radiation effects were included. Experimental data as shown for ambient gas pressures of 0.1 torr (diamonds), 0.3 torr (squares), 1.5 torr (circles), and 5.0 torr (triangles).

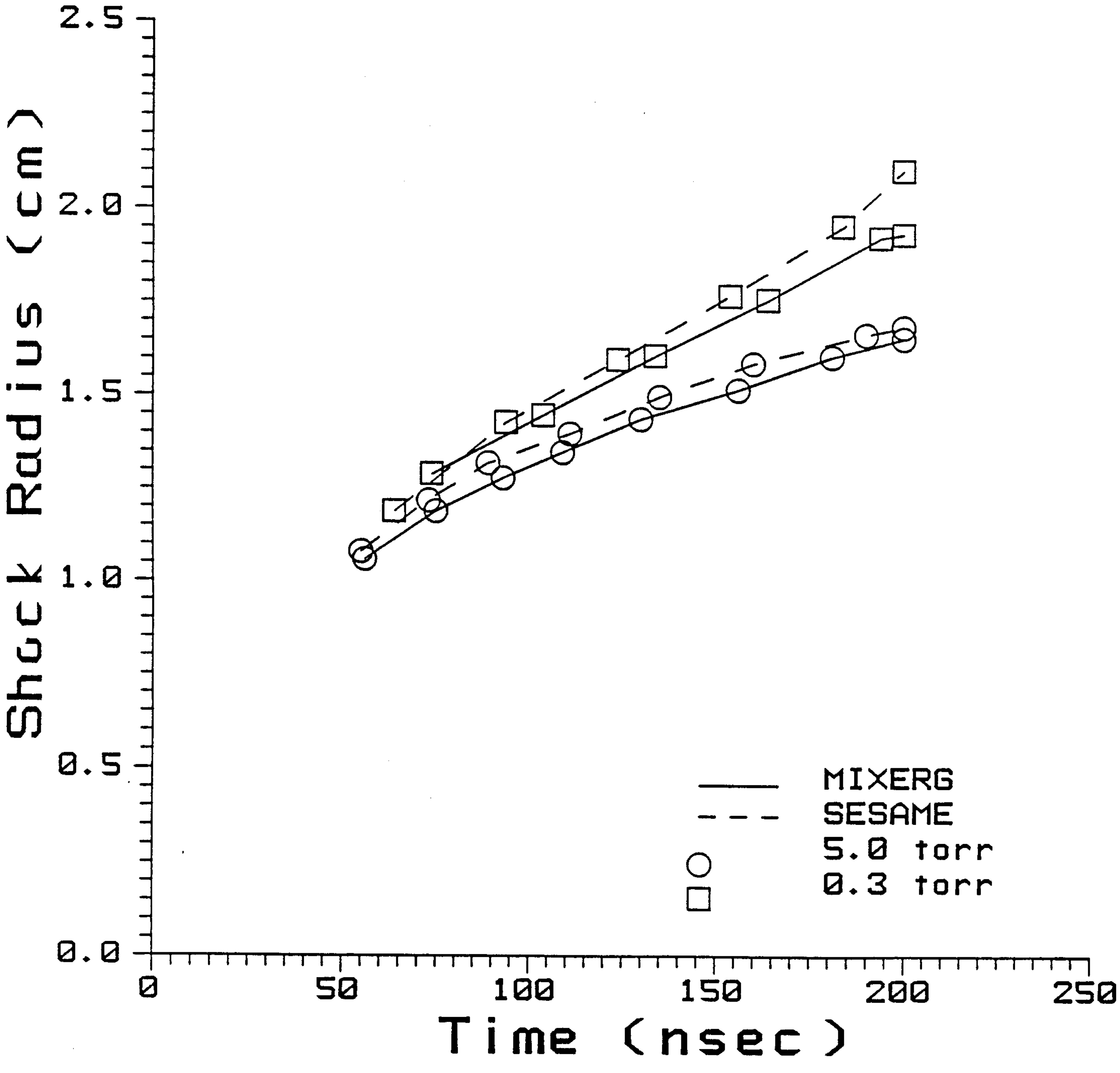

Fig. 2-15. Shock front radius vs. time computed using the MIXERG (solid curves) and SESAME (dashed curves) equations of state. The initial pressure of the neon background gas is 0.3 torr (squares) and 5.0 torr (circles).

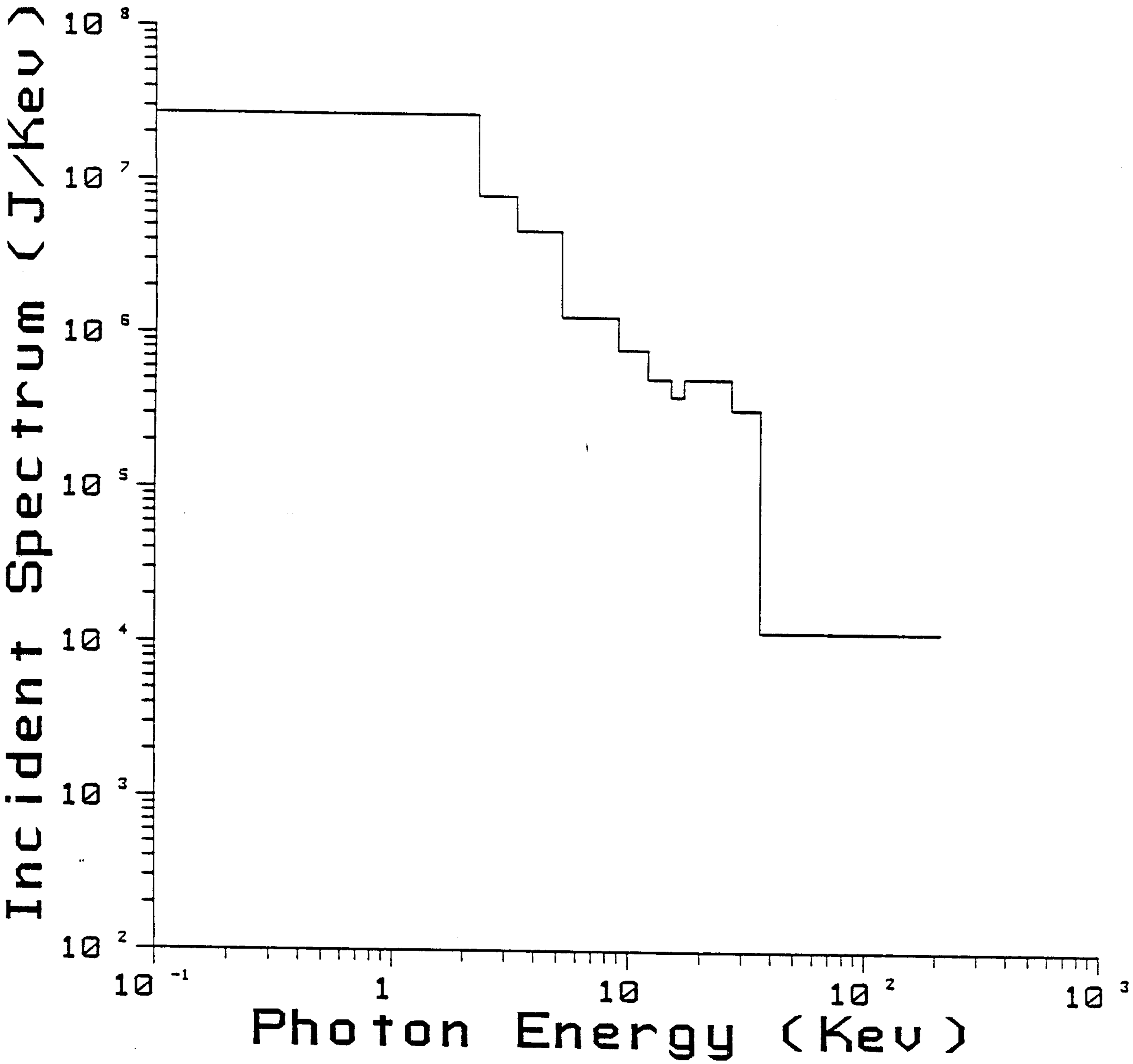

Fig. 2-16. X-ray spectrum for x-ray deposition comparisons.

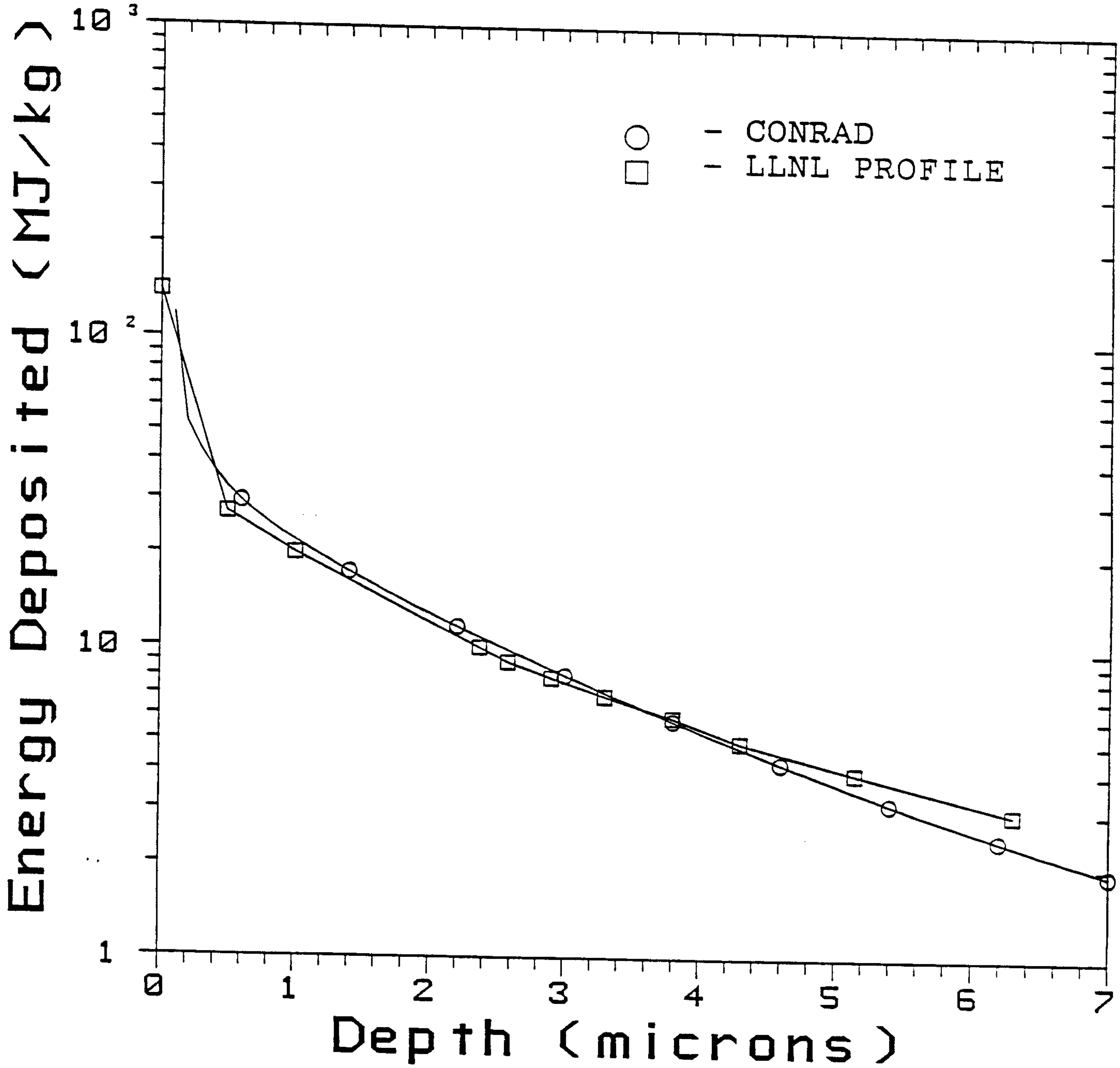

Fig. 2-17. X-ray deposition profiles as calculated with CONRAD and PROFILE.

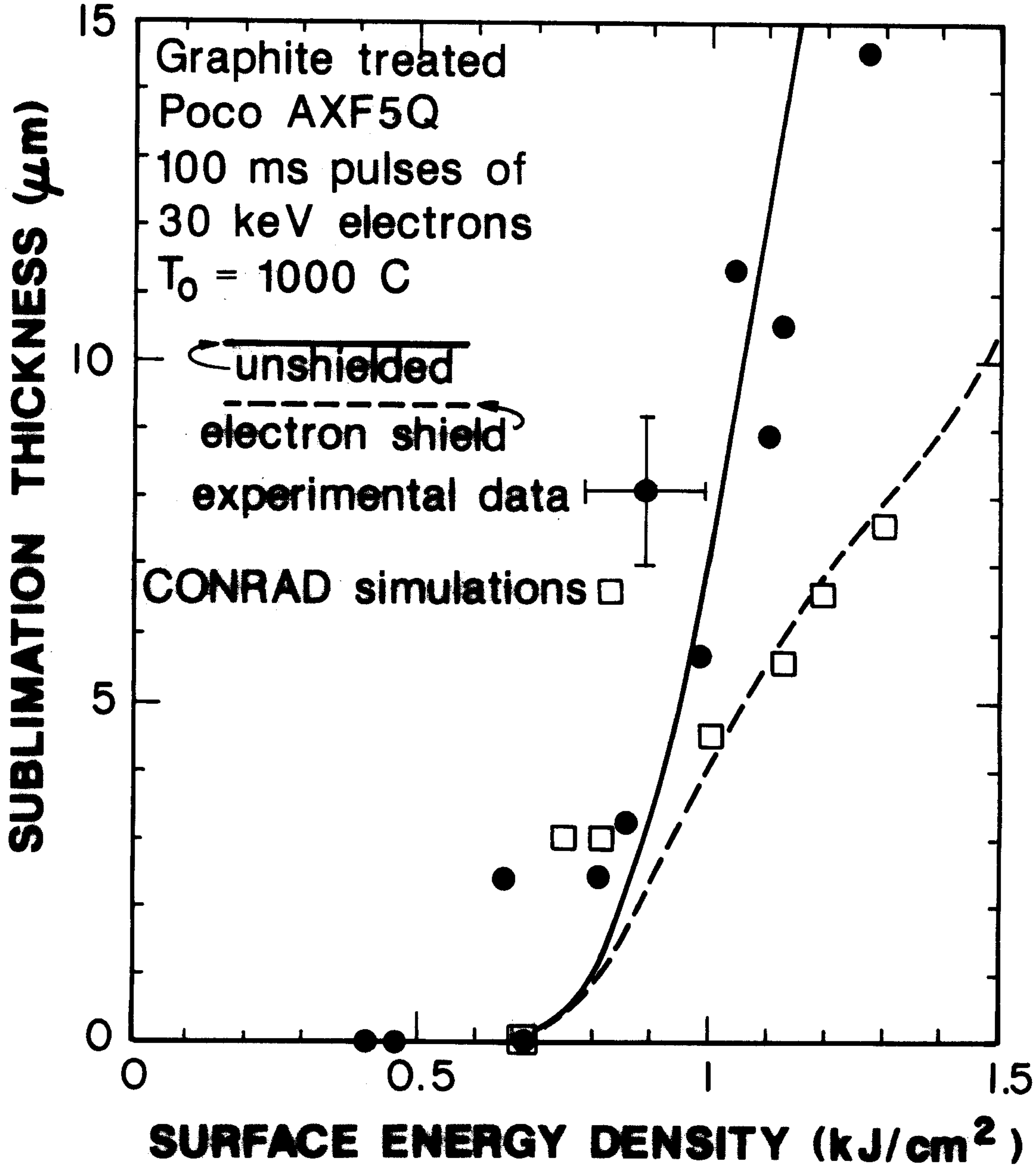

Fig. 2-18. Vaporized thicknesses of graphite for a 30 keV electron beam versus beam energy fluence.

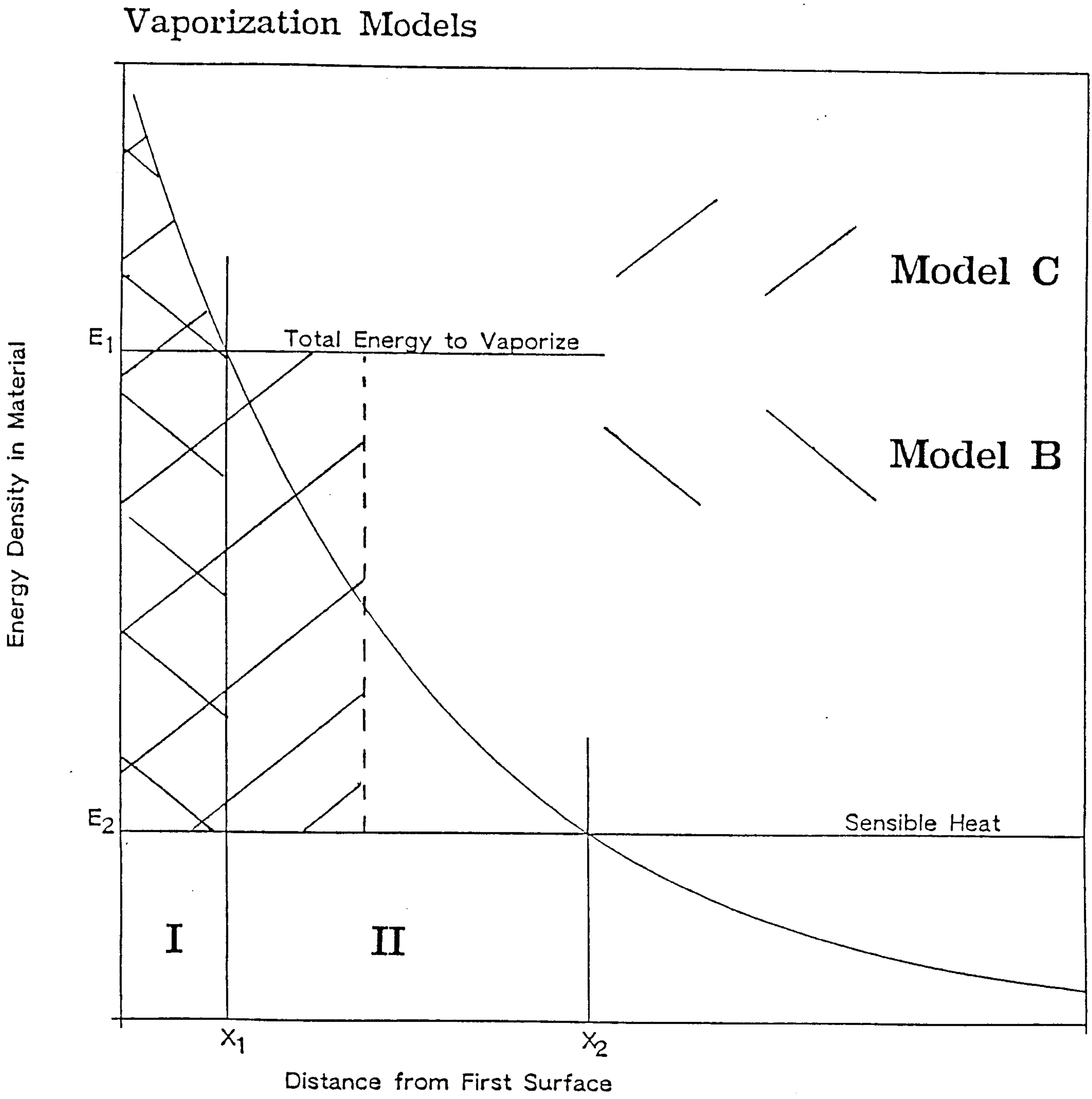

Fig. 2-19. Instantaneous vaporization Models in CONRAD.

3. SMALL SCALE CONDENSATION EXPERIMENTAL DESIGN

3.1 Background

The Inertial Confinement Fusion (ICF) power plant consists of three parts: (1) a primary energy source (e.g., short wavelength laser), (2) a reaction chamber, and (3) an energy removal and power conversion system. The use of liquid metals in ICF reactors allows an efficient energy removal system. The high power density at low pressures and the excellent heat transfer characteristics are features that encourage the use of liquid metals in ICF reactors.

Several design concepts have been proposed to protect the structural wall of the reactor throughout its lifetime and for power conversion. Some of these are: wetted walls, magnetic protection, swirling liquid metal pool, liquid metal stream protection, gaseous protection, and a refractory dry wall.[1-5] Two conceptual designs using a liquid metal protection layer are represented in HIBALL,[6] or LIBRA,[7] and HYLIFE.[1,8,9] Lithium and lithium based alloys are the most attractive liquid metals used in ICF reactors. The main reasons for that are their tritium breeding, their relatively low vapor pressure, and low induced activity. Lithium is very active chemically with oxygen, and thus it must be maintained in an inert atmosphere to prevent reactions with air. Lithium-lead alloys give good breeding properties due to the Pb(n,2n) reaction and have less chemical activity than Li. We summarize representative designs using liquid metals as the heat transfer medium to motivate the present work.

The wetted wall concept uses a thin film of liquid lithium covering the chamber wall for energy removal and wall protection. The lithium or lithium alloy is vaporized by the blast energy, but the wall is not overheated or eroded away. The film must be replenished quickly between shots. One idea is to use porous metal walls through which the liquid lithium flows to replenish the film, but this limits the pulse repetition rate to about 1 Hz or less. Another idea is to use spray nozzles to replenish the lithium film more quickly.[1] The pulse rate of the wetted wall concept is limited by the time required to remove most of the lithium vapor from the chamber atmosphere after each event. To permit effective penetration of infrared laser beams or heavy ion beams, the vapor pressure must be reduced to less than a certain minimum pressure by radiative energy transfer as well as condensation heat transfer at low temperatures before the next event takes place. This minimum pressure depends on the type of the driver beam used. The minimum pressure is estimated to be 100 torr for light ion beam drivers, 0.1 torr for lasers, and about 0.0001 torr for heavy ion beam drivers.

HIBALL (Heavy Ion Beams and Lithium-Lead) is a conceptual reactor design which uses the INPORT (Inhibited Flow Porous Tube) concept to wet the first wall in the

HIBALL reactor. The INPORT tubes are woven SiC tubes which are flexible, sufficient to absorb the energy from x-rays and target debris, while several banks of tubes provide enough Li-Pb alloy to moderate the neutron flux and reduce the total damage in the first wall.[6] A schematic diagram of the HIBALL conceptual reactor is given in Fig. 3-1. An illustration of the INPORT concept is given in Fig. 3-2.[10] Evaporation and condensation for this design were initially analyzed using the Hertz-Knudsen formula:[10]

$$j = j_{cond} - j_{ev}$$

$$j_{cond} = \left(\frac{M_v}{2\pi R_v T_v}\right)^{1/2} P_v$$

$$J_{ev} = \left(\frac{M_v}{2\pi R_v T_s}\right)^{1/2} P_s$$

where: j = net flux to the surface,

j_{cond} = condensation mass flux,

j_{ev} = evaporation mass flux,

T_v = vapor temperature,

P_v = vapor pressure,

T_s = surface temperature,

P_s = surface pressure,

R_v = gas constant,

M_v = molecular weight of vapor.

The results showed that the hydrodynamic motion during evaporation is negligible because the time of evaporation is short compared to the time of recovery after each event. This is why it was better to concentrate on the condensation process in order to determine whether the HIBALL cavity could support the designed 5 Hz repetition rate or not. The general timing of the event along with the relevant physical processes are given pictorially in Fig. 3-3. One notices that condensation heat transfer dominates the time spent between each event. A more detailed model (Fig. 3-4) was developed by Pong in her thesis[10] using the concepts of molecular transport and we are currently pursuing improvements in this model. The results of such analysis (Figs. 3-5 and 3-6) indicate that the condensation process begins after a few milliseconds at temperatures in the range of 3500 to 4500 K and continues until the vapor-gas mixture cools to 800 K in about 200 ms.

The existence of small amounts of noncondensable gas in the cavity, along with the time dependence of the parameters affecting the condensation process in the problem, also makes it quite interesting for fundamental research. This more detailed model is considered for the LIBRA study with greater amounts of noncondensable gases.

LIBRA (Light Ion Beam Fusion Reactor) is a reactor driven by high current light ion beams transported through preformed plasma channels. The first wall is protected by INPORT units similar to those used in the HIBALL design. The front rows of the tubes have a small diameter and the back rows have a large diameter. The designated repetition rate is expected to be 1 to 3 Hz. The cavity design is similar to that of HIBALL. The cavity is filled with argon at a pressure of 10 torr. The gas serves to absorb the non-neutronic target yield in a small volume around the target forming a fireball. This absorption protects the first wall from damage due to direct target debris. The gas cools down by flowing through an array of INPORT tubes[7] for increased surface area by conduction, convection, and radiation heat transfer. A computer code called CONRAD has been developed[11] to solve the gas hydrodynamic motion in a one-dimensional Lagrangian coordinate system.

HYLIFE is a laser driven ICF concept that uses a curtain of liquid lithium to protect the first wall from target emanations. The lithium curtain is vaporized and broken up by the rapid absorption of neutrons, x-rays and ions. The path that the lasers follow to the target must be cleared of vapor and pieces of lithium before the laser can be fired again. Therefore, condensation is an important consideration in determination of the repetition rate.

Some reactor designs, such as CASCADE,[12] involve the vaporization and recondensation of solid first wall material. One version of CASCADE has a graphite first surface. The physics of the condensation of graphite is greatly complicated by the creation of molecules of carbon when the material is in the vapor phase.[13] CONRAD has been used to calculate the allowable rep rate in CASCADE to be rather high.[14]

The most important point to note is that these liquid metal condensation models have yet to be verified experimentally. This is the major thrust of the current work. The next section will summarize our conceptual design of the condensation experiment.

3.2 Feasibility Design of Experimental Apparatus

To verify the mechanistic model being developed for liquid metal condensation at low particle densities (10^{22}-$10^{23}/m^3$) we have proposed a small-scale condensation experiment. The major features of the experiment are a relatively simple geometry along with known initial conditions and boundary conditions. A liquid metal sample would be vaporized in a known gas atmosphere and mix with the gas as it cools and condenses onto the surrounding structure of the apparatus. If one can determine the final conditions of the gas-vapor mixture and surrounding structure the heat transferred to the surroundings can be determined and the condensation rate inferred. The condensation rate inferred from the experiment can then be compared to the model which is being developed.

The first consideration is the initial temperature of the vapor that is condensed during the test. We have considered the HIBALL design study[6] to help us determine this value. If one considers the simple lumped parameter analysis used in HIBALL (Figs. 3-3 through 3-6) one finds that condensation is predicted to begin at a temperature of about 4500 K. At this temperature the vapor has lost much of its energy by radiative transfer and has desuperheated as the wall temperature has fallen below the vapor dew point. Such a temperature would probably be the upper bound temperature achievable from a practical viewpoint in the experimental apparatus. One final consideration is that the initial temperature chosen should be low enough that the ionization of the vapor would be minimal. This is important so that no large induced magnetic fields would be produced that would influence vapor fluid motion during condensation. This would make our experimental analysis efforts too complex and the resulting test data too ambiguous. Table 3-1 gives the result of our analysis that indicates if the peak vapor temperature is kept below 4000-4500 K the ion density will be less than 1% of the total particle density. This implies to us that the plasma effects will be small and the bulk of the gas-vapor mixture could be considered neutral.

The next consideration for initial conditions is what should be the characteristic dimension of the condensation chamber. The criteria used to determine this would be to assure that the vapor-gas bulk mixture behaves as a continuum during the whole condensation process as is the case under ICF conditions. As the vapor condenses and cools and the pressure decreases, the particle density decreases causing the mean free path of the particles to increase significantly. Under the design conditions for HIBALL (Figs. 3-3 through 3-6) this implies the mean free path becomes a significant fraction of the chamber dimension (~ 1 m), as the vapor cools to its original temperature (800 K) and pressure (10^{-2} torr). However, the bulk vapor-gas mixture appears to still remain as a continuum. In the design of our test chamber we have chosen to maintain this same condition; i.e. the bulk vapor-gas mixture behaves as a continuum throughout the process. The limiting set of conditions that would determine the chamber characteristic dimension would occur at the end of the condensation process when the pressure and temperature are low as is the corresponding particle density. We considered a temperature of

Table 3-1. Ion Particle Density as a Function of Temperature

Temperature (K)	Ion Density (atoms/m^3)	Ion/Particle Density	Debye Length (μm)
8500	1.22 (10^{23})	0.994	0.0183
8000	0.86 (10^{23})	0.704	0.02
7500	0.58 (10^{23})	0.477	0.025
7000	0.37 (10^{23})	0.306	0.03
6500	0.225 (10^{23})	0.185	0.037
6000	0.124 (10^{23})	0.103	0.048
5500	0.063 (10^{23})	0.052	0.065
5000	0.028 (10^{23})	0.023	0.092
4500	0.01 (10^{23})	0.0084	0.146
4000	0.003 (10^{23})	0.0025	0.19

800 K and a pressure of 10^{-2} torr for this estimate, which is in agreement with HIBALL conditions before the next target explosion. Based on these conditions one finds that the smallest dimension for the test chamber would be about 0.3 m. This is calculated based on the requirement that the characteristic dimension of the chamber be an order of magnitude larger than the largest mean free path of the particles (0.03 m) at the given particle density.

Another issue that must be considered is the scaling from the ICF reactor condition to the small scale experimental chamber. We have again used the HIBALL design as our guide. If one keeps the pressure and temperatures the same under the small scale conditions as in the prototypic reactor while using similar materials, that implies that the mass and energy scaling will be proportional to the cube of the scale factor (L^3). Based on these scaling laws the estimates for the mass and energy requirements for the small scale experiment are provided in Table 3-2. One should note that kinetic effects during the production of the high temperature vapor, that have not been accounted for as yet, may limit the actual mass of liquid metal vaporized. In these calculations we assumed the lithium-lead alloy ($Li_{17}Pb_{83}$) used in the ICF designs[6,7] would be initially utilized in the experiments.

Table 3-2. Scaling from Reactor to Experiment

$P = 50$ torr

$T = 4500$ K

$\Delta t = 1.8 \times 10^{-3}$ s

$\rho = 3.53 \times 10^{-5}$ g/cm^3

$E_V = 2800$ J/g @ 4500 K

Radius	Total Energy (kJ)	Mass (g)
20	3.3	1.2
25	6.5	2.3
30	11.2	4.0
35	17.7	6.3
40	26.5	9.5
45	37.7	13.5
50	51.7	18.5
55	68.9	24.6
60	89.4	31.9

Reactor: 18 kg with R = 500 cm (HIBALL)

The small scale of the proposed apparatus also implies other important characteristics of the experiments. First, one might look at the scaling of the condensation heat transfer, ΔQ_c,

$$\Delta Q_c = \int_0^{\tau} h_c A \, \Delta T \, dt \qquad (3\text{-}1)$$

where: h_c is the condensation heat transfer coefficient

A is the structure surface area

ΔT is the vapor-structure temperature difference

t is the time and τ is a characteristic time.

By the assumed scaling laws the time for the whole process ought to be reduced by the inverse of the scale factor (1/L). For HIBALL conditions, as shown in Table 3-3, this suggests a reduction in the characteristic time of 0.06 and a complete condensation process

Table 3-3. Liquid Metal Condensation Experiment

CURRENT PARAMETER LIST

Maximum Initial Vapor Temperature	3500-4500 K
Maximum Initial Energy Deposition	< 20 kJ
Final Vapor Pressure	10^{-2} torr
Final Vapor Temperature	T_{sat} (P_{final})
Chamber Overall Geometry	Cylindrical 0.3 m Radius
Chamber Wall Material	Stainless Steel with Silicon Carbide Laminate
Vaporization Mechanism	Capacitive Discharge

of 10-20 ms. This estimate assumes that the condensation heat transfer coefficient scales as unity because pressure, temperature, and materials are the same at the two scales. The second implication from the current scaling is that the surface area to volume ratio has been increased by the scale factor (L ~ 16). Thus, more energy and mass will condense per unit time or conversely for a given time increment the condensation heat transfer ought to be much more efficient because of the increased surface area to volume ratio. This points out that we cannot empirically use the condensation rates measured in the experiments. Rather, we must successfully model the experiment and apply this model to the larger scale prototypic facility. This is where we intend to incorporate our work into the CONRAD hydrodynamics model or some other appropriate tool for large scale simulations of the ICF reactor design.

The final consideration in the feasibility design is the specification of the chamber shape and wall material. Originally, we had conceived of a spherical cavity which would insure a one-dimensional behavior of the fluid motion. However, as will be discussed later, our concept for producing the vapor is by capacitive discharge. It appears that such a scheme will inherently introduce two-dimensional fluid motion in the chamber even though it would be spherical. Secondly, when we examined the fabrication cost of the chamber we found that to insure a spherical cavity would make the cost prohibitive for this small scale facility. In addition, the fabrication of the weld joints would also detract from the spherical shape and would probably affect the one-dimensional fluid motion. Therefore, we would propose to construct a cylindrical chamber (Fig. 3-7) in which the capacitive discharge electrodes would be on-axis with the cylinder axial length. In this way the initial two-dimensional motion of the fluid would be axisymmetric and more easily predicted. The second benefit would be that the chamber can be easily constructed as three separate pieces (cylinder, top and bottom plate) connected by a standard flange and seal gasket arrangement. The wall material that we would use is a commercially available stainless steel laminated with a silicon-carbide surface. Such a material could be heated to the required temperatures (800 K) and retain its structural integrity. The silicon-carbide surface is also the actual material being proposed in many ICF designs for the wall material and would be compatible with the high surface temperatures that could occur during the initial condensation transient.

The instrumentation and experimental setup is conceptually displayed in Fig. 3-8. We would plan to run the experiment using a microcomputer as the time sequencer and data reduction device. Through a standard output interface one can send a 1-10 V signal to trigger the capacitive discharge device and vaporize the liquid metal sample. The instrumentation will then measure the amperage and voltage through the capacitive discharge device, the wall temperature as a function of position, the wall heat flux and gas properties and transfer this data to a computer buffer interface via a high speed A/D system. We tentatively plan to acquire a LeCroy KAMAC 8-channel A/D system for this function based on its ability for high speed data acquisition (1 MHz), modularity, and portability. This also allows us to use the expertise of the Phaedrus plasma physics group at the UW to aid us in the initial usage of this data acquisition device.

The independent variables considered in this experiment are:

(1) Mass and composition of the vaporized sample
(2) Energy deposited in the sample (i.e., temperature)
(3) Initial wall temperature
(4) Chamber gas mass and composition.

We have not developed an experimental test matrix as yet. The exact range of values considered will depend to a large extent on the performance of the capacitive discharge system that we must design and build. This system will vaporize the sample and thus determine the allowable bounds on sample mass and input energy.

The capacitive discharge system preliminary design indicates that the most proven design would involve plating the liquid metal as a thin coating on a tungsten wire. The tungsten wire would be held between the electrodes and about 17 kJ of energy would be discharged through the wire in a time less than 1 ms. We considered peak operating voltages of 5-15 kV with a wire radius of 60 μm. In the simulation calculations this filament radius satisfied our requirements of delivering the required energy within the millisecond time frame. The wire length would be on the order of 10 cm, although its exact length will depend on the optimum thickness of the liquid metal coating over the tungsten filament.

REFERENCES FOR SECTION 3

1. T.J. Dolan, Fusion Research, Pergammon Press, New York, Vol. 2 (1982).

2. G.L. Kulcinski, "First Wall Protection Schemes for Inertial Confinement Fusion Reactors," J. Nucl. Materials 85-87, (1979).

3. J.M. Williams, F.T. Finch, T.G. Frank, J.S. Gilbert, "Engineering Design Considerations for Laser Controlled Thermonuclear Reactors," Proc. 5th Symp. of Engineering Problems of Fusion Research, p. 102, Princeton, NJ (1973).

4. G.L. Kulcinski et al., "The INPORT Concept - An Improved Method to Protect ICF Reactor First Walls," J. Nucl. Materials 103 & 104, (1981).

5. T.G. Frank, G.E. Rossi, "Technological Requirements for Commercial Applications of Inertial Confinement Fusion," Nuclear Tech./Fusion 1, 359 (1981).

6. B. Badger et al., "HIBALL - A Conceptual Heavy Ion Beam Driven Fusion Reactor Study," University of Wisconsin Fusion Technology Institute Report UWFDM-450 (1981).

7. B. Badger et al., "Annual Report for the LIBRA Light Ion Beam Fusion Reactor Project for the Period Jan.-Dec. 1983," Fusion Power Associates Report FPA-83-8, December 1983. Also, B. Badger et al., "Annual Report for the LIBRA Light Ion Beam Fusion Reactor Project for the Period Jan.-Dec. 1984," Fusion Power Associates Report FPA-84-8, December 1984.

8. L.A. Glenn, "Transport Process in an ICF Reactor," Nuclear Eng. & Design 54, 1 (1979).

9. L.A. Glenn, D.A. Young, "Dynamic Loading of the Structure Wall in a Lithium-Fall Fusion Reactor," Nuclear Eng. & Design 54, 1 (1979).

10. L. Pong et al., "Liquid Metal Condensation in the Cavity of the HIBALL Heavy Ion Fusion Reactor," Nuclear Eng. & Design/Fusion 3, 47 (1985).

11. R. Peterson, "CONRAD - A Combined Hydrodynamics-Condensation/Vaporization Computer Code," University of Wisconsin Fusion Technology Institute Report UWFDM-670 (1986).

12. J.H. Pitts, "CASCADE: A High-Efficiency ICF Power Reactor," Lawrence Livermore National Laboratory Report UCRL-93554 (Oct. 1985).

13. A.J.C. Ladd, "Condensation of Ablated First-Wall Materials in the CASCADE Inertial Confinement Fusion Reactor," Lawrence Livermore National Laboratory Report UCRL-53697 (Dec. 1985).

14. R.R. Peterson, "Analysis of Cavity Conditions in Heavy Ion Beam Fusion Reactors," University of Wisconsin Fusion Technology Institute Report UWFDM-719 (Feb. 1987).

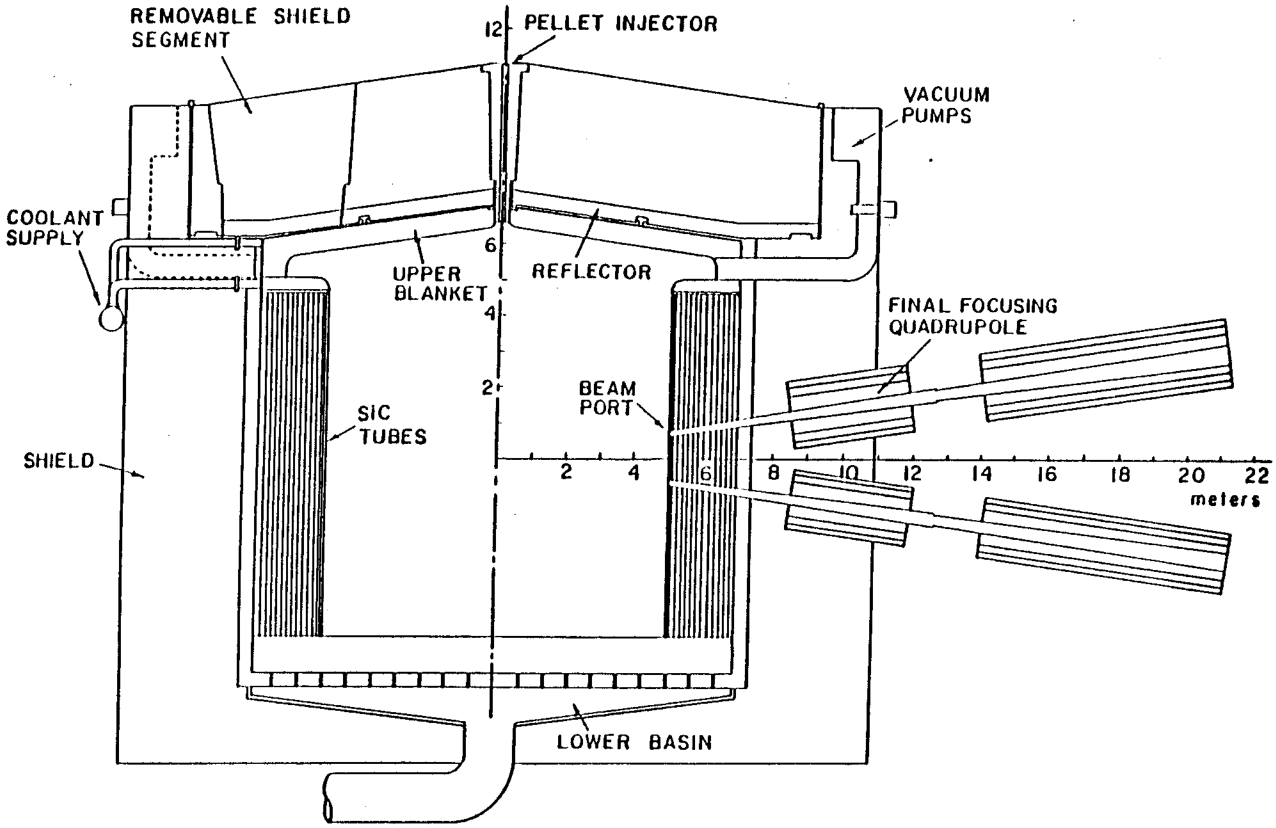

Fig. 3-1. Cross-sectional view of HIBALL reactor chamber.

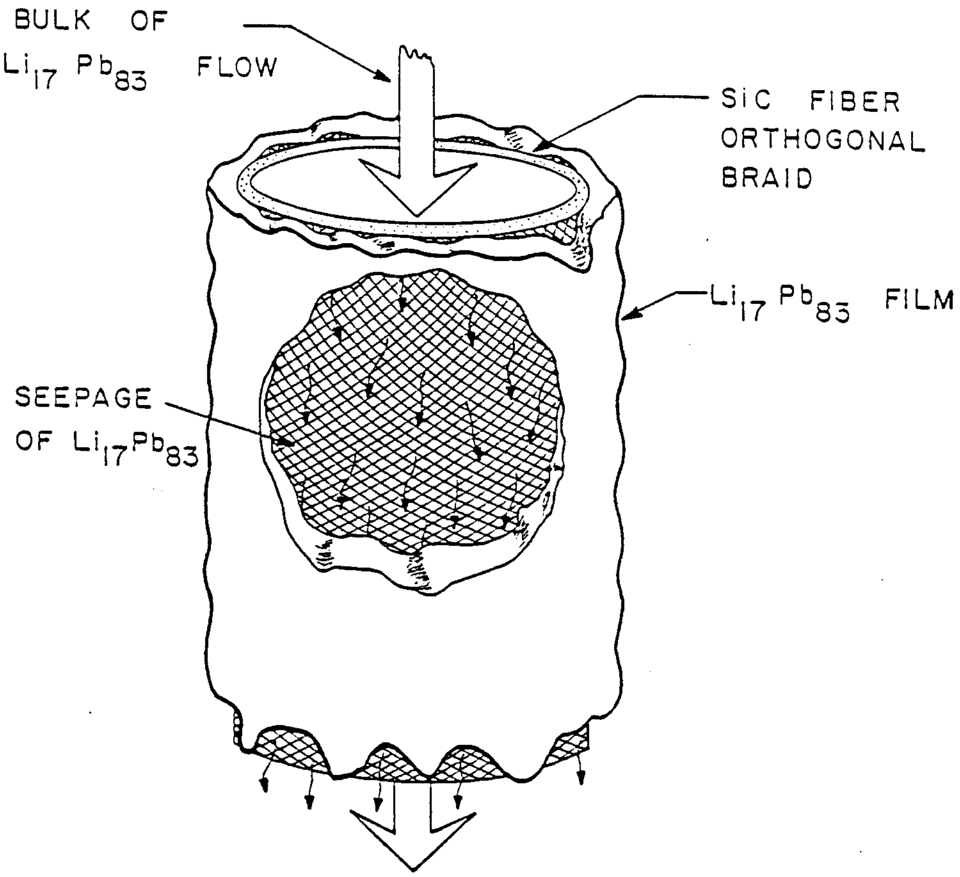

Fig. 3-2. Schematic of INPORT concept. Metallic coolant seeps through porous woven structure to protect outside of tube from target x-ray and ion debris.

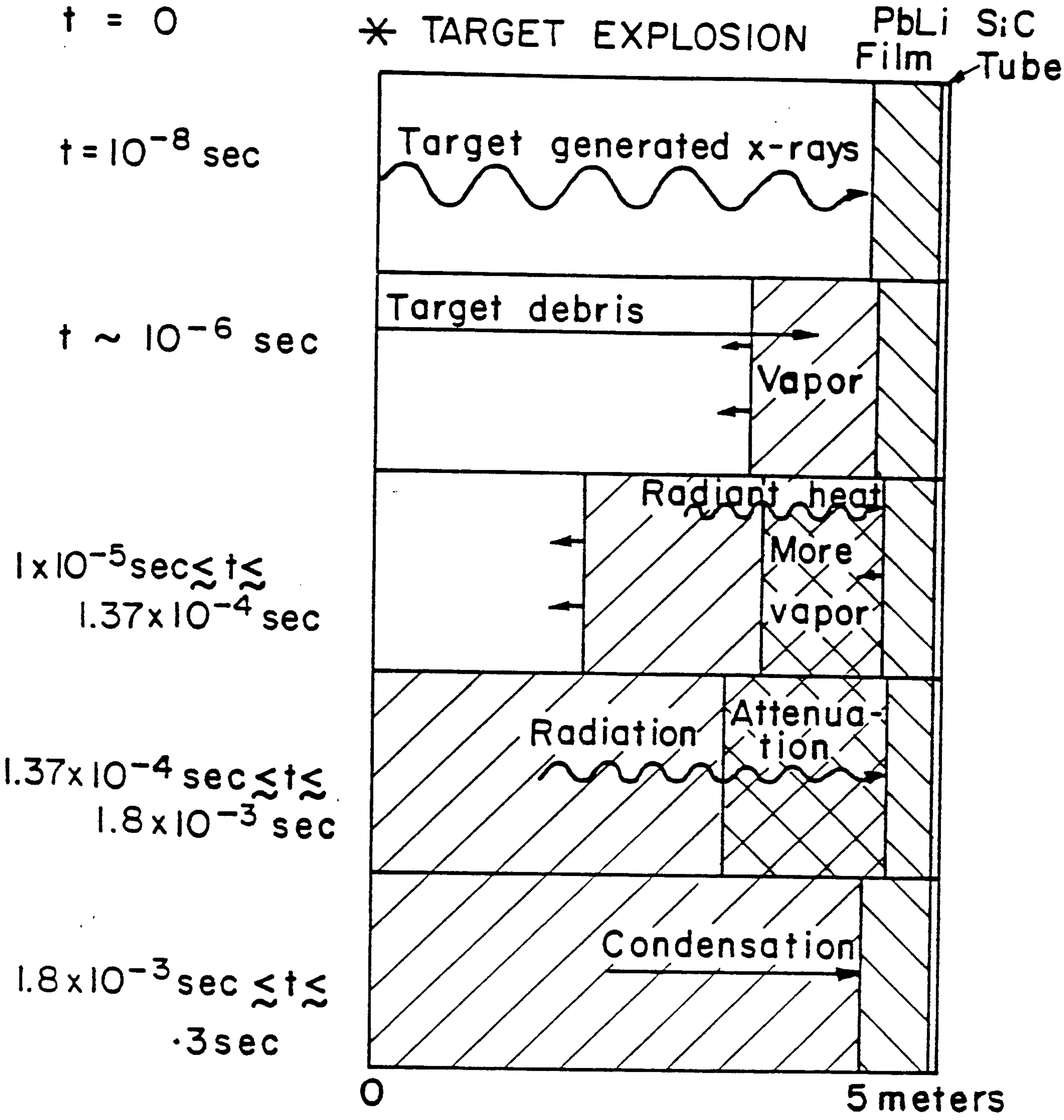

Fig. 3-3. Vaporization phenomenon in ICF target chambers.

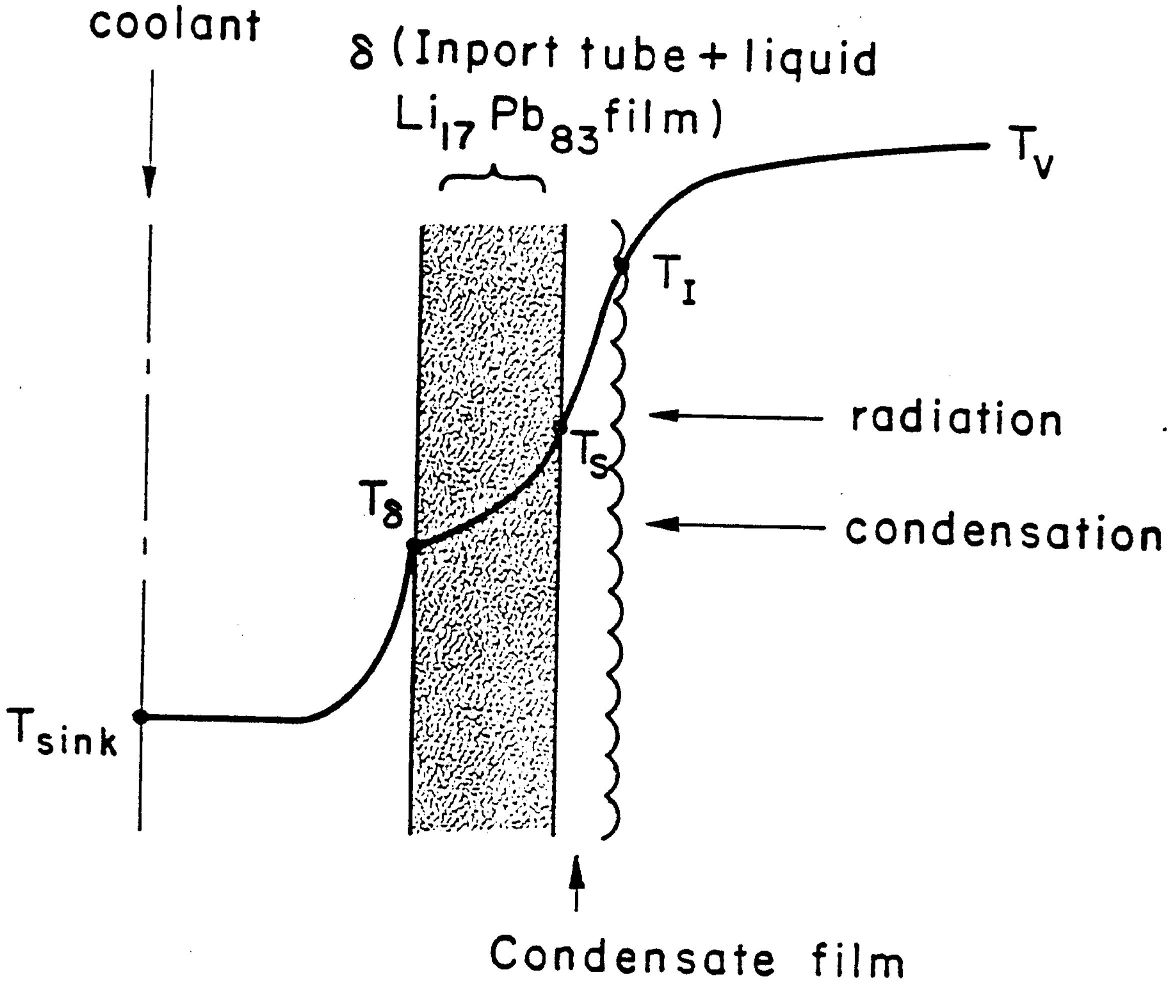

Fig. 3-4. Schematic temperature profile in ICF target chamber first walls.

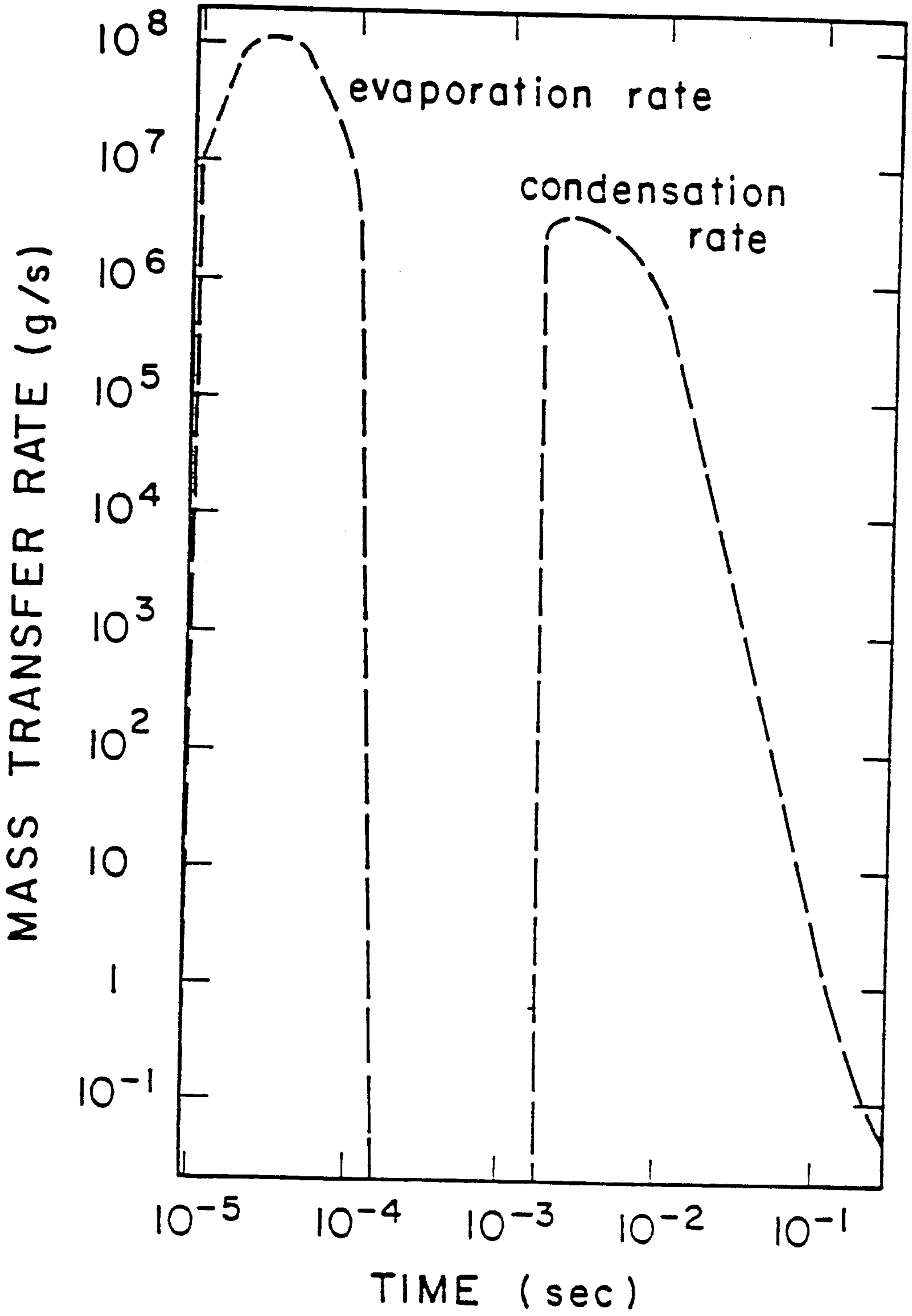

Fig. 3-5. Evaporation and condensation rates on first surface for mass of vaporized gas = 13 kg.

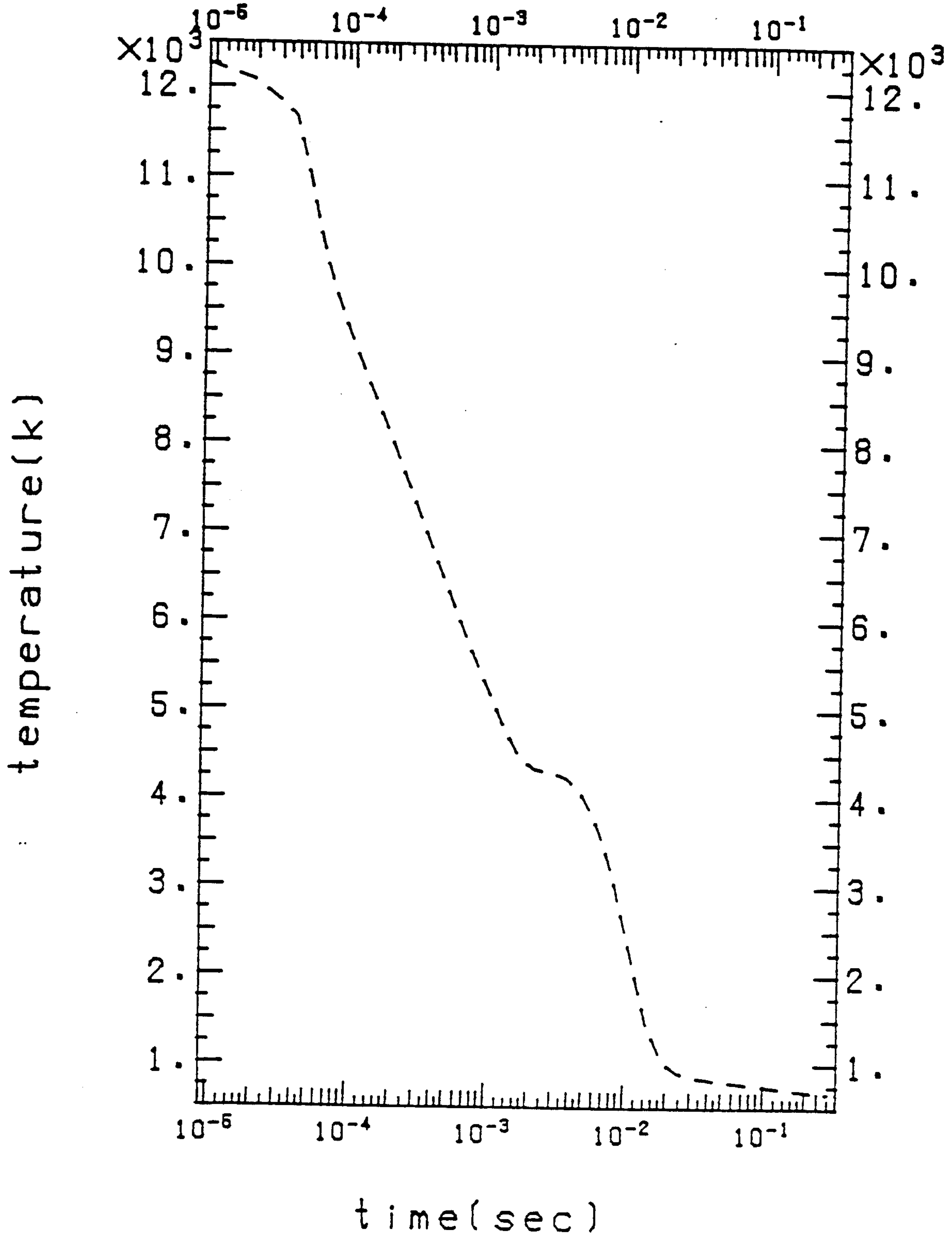

Fig. 3-6. $Li_{17}Pb_{83}$ vapor temperature as a function of time.

Fig. 3-7

CONCEPTUAL PICTURE OF CHAMBER

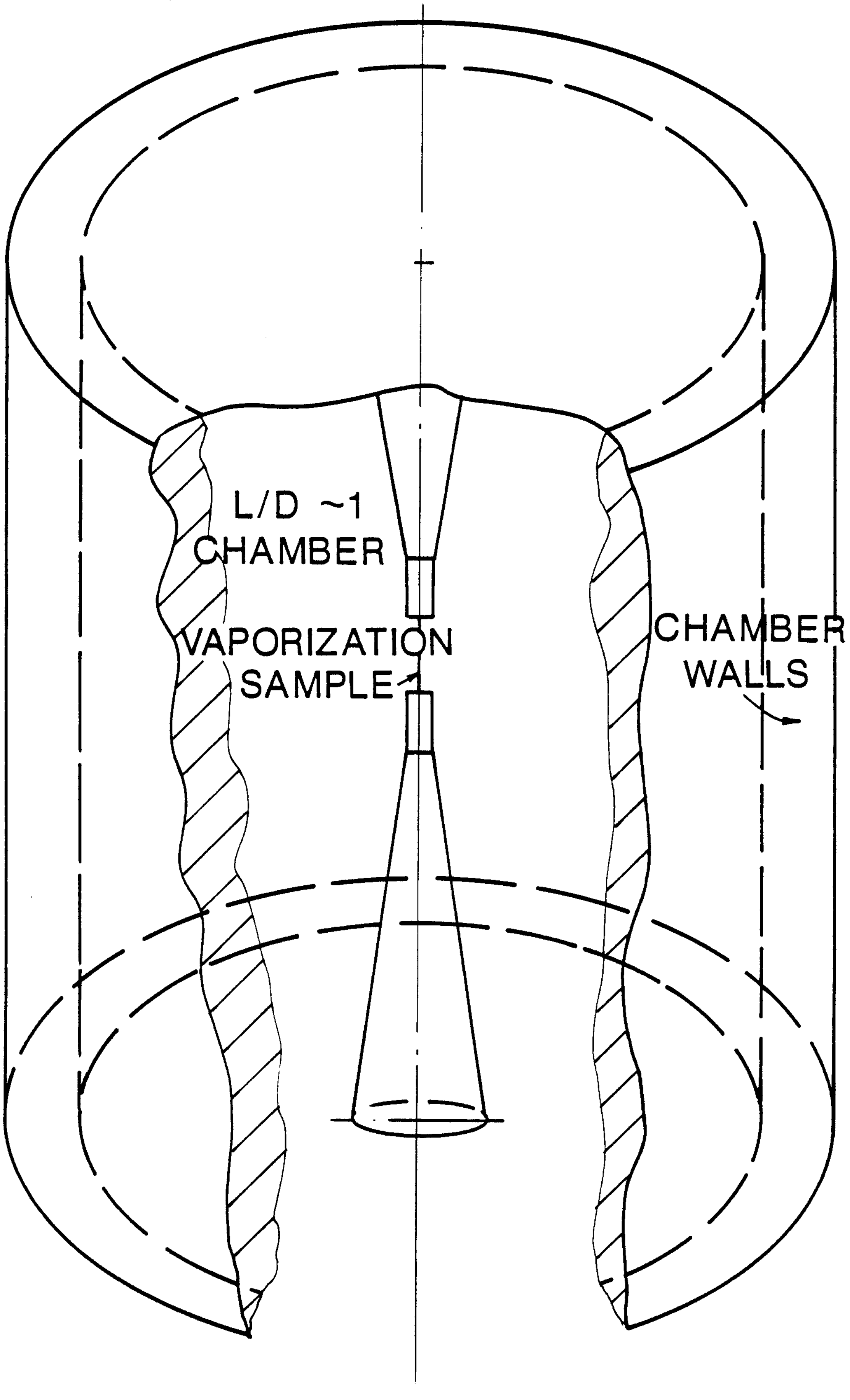

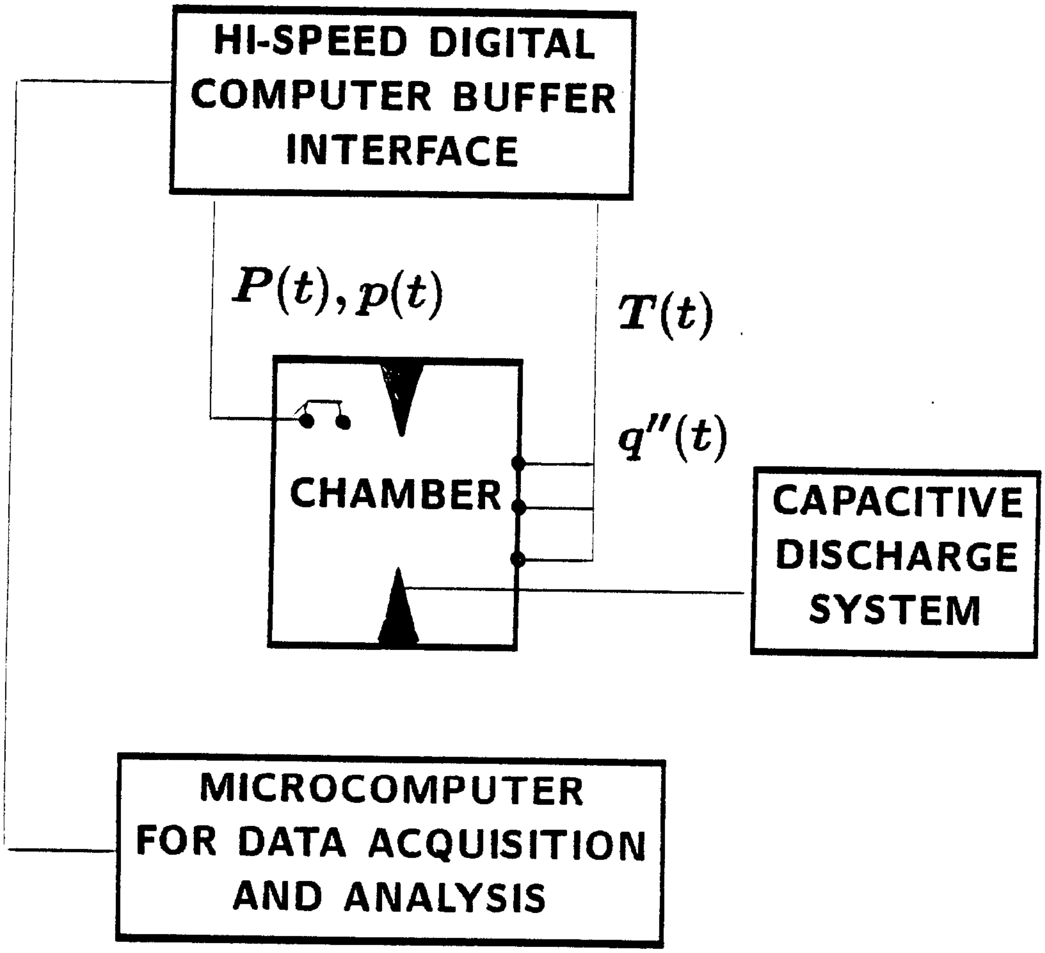

Fig. 3-8. Conceptual picture of experimental setup.

4. VAPORIZATION EXPERIMENT DESIGN

We have designed an experiment that would use currently available sources of x-rays to vaporize samples of typical ICF first surface materials. This experiment would provide important data for verification of rapid vaporization physics in CONRAD and for study of the physics of rapid vaporization. The design is shown in Fig. 4-1, where the x-ray source is a gold foil that is irradiated with a short wavelength laser. The x-ray source could instead be a flash board or some other more direct use of pulsed power.

Also shown in Fig. 4-1 is a depiction of x-ray vaporization in ICF target chambers. Here as much as 20%[1] of the target yield is released in the form of x-rays. A typical x-ray spectrum for a target with a heavy element tamper[1] is shown if Fig. 4-2. The spectrum consists of a component centered around 1 keV, which is radiated over a few nanoseconds, and a much higher energy part that is radiated over a much shorter time. Some target chamber designs allow large fluences of these x-rays to reach the target chamber wall and to vaporize it. This vaporization can lead to wall erosion, impulsive mechanical loading due to recoil from the vaporization, and shielding of the first wall from target generated blast waves. We have assessed the relevance of the experiment shown in Fig. 4-1 to these three issues.

There are multiple choices for the type of x-ray source. A large short wavelength laser such as NOVA is capable of converting most of its energy into x-rays when it is focused on a gold foil. NOVA was designed to focus 50 kJ of 0.35 μm light onto a target, though a planar target could only receive five of the ten beams on a surface. The NOVA laser currently operates at the 20 kJ level. Therefore we have assumed NOVA could produce 10 kJ of x-rays. There is the possibility of controlling the x-ray spectrum from such a source by adjusting the laser pulse width and spot size.

Another choice is a more direct use of pulsed power to create x-rays. Pulsed power machinery applies a large voltage across electrodes to create either relativistic electrons that are stopped in some material to create x-rays or to drive a discharge current through a gas puff that leads to a magnetic pinching of the gas to the point that it is hot and dense enough to strongly emit x-rays. Since these methods are more direct, they are overall a more efficient and cheaper way of making x-rays than solid state lasers. For example, Sandia National Laboratory has been able to create as much as 100 kJ of x-rays with the PROTO-II accelerator,[2] which is a much smaller and less costly device than NOVA. However, the experimental geometries are more confined than with a laser-foil x-ray source because the electrodes that carry the pulsed power take a large part of the total solid angle, though even with this problem Sandia has been able to irradiate samples with x-rays. It is also possible to control the x-ray spectrum through changes in gas puff or electron target species, though experimenters may be able to more carefully tailor the x-ray spectrum in a laser-foil system.

The final choice for an x-ray source we have considered is a flash board. This method would call for a flash board to be connected to a capacitor bank. Sandia National Laboratories has been using flash boards to create soft x-rays for cleaning and preionization of anode surfaces in light ion beam diodes.[3] The efficiency of creating x-rays with flash boards is typically a few percent and as much as 80 J of x-rays have been created. The widths of the x-ray pulses are in the several 100 nanosecond range. Blackbody temperatures of 10's of eV have been achieved. This is a very inexpensive way of creating x-rays since one only needs a flash board and a capacitor bank. One could possibly adjust the blackbody temperature upwards with proper choice of the insulator gap dimensions and material. The total energy in x-rays is much less than in the other options, so the samples would have to be placed very close to the flash boards and the flash boards would have to be increased in size.

The choice of x-ray sources therefore comes to a choice between cost, total energy, and experimental flexibility. Short wavelength lasers irradiating foils have high cost, good experimental flexibility, and, as we show below, adequate energy to do relevant experiments. Electron beam and pinched gas puffs have lower cost, large x-ray energy fluences, but reduced flexibility. Flash boards are the cheapest, but have the lowest x-ray energy and questionable experimental flexibility. We have chosen a laser-foil source for further analysis.

Besides the x-ray source, the experimental design consists of a system of samples that are connected to pendulums that would allow measurement of the recoil impulse. This method for measuring recoil impulses has already been used in the NOVA facility, where recoil impulses caused by laser vaporization of aluminum have been measured.[4] The resulting swing on the pendulum can be recorded with television cameras on videotape. The samples would be polished to insure one-dimensional deposition of the x-rays. The samples would be carefully weighed before and after the experiment, to allow measurement of the vaporized mass. The experiment chamber would have to be filled with a low enough density gas to permit the transmission of the x-rays from the source to the samples. We have chosen 0.1 torr of helium as a chamber gas. We feel that the experiment could irradiate several 1 cm square samples at the same time, though the samples should not be so close to each other that one will adsorb the vapor of another.

Some attention should be paid to sample preparation and analysis. So that the x-rays are normal to the surface, the surface should be smooth to less than 0.1 μm surface roughness. With some materials, this should be relatively easy to achieve with a combination of standard polishing, electrochemical methods, and diamond turning. Aluminum is one material that one could make very smooth. Other materials, like graphite, may be difficult to polish to much smoother than a 1 μm finish. It is also important to have samples that have uniform densities, and once again aluminum has less problems than graphite. In fact graphite is a difficult choice for sample material and is only proposed because it is a good candidate for an ICF target chamber material. Using single crystals of graphite would be a way of getting better uniformity and surface smoothness through cleaving. Care should be taken that the samples not be handled between weighings as that would add micrograms to the mass of a sample.

After the experiment, it will be quite interesting to slice the sample material and microscopically examine it. One should be able to tell what regions have been vaporized and recondensed, melted and solidified, and have experienced thermal stresses and shocks. These are all important phenomena in the response of wall materials in ICF target chambers.

An experiment such as this should provide good measurements of vaporization thicknesses. We have used CONRAD to calculate the vaporized mass and thicknesses that might reasonably be produced in such an experiment. We have used an x-ray source that could be driven with the NOVA laser as an example. We have assumed that 10 kJ of x-rays could be created by irradiating a gold foil with the NOVA laser. We have assumed that by changing characteristics of the laser beam, that one could change the spectrum of the x-rays. We have calculated the vaporization for graphite and aluminum samples that are different distances from a 100 eV blackbody spectrum x-ray source and for graphite samples that are 10 cm from x-ray sources of variable blackbody temperatures. The results are summarized in Table 4-1 and in Figs. 4-3 and 4-4. The samples have 1 cm^2 of surface exposed to x-rays. The vaporized masses for graphite samples are below 10^{-4} grams while they are somewhat larger for aluminum. Balances are available that can measure mass changes in this range. We have looked at samples that are positioned from 10 to 30 cm from the target.

The vaporization calculations for this experiment show some interesting trends. When looking at the amount of vaporization as a function of distance from the target, one sees that the vaporized masses and thicknesses do not scale directly with the x-ray fluence. Also, the ratio of the vaporization in aluminum to that in graphite changes as a function of the distance from the target. Finally, one notices that the vaporization reaches a maximum at a blackbody temperature around 100 eV. At lower temperatures the range shortens and this limits the vaporization, while at high temperatures the range

Table 4-1. Vaporization Experiment Parametric Study

	Distance from Target to Sample (cm)			
	10	15	20	30
Graphite Sample - 10 kJ of 100 eV blackbody spectrum x-rays				
Vaporized Mass* (μg)	73.8	41.0	31.4	24.1
Vaporized Thickness (μm)	0.327	0.182	0.139	0.107
Aluminum Sample - 10 kJ of 100 eV blackbody spectrum x-rays				
Vaporized Mass* (μg)	147	91.9	64.1	35.0
Vaporized Thickness (μm)	0.544	0.340	0.237	0.127

	X-Ray Blackbody Temperature (eV)				
	50	100	150	200	1000
Graphite Sample - 10 cm from Target to Sample					
Vaporized Mass* (μg)	67.2	73.8	70.7	62.0	0.
Vaporized Thickness (μm)	0.297	0.327	0.315	0.276	0.

---

* The Exposed Area of the Sample is 1 cm^2

is longer so the local energy density is reduced and the vaporization is ultimately reduced. Therefore, there is an optimum spectrum for vaporization at an intermediate blackbody temperature.

One feature of ICF that this experiment would not simulate is the interaction of target debris ions with the vaporized material. We have seen in the simulation of target chamber phenomena in the APEX facility,[5] that the vapor can absorb debris ions, convert the energy to hydrodynamic motion and transmit a shock to the wall. This phenomenon is complex and needs to be studied experimentally. The samples are small in the present experimental design, so the vapor plume can spread out two-dimensionally and greatly reduce the ability of the vapor to stop the ions. Also, to create this shock in the vapor we would need roughly as much energy in ions as in the x-rays. One could modify the experiment to study this phenomenon by using large sample sizes, with one sample per shot, and by adjusting the laser pulse and the laser target to reduce the x-ray conversion and thus leave more energy in the laser-plasma. The ion energies might be different from those in ICF reactor applications, but it would still be a relevant experiment.

There are some differences between ICF target chamber conditions and this experimental design. The x-ray spectrum is much softer and the energy fluences much lower. Our computational results show that for a blackbody temperature of 1000 eV, typical of ICF target spectra, there is no vaporization of a sample located at 10 cm from the target. The pulse widths of the x-rays are similar, at about 1 nanosecond, so the rapid vaporization phenomena should be similar. In this respect, the experiment would be relevant to ICF.

REFERENCES FOR SECTION 4

1. G.A. Moses, R.R. Peterson, M.E. Sawan and W.F. Vogelsang, "High Gain Target Spectra and Energy Partitioning for Ion Beam Fusion Reactor Design Studies," University of Wisconsin Fusion Technology Institute Report UWFDM-396 (Nov. 1980).

2. D.L. Hanson and M.K. Matzen, "Comparative Study of X-ray and Ion Beam Energy Deposition in Aluminum using Pulsed Power Sources," Bull. APS 30, 1504 (1985).

3. J.R. Woodworth, P.F. McKay, and W. Jaramillo, "Particle Beam Fusion Progress Report July 1984 through December 1984," Sandia Report SAND85-0616 (Nov. 1985) pp 57-60.

4. C.E. Annese, "85 Laser Program Annual Report," Lawrence Livermore National Laboratory Report UCRL-50021-85 (November 1986) pp. 4-34 through 4-35.

5. R.R. Peterson, R.L. Engelstad, G.A. Moses, and E.G. Lovell, "Target Chamber Design Considerations for the APEX Light Ion Beam Fusion Facility," University of Wisconsin Fusion Technology Institute Report UWFDM-724 (May 1987).

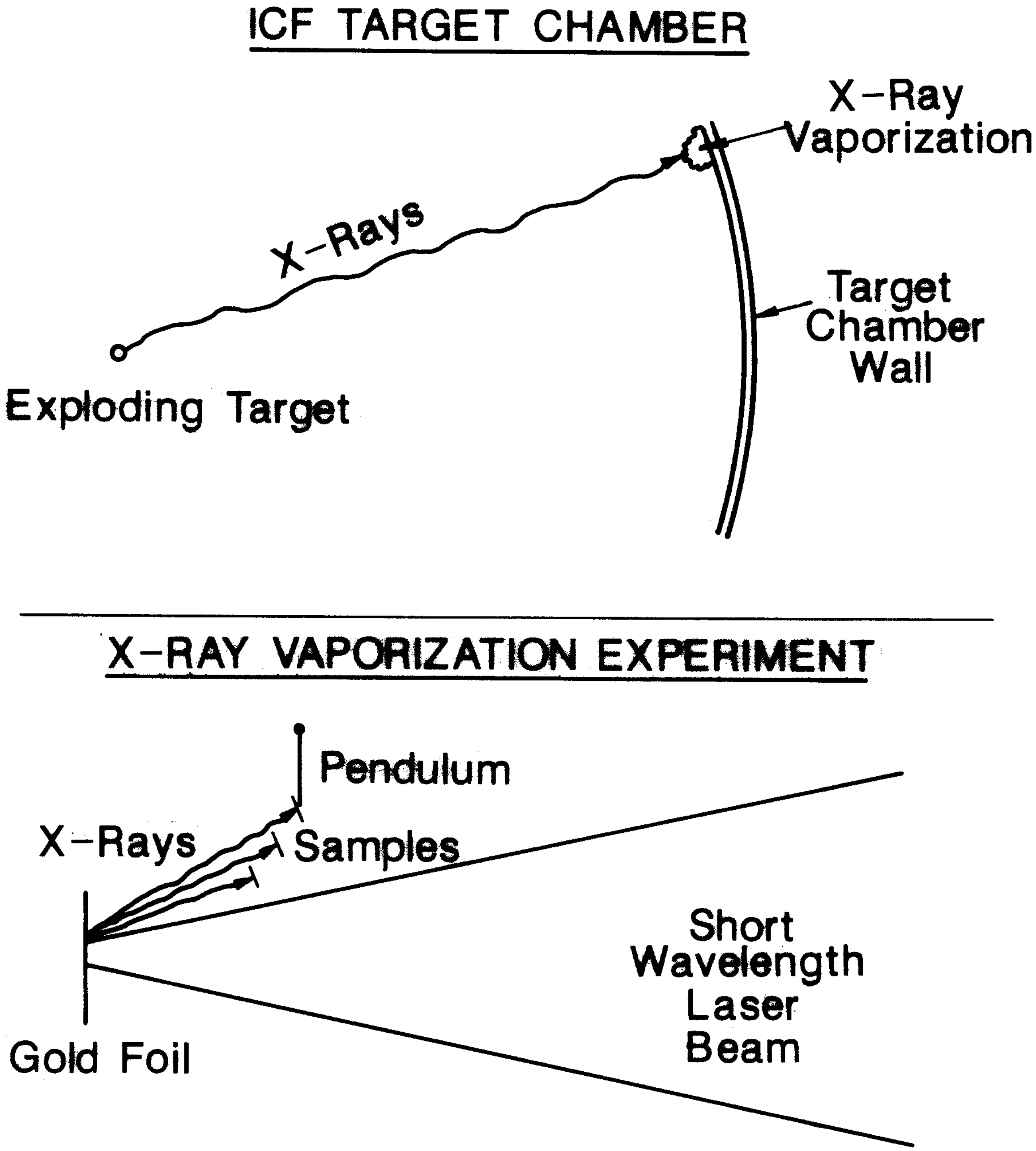

ICF TARGET CHAMBER

X-RAY VAPORIZATION EXPERIMENT

Fig. 4-1. X-ray vaporization in ICF target chambers and the x-ray vaporization experiment.

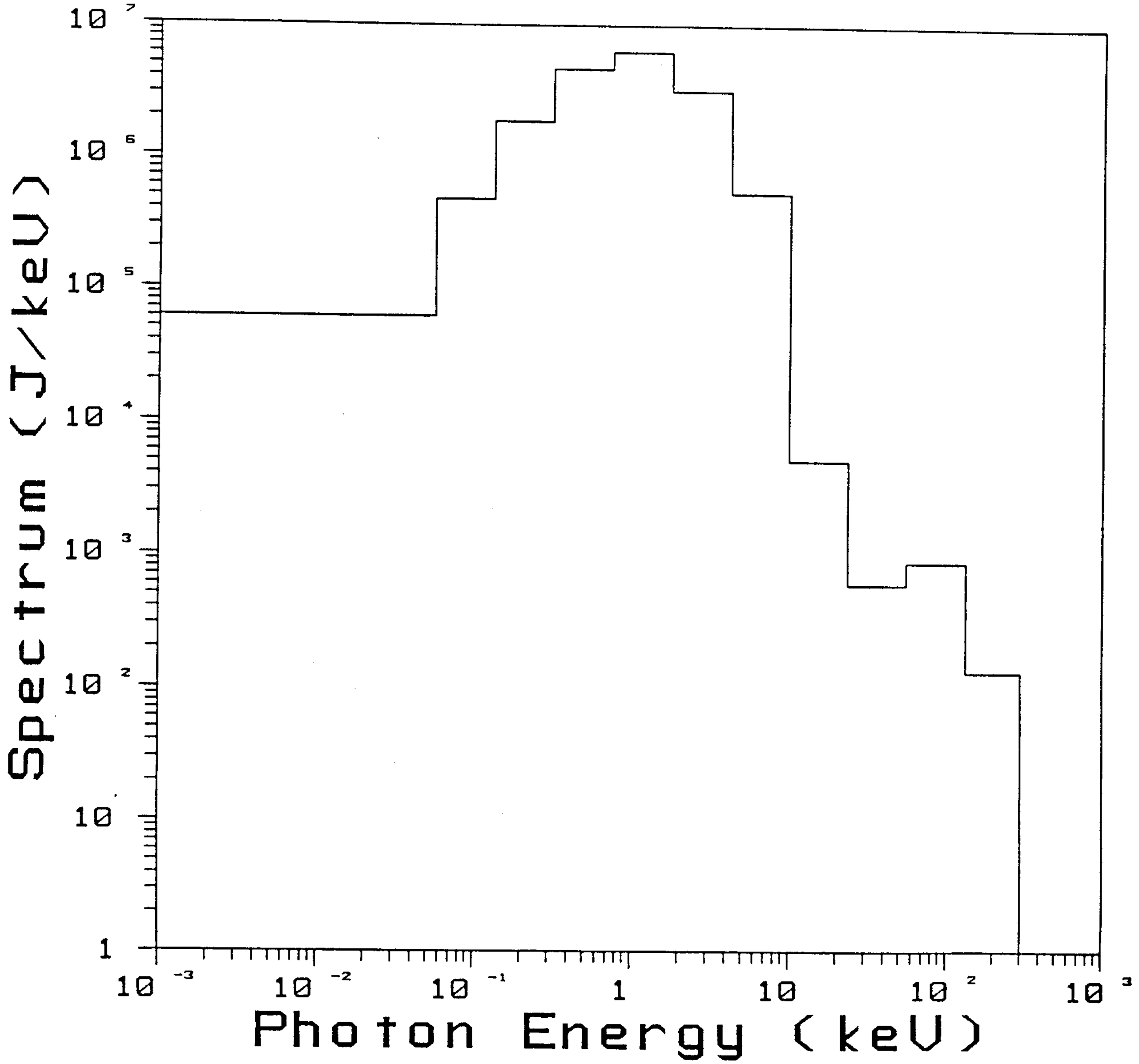

Fig. 4-2. Typical x-ray spectrum for an ICF target.

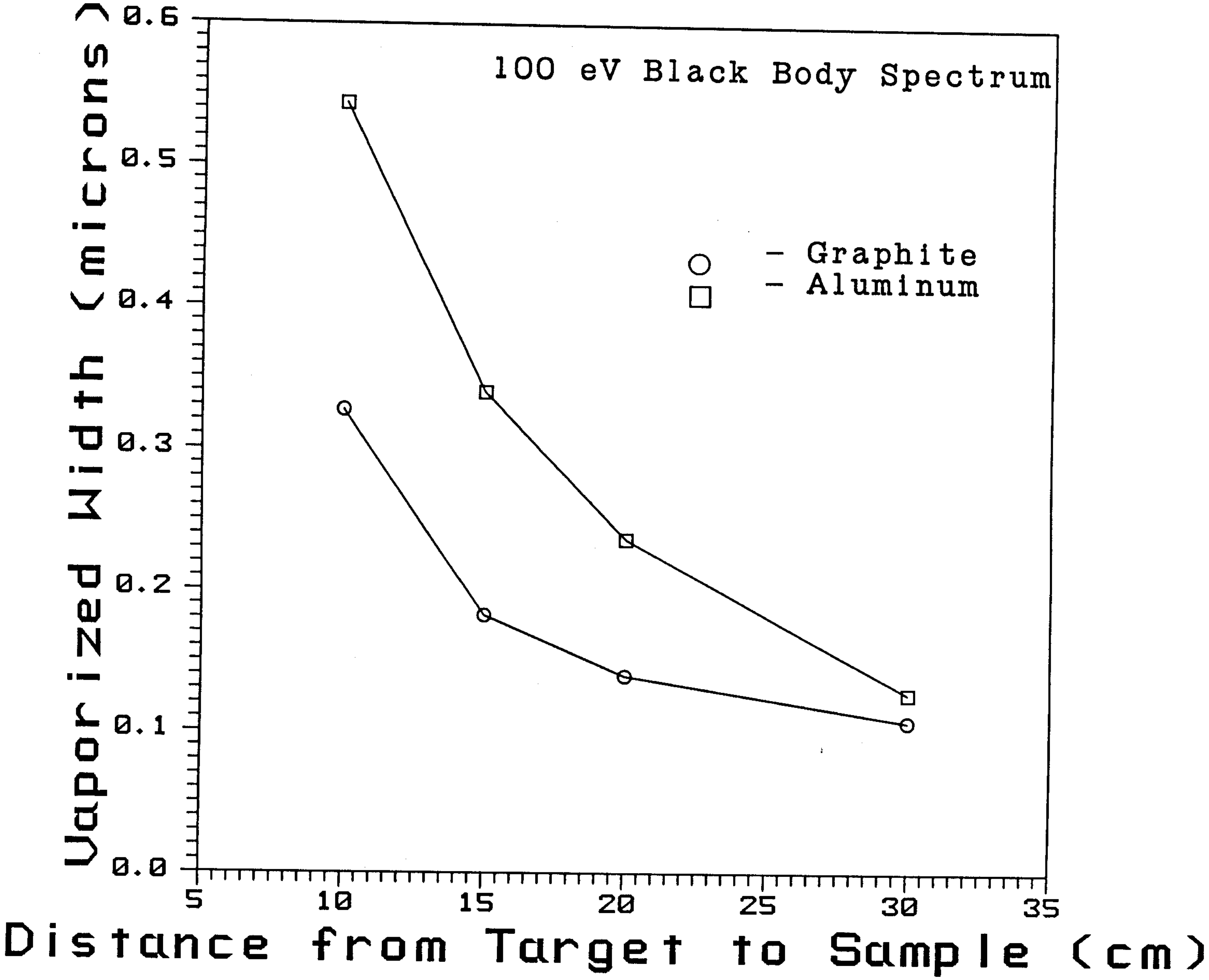

Fig. 4-3. Vaporized thickness for graphite and aluminum samples versus distance from target. X-rays consisted of 10 kJ of a 100 eV blackbody spectrum.

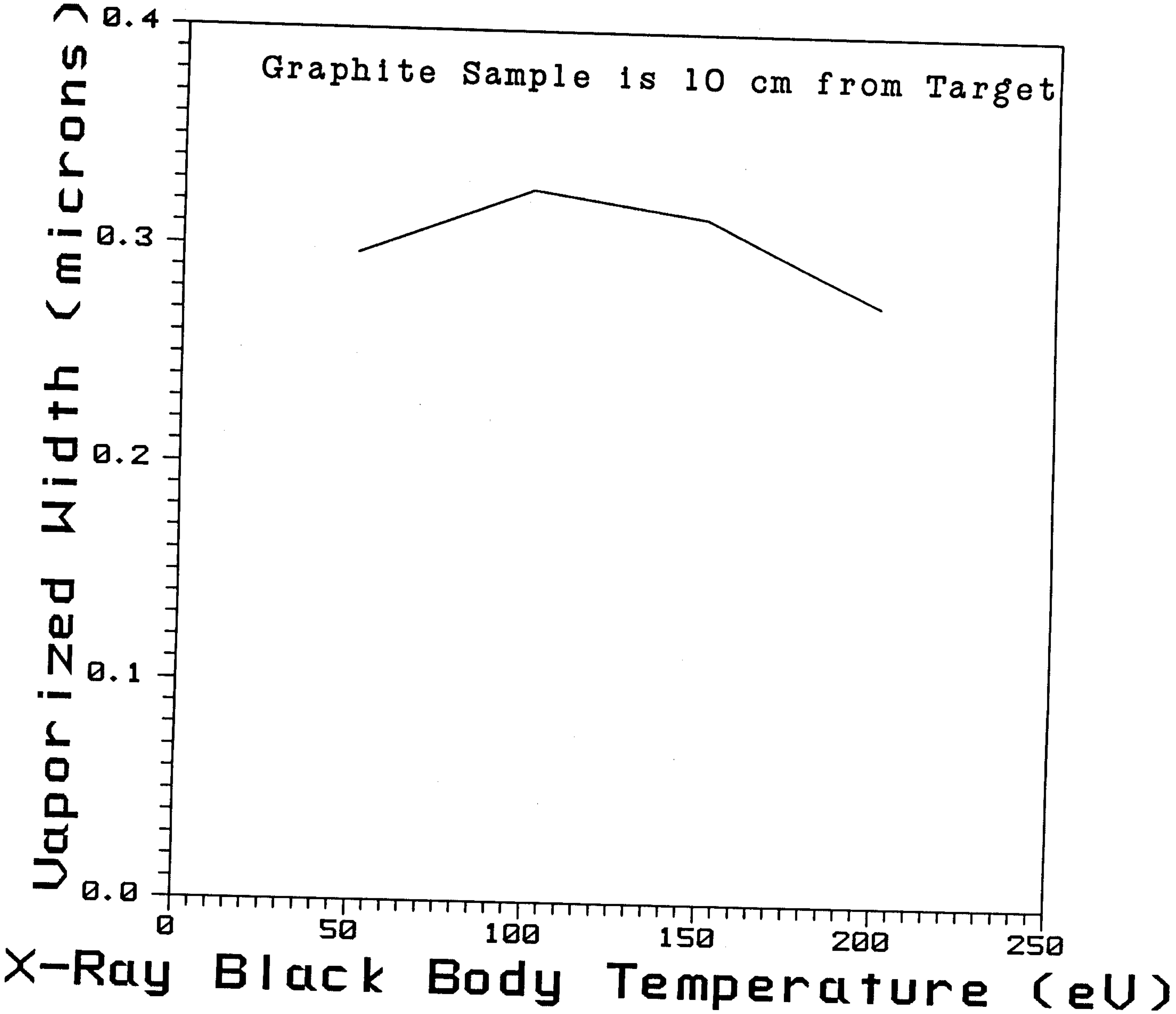

Fig. 4-4. Vaporized thickness for graphite samples versus blackbody temperature of x-ray spectrum. Samples were 10 cm from target.

5. CONCLUSIONS

We have studied three general areas related to ICF cavity gas phenomena: (1) verification of the CONRAD and MIXERG computer codes, (2) design of an experiment to study the condensation of vaporized material in ICF target chambers, and (3) design of an experiment to study x-ray vaporization phenomena in ICF target chambers. We have performed these tasks during the period from July 1, 1986 and June 30, 1987.

We have reached the following conclusions regarding the accuracy of the CONRAD and MIXERG computer codes:

1) Equation of State: The equation of state data provided by MIXERG appears to be quite reasonable.
2) Opacities: The MIXERG opacities for low density plasmas (i.e., electron densities $\lesssim 10^{16}$ cm^{-3}) are too large, but this problem can be fixed without a significant effort. The large opacities result in CONRAD overestimating the radiation emitted from low density plasmas. Also, the bound-bound contributions to the opacity seem to be underestimated.
3) Ion Stopping Cross Sections: The low temperature cross sections are in very good agreement with experimental data. The high temperature values could not be validated because of the lack of experimental data. It is realized, however, that it would be worthwhile to develop a model for computing the evolution of the debris ion charge states as the ions travel through the background gas.
4) Radiation: Simulations of the NRL experiments show that the radiation losses computed by CONRAD are too large. This is because the opacities are too large (see item 2 above). Also, we mention that in some of the NRL experiments, the radiation diffusion approximation breaks down because the photon mean free paths become large in low density background gases.
5) X-ray Deposition: The x-ray deposition agrees with the BUCKL and PROFILE codes and we believe that it is now an accurate calculation.
6) Vaporization: We have compared vaporization calculated with CONRAD with rather long pulse electron beam vaporization experiments. The agreement on the threshold energy fluence for vaporization that we have obtained verifies the heat transfer calculation in the material as it is done in CONRAD. There is some disagreement between CONRAD and the experiment on the amount of vaporization at fluences above the threshold. We believe that the disagreement is due to dispersal of the vapor plume in the experiment, while CONRAD assumes that the vapor remains between the electron source and the sample. When CONRAD is compared with another calculation that makes this same assumption, we get good agreement. We

therefore believe that the slow vaporization model in CONRAD is correct. This says nothing about the rapid vaporization model in CONRAD, for which we have not found relevant experiments.

We have completed the design of a condensation experiment that uses a liquid metal vapor source. The vapor would be created with an electrical discharge. The overall experiment would be of such a size and cost that it could be done as a university "table top" experimental program.

We have completed the design of an x-ray vaporization experiment. Lasers and more direct uses of pulsed power have been considered as x-ray sources. Sample preparation and handling have been considered for both aluminum and graphite samples. CONRAD has been used to calculate the amount of vaporization that we could expect in these samples in the presence of 10 kJ of x-rays of various spectra. We have addressed methods for diagnosing the amount of vaporization and the recoil impulse.

ACKNOWLEDGEMENTS

This work is supported under contract #9265205 by Lawrence Livermore National Laboratory and U.S. Department of Energy.

Computer time for this work was supplied by the National Science Foundation in a grant to the San Diego Supercomputer Center.